DEVELOPMENT OF FAST LIGHT ALLOYS STAMPING TECHNOLOGY (FAST) FOR MANUFACTURING PANEL COMPONENTS FROM DISSIMILAR ALLOYS – TAILOR WELDED BLANKS (DA-TWBs)

By

ZHAOHENG CAI

A thesis submitted to Imperial College London for the degree of Doctor of Philosophy

Department of Mechanical Engineering
South Kensington Campus
Imperial College London
London SW7 2AZ
United Kingdom

2020

Declaration of originality

This thesis hereby presented is based on research by the author (Zhaoheng Cai) at the Department of Mechanical Engineering of Imperial College London. I declare that the work contained in this thesis is the result of author's independent research under the supervision of Dr Liliang Wang, and that any work that is not has been referenced appropriately. The work of this thesis has not been submitted elsewhere for any other degree or qualification.

Copyright Declaration

Abstract

The reduction of weight for car Body-in-White (BIW) structures through the use of high/ultra-high strength aluminium alloys is the most efficient way to achieve CO_2 emissions and reduce fuel consumption. Hot and warm stamping are forming techniques commonly used in the automotive industry to form aluminium alloy sheets into structural components. However, it is challenging to improve the production rate and achieve further cost savings with these mature forming technologies. Moreover, there are significant challenges in current forming technologies to form dissimilar alloys, and the use of tailor welded blanks for BIW necessitates the development of novel forming technologies.

The present work aims to develop a novel sheet metal forming technology – Fast light Alloys Stamping Technology (FAST) for manufacturing panel components from Dissimilar Alloys – Tailor Welded Blanks (DA-TWBs), whilst achieving desirable mechanical properties in a cost and time efficient manner. The dissimilar alloys in this study consist of two base materials of 6xxx series Al-Mg-Si and 7xxx series Al-Zn-Mg-Cu alloys, which were joined by friction stir welding. The feasibility of the FAST was initially studied on the aluminium alloys AA6082 and AA7075, then applied to the application of DA-TWBs by using the common processing window that was suitable for both AA6082 and AA7075. The optimisation of the processing window of the FAST process and a comprehensive understanding of the thermal-mechanical properties and a post-Paint Bake Cycle (PBC) strength investigation on various forming process condition were conducted. The implementation of the proposed FAST process was conducted by forming M and U-shaped panel components in lab scale. The FAST optimal process was successfully implemented to form a U-shaped component which was made from DA-TWBs at 300 °C and enabled a significant reduction of total cycle time from several hours to 10 seconds, which further improved the production rate to 12.5 spm (strokes per minute).

In order to reduce experimental efforts, the present research described an efficient method to determine the critical processing parameters, i.e. the integration of the Finite Element (FE)

simulated temperature evolutions with the Continuous Cooling Precipitation (CCP) diagrams of aluminium alloys. Through the optimisation of processing parameters, the temperature evolutions and CCP diagrams do not intersect, indicating that the post-PBC strength of the aluminium alloys could be fully retained after a proper artificial ageing process. A general aluminium alloy-independent model with one set of model constants was therefore developed to predict the Interfacial Heat Transfer Coefficient (IHTC) evolutions as a function of contact pressure, surface roughness, initial blank temperature, initial blank thickness, tool material, coating material and lubricant material. Subsequently, the predicted IHTC evolutions for AA6082 and AA7075 were used to simulate their temperature evolutions, which were then integrated with their CCP diagrams to identify the critical processing parameters in hot and warm stamping processes to meet the desired post-PBC strength of the AA6082 and AA7075, which were then experimentally verified by the results of the dissimilar alloy forming.

A software agnostic platform '*Smart Forming*', was developed to provide cloud Finite Element Analysis (FEA) of a hot and warm stamping process in three stages, namely pre-FE modelling, FE simulation and post-FE evaluation. When the desired materials and processing window were uploaded on the platform, the flow stress, material properties, IHTC and friction coefficient were predicted by the model-driven functional modulus and then generated in the form of compatible packages that could be implemented into the desired FE software. Subsequently, the FE simulation was performed either locally or remotely on the developed platform. When the simulated evolutionary thermomechanical characteristics of the formed component were uploaded, the formability, quenching efficiency and post-PBC strength could be predicted and then demonstrated on a dedicated visualiser on the developed platform. Cloud FEA of FAST was conducted to demonstrate the function of the developed platform, showing an error of less than 10 %.

Acknowledgements

First and foremost, I would like to express my sincerest gratitude to my supervisor Dr Liliang Wang, for the continuous guidance, unlimited support and encouragement along my PhD journey. I greatly appreciate him for introducing me to sheet metal forming field with which I was initially unfamiliar and sharing his unique vision of the future of sheet metal forming. He provides me with opportunities and understanding that any student would be eager for. His patience and rigorous attitude toward academic research encourage me to become a better person not only in my future development but also in daily life. I would also like to express my thanks to my co-supervisor Professor Jianguo Lin for his encouragement and support during the last four years of PhD studies.

I would like to express my gratitude to Dr Guizhu Hong, my guardian when I arrived UK back in June 2007, for her unlimited support, encouragement and step-by-step guidance over the past 13 years of the study in the UK.

I would like to thank China Heilongjiang Academy of Sciences Institute of Intelligent Manufacturing (HAS) for providing me with research funding throughout my PhD study and provide me with great opportunity to collaborate with leading researchers from the UK and China. I would also like to thank Smith metal centres Ltd for providing testing materials and TWI Ltd for the support to friction stir welding of dissimilar alloys.

It is my honour and fortune to be part of the research group - Metal Forming and Materials Modelling (MoM). I would like to thank the technical staff, Amit Choda, Mark Holloway, Neil Beadle, Andrew Wallace, Suresh Viswanathan Chettiar, Alex Toth and Dr Ruth Brook for their kind help and assistance in the experimental work. I would especially like to thank Dr Jun Liu, Dr Denis J. Politis, Dr Omer El Fakir, Dr Kehuan Wang and Dr Xiaochuan Liu who provide unlimited support throughout my studies with valuable discussion and scientific writing. I would also like to thank my colleagues: Dr Haoxiang Gao, Dr Kang Ji, Dr Yiran hu, Dr Ailing

Wang, Dr Xi Luan, Dr Qunli Zhang, Dr Yuhao Sun, Dr Yang Zheng, Dr Mateusz Kopec, Dr Jinghua Zheng, Dr Qinmeng Luan, Dr Yu Zhu, Dr Peng Wang, Xiao Yang, Saksham Dhawan, Dimitrios Chantzis, Heli Liu, Xiangnan Yu and Mozammel Mia. I would also like to extend my thanks to Dr Jun Liu. My PhD time would not have been the same without you.

I would like to thank the undergraduate and master students: Tong Ding, Junchen Lu, Paul Josef Batthyany and Calista Yi Xian Lim, for the great support at different stages of my PhD research.

Besides the research group, I would like to thank all the friends I have made in the UK since 2007 when I just arrived, as well as the friends from my hometown Jinjiang, for always being there for me and providing encouragement. Especially, I would like to thank Yaozhou Yang, Lun Ma, Xi Yuan and Jieping Zhang for always be my side and support since my undergraduate studies.

Finally, last but the most important, I would like to thank my family for their endless support, without whom I would not have these achievements. I would like to extend my deepest thanks to my beloved wife Zhijia Wang. It is not only your unconditional love, support, understanding and trust, but also your selfless accompany with our daughter during my PhD studies that enable me to achieve the best in my most difficult time. I cannot imagine a life without your love, and to you, I dedicate this thesis.

Zhaoheng Cai

London, UK

December 2020

Contents

List of Figures

Chapter 1

Chapter 2

Chapter 3

Chapter 4

Chapter 5

Chapter 6

Appendix A

List of Tables

Chapter 2

Chapter 3

Chapter 4

Chapter 5

Chapter 6

List of Publications

Cai, Z., Batthyangy, P., Dhawan, S., Zhang, Q., Sun, Y., Luan, X., Wang, L., 2018. Study of springback for high strength aluminium alloys under hot stamping. *Advanced high strength steel and press hardening*. 117-121. Doi: 10.1142/9789813277984_0019

Cai, Z., Politis, D. J., Chettiar. S. V., Dhawan. S., Yang, G., Wang, L., Lin. J., 2019, Experimental and simulation analysis in single point incremental forming (SPIF) of AA5754. *3rd International Conference on Light Materials – Science and Technology*. 5-7 November 2019, Manchester, United Kingdom.

Cai, Z., Sun, Y., Fakir, O. EL., Liu, J., Zhang, Q., Wang, L., 2019. Study of springback behaviours of AA7075 under hot/warm stamping. *3rd International Conference on Light Materials – Science and Technology*. 5-7 November 2019, Manchester, United Kingdom.

Cai, Z., Lim, Y. C., Dhawan. S., Liu, J., Politis, D. J., Wu, G., Wang, L., Liu, X., 2020. Cloud FEA of hot stamping processes using a software agnostic platform. *The International Journal of Advanced Manufacturing Technology*. (Under Review)

Liu, X., **Cai, Z.,** Zheng, Y., Fakir, O. EL., Wang, L., 2020. Development of a general interfacial heat transfer coefficient model to characterise the critical processing parameters in hot and warm aluminium stamping processes. *Applied Thermal Engineering*. (in press):115619-115645.

Sun, Y., **Cai, Z.,** Politis, D. J., Luan, X., Chen, G., Wang, L., 2019. Springback characteristics of UHSS for warm u-shape bending: experiments and FE simulation. *38th International Deep-Drawing Research Group Conference*. 3-7 June 2019, Enschede, Netherlands. Doi:10.1088/1757-899X/651/1/012055

Liu, X., Fakir, O. EI., **Cai, Z.,** Gharbi, M. M., Dalkaya, Baransel., Wang, L., 2019. Development of an interfacial heat transfer coefficient model for the hot and warm aluminium stamping processes under different initial blank temperature conditions. *J. Mater. Process. Technol*. DOI: 10.1016/j.jmatprotec.2019.05.026

Sun, Y., Wang, K., Politis, D. J., **Cai, Z.,** Wan, L., Wang, Y., Wang, L., 2018 A novel stamping process of 60Si2Mn steel disc springs. *Advanced high strength steel and press hardening*. 295-300. Doi: 10.1142/9789813277984_0046

Yu, X., Jiang, Y., Yang, X., **Cai, Z.,** Hua, Y., Yang, S., Wang, H., Liu, X., Wang, L., 2020. Dodecanethiol coated muti-walled carbon nanotube films as flexible current collector for lithium-ion batteries. *Materials Letters* (Under Review)

Zhang, Q., Luan, X., Dhawan, S., Politis, D.J., **Cai, Z.,** Wang, L., 2018. Investigating the quench sensitivity of high strength AA6082 aluminium alloy during the new FAST forming process. *IOP Conf. Ser. Mater. Sci. Eng*. 418, 12028.

Patents:

Cai, Z., Fakir, O. EL., Dhawan, S., Zhang, Q., Sun, Y., Luan, X., Wu, G., Wang, L., 2019. A data guided approach to manufacturing light-weight components. Patent application number: CN201910786108.0

Cai, Z., Liu, X., Dhawan, S., Fakir, O. El., Lin, J., Wang, L., 2019. A Compact Automatic Simulating Facility for Non-Isothermal Forming Processes. Patent application number: CN201911035650.9

Cai, Z., Liu, X., Zhang, Q., Wu, G., Zhu, M., Wang, L., 2020. Method of forming parts from tailor-welded blanks manufactured by dissimilar alloys. Patent application number: CN2020xxxxxxxxx (Under Review)

Sun, Y., **Cai, Z.,** Ji, K., Luan, X., Liu, X., Fakir, O. EL., Wang, L., 2017. Fast warm stamping of ultra-high strength steel sheets, Patent number: WO/2019/038556.

Sun, Y., **Cai, Z.,** Luan, X., Politis, D. J., Fakir, O. EL., Lin, J., Ying, Q., Wang, L., 2019. Method of forming parts from reinforced thermoplastic composites. Patent application number: CN201910707800.X

Luan, X., Sun, Y., Zhang, Q., **Cai, Z.,** Fakir, O. EL., Wu, G., Lin, J., Wang, L., 2019. A device for simulating the hot stamping process of a sheet. Patent application number: CN201910707785.9

Industrial project report:

Cai, Z., Lin, J., Wang, L., 2017. Single point incremental forming of aluminium alloy AA5754. Report No: CALT-2017-06-27. *Confidential*

Cai, Z., Liu, X., Lin, J., Wang, L., 2018. Production of floor enforcement part by using single point incremental forming. Report No: SiFang-2018-06-08. *Confidential*

Cai, Z., Zhang, Q., Zheng, Y., Liu, J., Wang, L., 2018. Report of prospect analysis for hot stamping of lightweight component. Report No: HAS-2018-12-28. *Confidential*

Cai, Z., Lin, J., Wang, L., 2019. Summary of lightweight manufacturing technologies for new energy vehicles. Report No: HAS-2019-09-11. *Confidential*

Cai, Z., Dhawan, S., Lin, J., Wang, L., 2019. Development of FAST production line in industrial testing scale. Report No: HAS-2019-11-11. *Confidential*

Cai, Z., Dhawan, S., Lin, J., Wang, L., 2019. Annual activity report. Report No: HAS-2019-12-20. *Confidential*

Abbreviation

AA	Aluminium Association
ASF	Audi Space Frame
BIW	Body-in-White
CCP	Continuous Cooling Precipitation
CMM	Coordinate Measurement Machine
DA-TWBs	Dissimilar Alloys – Tailor Welded Blanks
DIC	Digital Image Correlation
FAST	Fast light Alloys Stamping Technology
FE	Finite Element
FEA	Finite Element Analysis
GP	Guinier-Preston
HFQ®	Solution Heat treatment, Forming and in-die Quenching
IHTC	Interfacial Heat Transfer Coefficient
MK	Marciniak-Kuczynski
OEM	Original Equipment Manufacturer
PBC	Paint Bake Cycle
PFH	Post-form Hardness
PFS	Post-form Strength
RT	Room Temperature

SHT	Solution Heat Treatment
spm	Strokes per minute
SSSS	Supersaturated Solid Solution
TC	Temperature Control
TWBs	Tailor Welded Blanks
UTS	Ultimate Tensile Strength
YS	Yield Strength

Nomenclature

English Alphabet (Uppercase)

A	Area
$B(T)$	Temperature dependent parameter
$C_p(T)$	Specific heat capacity at forming temperature
F	Force
K_{slt}	Mean thermal conductivity between the blank, forming tools and lubricant
K_{st}	Harmonic mean thermal conductivity
L	Corresponding length
L_o	Original length
N_p	Contact pressure dependent parameter
N_δ	Lubricant layer thickness dependent parameter
P	Contact pressure between the blank and forming tools

R	Molar gas constant
R_s	Surface roughness of aluminium specimen
R_t	Surface roughness of forming tools
R_{st}	Interfacial surface roughness
T	Absolute temperature in Kelvin
T_F	Forming temperature
T_R	Room temperature
T_T	Treatment temperature

English Alphabet (Lowercase)

f	Tempering correction factor
h	Overall IHTC
h_a	Air-contact IHTC
h_c	Coating-contact IHTC
h_s	Solid-contact IHTC
l	Blank thickness
t	Corresponding thickness
t_o	Original thickness

Greek Alphabet

α	Temperature dependent thermal diffusivity of the blank
δ	Engineering stress
δ_c	Tool coating layer thickness

δ_l	Lubricant layer thickness
e	Engineering strain
ε	True strain
θ	Initial deformation angle of blank contact profile
θ_A	Sidewall springback angle A
θ_B	Flange springback angle B
k_c	Thermal conductivity of the tool coating
k_l	Thermal conductivity of the lubricant
k_s	Thermal conductivities of aluminium specimen at forming temperature
$k_s(T)$	Thermal conductivity at forming temperature
k_t	Thermal conductivities of forming tools at forming temperature
$\rho(T)$	Density at forming temperature
σ	True stress
σ_U	Temperature dependent ultimate strength
$\sigma_U(Tx)$	Ultimate strength of the aluminium alloy at Tx temper
$\sigma_U(T6)$	Ultimate strength of the aluminium alloy at T6 temper

Chapter 1. Introduction

1.1 Background

A key greenhouse gas emissions reduction milestone was achieved in 2016, with the signing of the Paris Agreement by governments around the world, recognising the significance of climate change caused by greenhouse gas emissions (United Nations Climate Change, 2015). According to the transport and environmental research data shown in Figure 1.1, transportation was the greatest contributor to climate change in 2016, exceeding both power generation and industry. This is also mirrored in other regions, with the transportation sector generating the largest share of greenhouse gas emissions, at 29 % in the USA for the year 2018 (EPA, 2019). In Europe, 12 % of total carbon dioxide (CO_2) emissions were contributed by vehicles alone. Greenhouse gas emissions from transportation primarily arise from the burning of fossil fuel for cars, trucks, ships, trains, and planes as over 90 % of the fuel used for transportation is petroleum based (Metz et al., 2007). Therefore, a series of strict legislation for the automotive industry was introduced in 2017 by the European Commission, which states that vehicle emissions must be reduced from 130 grams CO_2 per kilogram in 2015 to 95 grams CO_2 per kilogram by 2021 (European Commission, 2017). Moreover, to provide incentives for car manufacturers to meet these targets, large penalties are applied for each gram in excess of the CO_2 emissions limit.

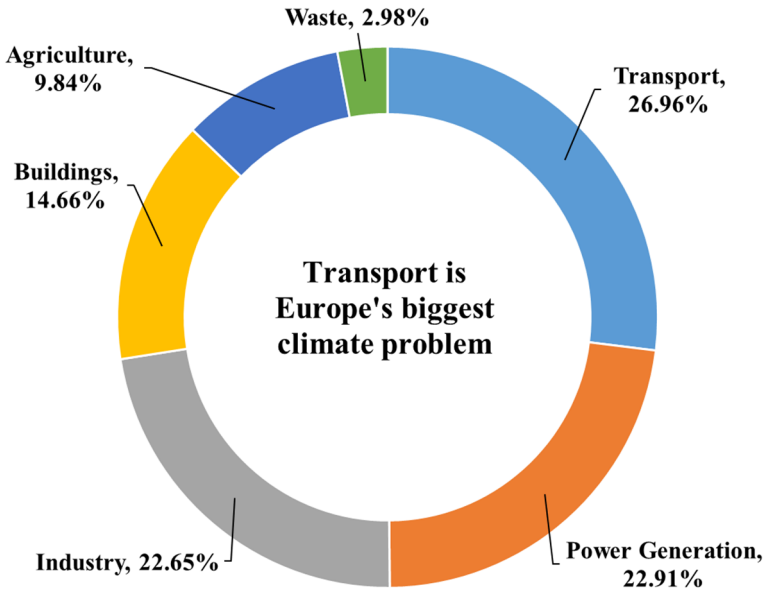

Figure 1.1 EU Greenhouse gas emissions per sector in 2016 (Grelier, 2018).

Therefore, there are three main methods currently being used by automotive OEMs (Original Equipment Manufacturer) to meet these targets:

1. Reduce the weight of BIW (Body-in-White) – using lighter materials;
2. Improve engine efficiency - burning less fuel with additional range;
3. Replacing internal combustion engines with electric motors – hybrid and electric cars.

According to the literature, the reduction of weight for BIW is the most efficient way to achieve the government regulations, with aluminium alloys being good lightweight alloy candidates to replace heavy steels (Lutsey and Sperling, 2005). In addition, the application of lightweight aluminium alloys is beneficial for reducing CO_2 emissions and saving fuel consumption. It was found that the carbon dioxide emission could be reduced by 10 % when a vehicle structure was made from aluminium alloys instead of conventional steels (Ungureanu, C.A. et al., 2007).

1.2 Aluminium alloys for automotive applications

Aluminium alloy sheets have been widely applied in vehicles due to their high strength-to-weight ratio, corrosion resistance, good recyclability and weldability (Antunes and de Oliveira, 2014). The usage of the aluminium alloys (AL 5000/6000 plus Aluminium/High Strength) in vehicles is continuously increasing in recent years and will dominate by the year 2040, as shown in Figure 1.2 where the usage rate of aluminium alloys in vehicle BIW is expected to increase from 4 % in 2010 to 26 % in 2040 (Smith, 2017).

In 2017, the carmaker Audi introduced the first Audi Space Frame (ASF) in the model A8 shown in Figure 1.3, that combines aluminium, steel, carbon fibre and magnesium to deliver stiffness and safety (Torque Tips, 2017). The ASF in the new model mainly consists of aluminium, at 58 % of the total material used. Most significantly, the structure is 24 % stiffer but 30 % lighter compared with the previous generation model. However, due to cost constraints, only premium segment cars such as the Audi A8 and Jaguar XF currently have aluminium bodies (European Aluminium, 2017). The most expensive aspect of aluminium components is the forming technique used, and therefore a low cost and high production rate sheet metal forming process is urgently required.

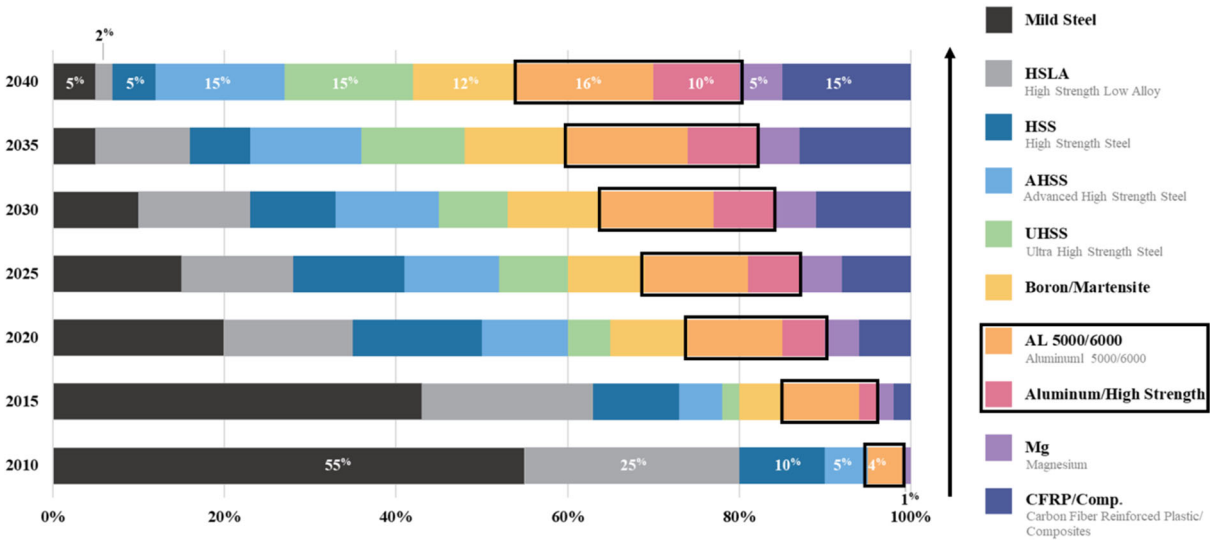

Figure 1.2 Material usage in vehicles from 2010 to 2040 (Smith, 2017).

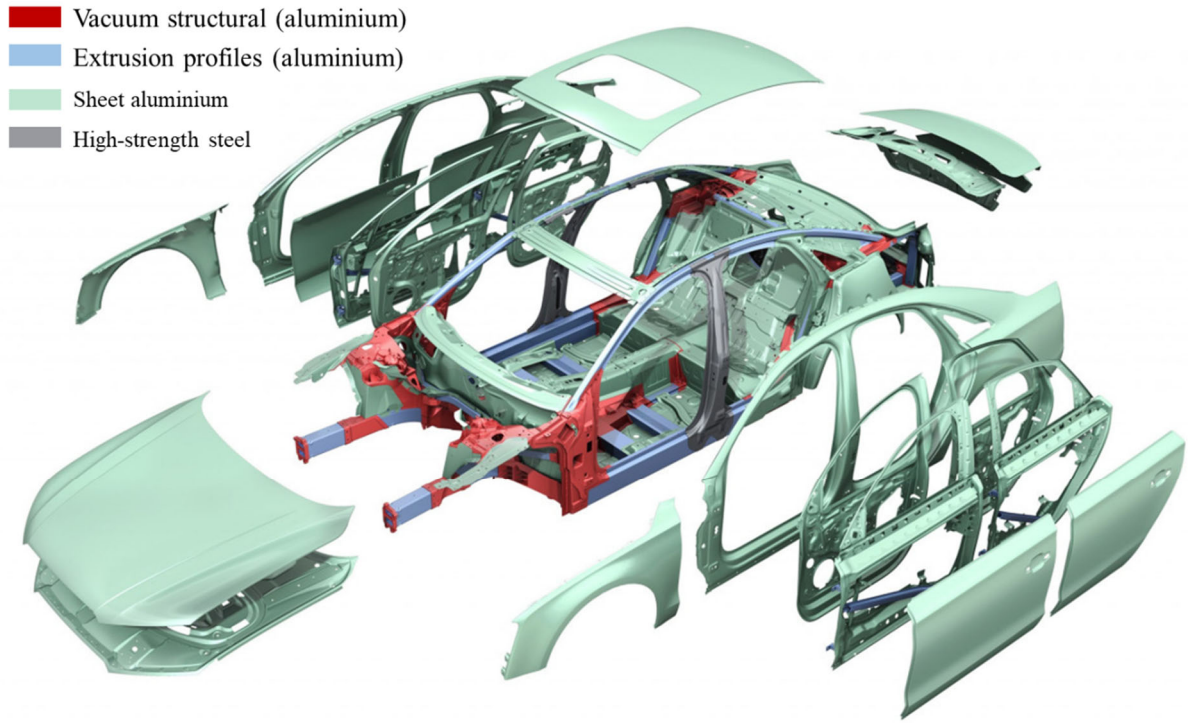

Figure 1.3 Body part materials in Audi A8 (Torque Tips, 2017).

In addition to using aluminium alloys to reduce vehicle weight, the application of Tailor Welded Blanks (TWBs) could further reduce the overall mass and improve the overall structural stiffness by using Dissimilar Alloys - Tailor Weld Blanks (DA-TWBs) (Merklein et al., 2014). Traditionally, a car assembly is produced by forming multiple components and then welding together. Nowadays, with the introduction of TWBs, the sheet blanks are welded together before the forming process begins, and therefore only a simple forming process is

required. Figure 1.4 shows an exploded view of potential vehicle components formed by using TWBs (Arcelor Mittal, 2010). Kinsey and Wu (2011) summarised the advantages of using TWBs in not only reduced vehicle weight and improved stiffness but also decreased noise, improved dimensional accuracy and improved corrosion resistance.

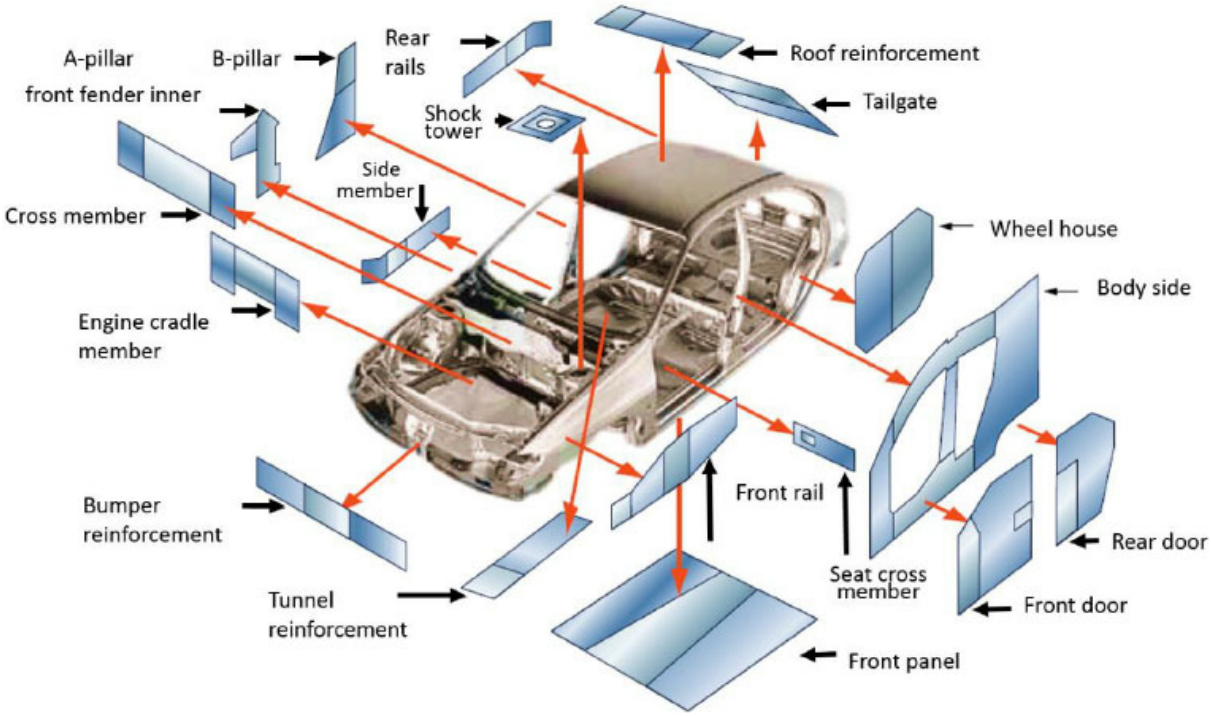

Figure 1.4 The main applications of tailor welded blanks and patchwork blanks in a car body-in-white (Arcelor Mittal, 2010).

Previously, research focused on Steel to Steel TWBs with different thickness and mechanical properties (Gaied et al., 2009, Xu et al., 2014). However, due to weight saving requirements for passenger cars, a growing number of OEMs and researchers have investigated the application of Aluminium to Aluminium TWBs. According to the research made on the ductility of similar and dissimilar Aluminium to Aluminium TWBs, it was found that the formability is highly dependent on the different mechanical properties of the base materials (Leitão et al., 2009, Liu et al., 2015b, Liu et al., 2015c). In addition, poor formability occurs at room temperature due to the limited ductility of the base aluminium alloys especially at the weld zone (Feistauer et al., 2014). Nevertheless, studies suggested that forming TWBs at elevated temperatures enhance the formability and improve the post-form strength (Bhanodaya Kiran Babu et al., 2014). Therefore, a suitable forming process at hot and warm condition was desired.

1.3 Manufacturing methods for aluminium alloy components

Cold, hot and warm stamping are forming techniques commonly used in the automobile industry to form aluminium alloy sheets into structural components. However, the low formability of aluminium alloys at room temperature significantly limits their application in complex-geometry components.

In order to overcome the drawback of low formability of aluminium alloys at room temperature, hot and warm stamping technologies were developed (Karbasian and Tekkaya, 2010, Toros et al., 2008). Solution Heat treatment, Forming and in-die Quenching (HFQ®) technology was applied in the literature (El Fakir et al., 2014), in which an AA5754-H111 blank with 1.5 mm thickness was first heated in a furnace to its solution heat treatment temperature of 480˚C at a heating rate of 1˚C/s, followed by a transfer from the furnace to a press machine within 10 seconds. Subsequently, the cold forming tools deformed the hot blank at a stamping speed of 250 mm/s into the desired shape. A different hot stamping process was used in the study of (Maeno et al., 2017). Specifically, a 1.3 mm thick 2025 aluminium alloy blank in the T4 state was electrically-resistance heated to a target temperature lower than its solution heat treatment temperature, and then quickly transferred to a press machine within 0.2 seconds, followed by deformation in cold forming tools.

However, it is challenging to improve the production rate and achieve further cost savings in these forming technologies. Moreover, there are significant challenges in current forming technologies to form dissimilar alloys, and the use of tailor welded blanks for BIW (Merklein et al., 2014) necessitates the development of novel forming technologies.

1.4 Aim and objectives of research

The present work aims to develop a novel sheet metal forming technology – Fast light Alloys Stamping Technology (FAST) for panel components from tailor-welded blanks manufactured by dissimilar alloys (DA-TWBs), whilst achieving desirable mechanical properties in a cost and time efficient way. The dissimilar alloys in this study consist of two base materials of 6xxx series Al-Mg-Si and 7xxx series Al-Zn-Mg-Cu alloys, which are joined by friction stir welding. The implementation of the proposed FAST process was conducted by forming M and U shaped panel components. A general aluminium alloy-independent model with a single set of fixed

constants was developed to predict the interfacial heat transfer coefficient (IHTC) evolutions and was applied to simulate the temperature evolutions during FAST forming processes. A software agnostic platform, Smart Forming, was developed to provide cloud FEA of FAST processes as well as solutions for specific demands by operating model-driven functional modules. The following list of objectives was conducted to realise the aim of this work:

- Investigate thermo-mechanical properties through experimentation on AA6082 and AA7075 alloys including uniaxial tensile tests and strength degradation tests.
- Develop a further understanding of the influence of processing parameters on thermo-mechanical properties and investigate the mechanism behind it.
- Validate the FAST process by forming U-shaped components and evaluate the influence of the processing parameters on post-form and paint bake cycle (PBC) properties of formed components.
- Develop a general aluminium alloy-independent model to predict the IHTC evolution during the FAST process.
- Verify the developed IHTC model by forming M-shaped dissimilar alloy components under FAST forming conditions.
- Develop a cloud FE analysis platform for hot and warm stamping processes which aims to reduce the product development cycle.
- Verify the developed platform with M-shaped forming using FAST.

1.5 Major tasks

To achieve the research objectives, the following major tasks were completed:

1. Review of the state-of-art technologies for aluminium alloys (with the emphasis on AA6xxx and AA7xxx) and tailor welded blanks.

2. Review of the state-of-art forming technologies for aluminium alloys. Particular attention was paid on hot and warm stamping processes.

3. Review of the effect of forming temperature (blank temperature), heating rate, soaking time and quenching rate on mechanical properties of AA6xxx and AA7xxx, and the precipitation hardening evolution during the hot and warm stamping processes.

4. Review of the IHTC including value determination, test facility, inflectional factors and model with validation.

5. Review of the state-of-art FE simulation for hot and warm stamping processes.

6. Conducted uniaxial tensile tests to understand the flow behaviour and ductility of the AA6082 and AA7075 at various blank temperatures and strain rates.

7. Conducted simple strip forming tests with designed forming simulator to evaluate the effect of post-PBC strength at various forming temperatures, heating rates, soaking times, and quenching rates on FAST.

8. Conducted U-shaped forming tests using a dedicated pilot production line to validate the feasibility of the FAST with the AA6082, AA7075 and DA-TWBs respectively.

9. Evaluated post-PBC strength of the components formed by using FAST. The effect of forming temperature and forming speed on springback was investigated.

10. Developed a finite element (FE) model of the U-shaped FAST forming process in PAM-STAMP and verified the FE model with experimental results.

11. Developed a general aluminium alloy-independent model with a single set of fixed constants to predict the IHTC during the FAST forming process.

12. Identified the critical processing parameters in terms of the desired post-PBC strength by integrating the temperature evolution of AA6082 and AA7075 in FAST forming which was simulated by applying the predicted IHTC evolution with the continuous cooling precipitation diagram.

13. Conducted M-shaped forming using DA-TWBs to validate the feasibility of critical processing parameters and verify the developed IHTC model by measuring the post-PBC hardness.

14. Developed a cloud FE analysis platform to simulate the FAST process combined with Pre-FE, FE and Post-FE. This aims to improve efficiency and reduce human effort while using conventional FE simulation packages.

15. Conducted two case studies to verify the developed platform with M-shaped forming under FAST conditions

1.6 Thesis structure

In this thesis, the novel forming technology '*FAST*' was developed to form complex-shaped components from aluminium alloys and DA-TWBs with reduced cycle time and improved cost efficiency. The chapters of this thesis cover the work that was performed to complete these objectives.

Chapter 2 provides the literature review on aluminium alloys, the state of art for sheet metal forming technologies, precipitation hardening processes of aluminium alloys, IHTC and FE simulation during the forming process.

Chapter 3 introduced the concept of the FAST process and presented the experimental methodologies of uniaxial tensile tests, strength evaluation test and FAST forming test.

Chapter 4 discusses the analysis of the experimental results. The effect of temperature and strain rate on the thermo-mechanical properties are explored. A discussion of the relationship between post-PBC hardness and mechanical properties is provided. In addition, a novel FAST process with U-shaped forming with AA6082, AA7075 and DA-TWBs were also developed. A study of springback of the formed components at various temperatures and forming speeds are given. Moreover, an FE model is developed and experimentally verified.

Chapter 5 presents an aluminium alloy dependent model developed to predict the IHTC evolution during the FAST process, that explored the relationship between die contact force and post-PBC hardness. The optimised forming parameters during the FAST process are also verified by manufacturing M-shaped components with DA-TWBs.

Chapter 6 presents a cloud FE analysis platform, Smart Forming, that was developed. Cloud FEA of a FAST forming process for component made from AA6082 was performed and subsequently experimentally verified.

Chapter 7 concludes the thesis with a summary of the work conducted and suggestions for future work. Figure 1.5 shows a schematic diagram of the key contributions for this thesis.

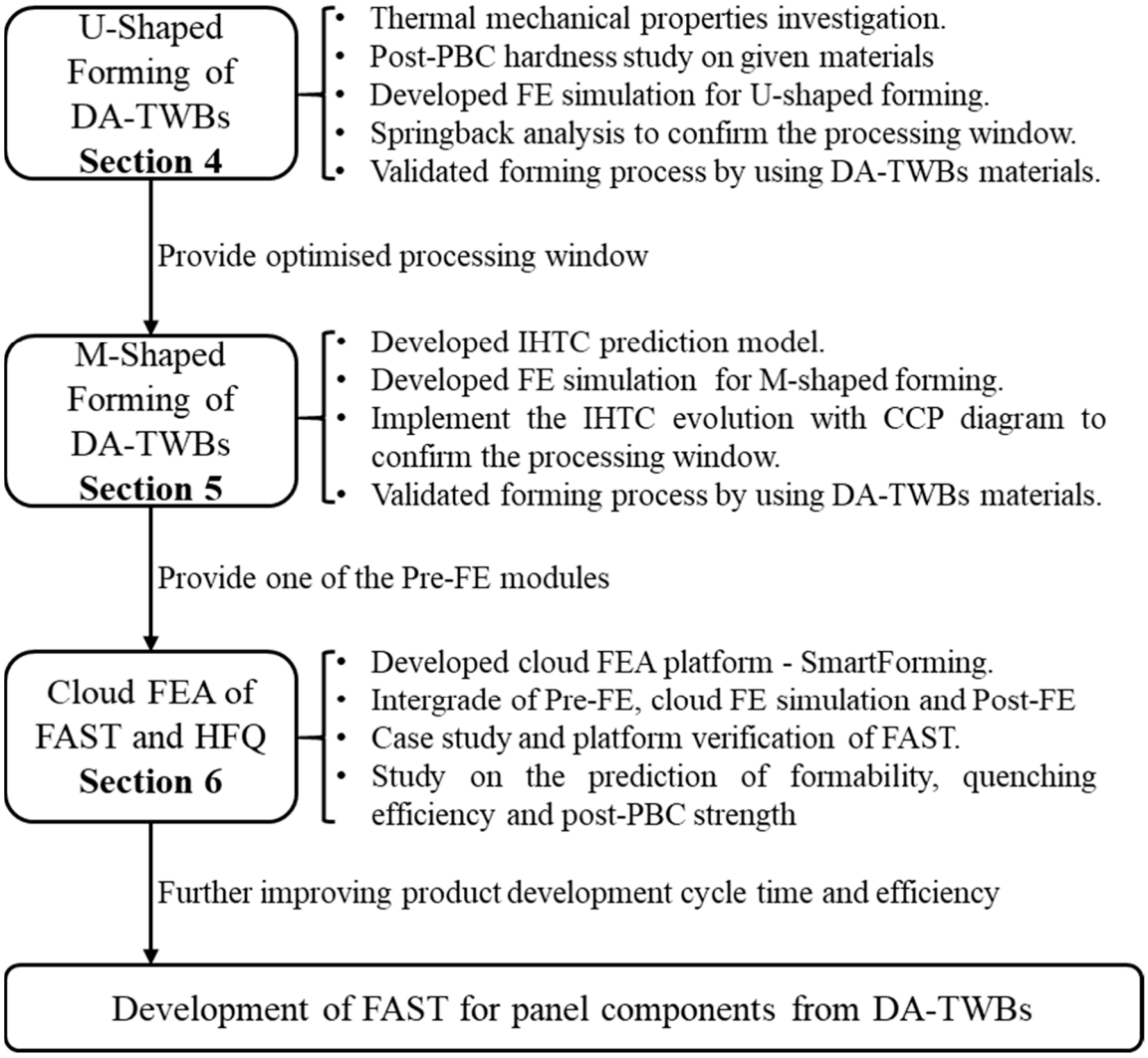

Figure 1.5 Schematic diagram for the key contribution of the thesis.

Chapter 2. Literature review

In this chapter, the literature on the state-of-art aluminium alloy and sheet metal forming technologies are reviewed. In order to develop a novel sheet metal forming technology, a detailed scientific investigation was conducted on a range of aluminium alloys. In particular, 6xxx and 7xxx series aluminium alloys and TWBs were the main focus of this research. To address the commonly used industrial sheet metal forming technologies, variations of cold, warm and hot stamping were reviewed. For each technology, material behaviour such as the precipitation hardening process, IHTC and the implantation of multi-objective FE simulation for hot and warm stamping of aluminium alloys were also reviewed. This chapter aims to provide an overview of the development of sheet metal forming technology for aluminium alloy panel components, with the structure of this chapter shown in Figure 2.1.

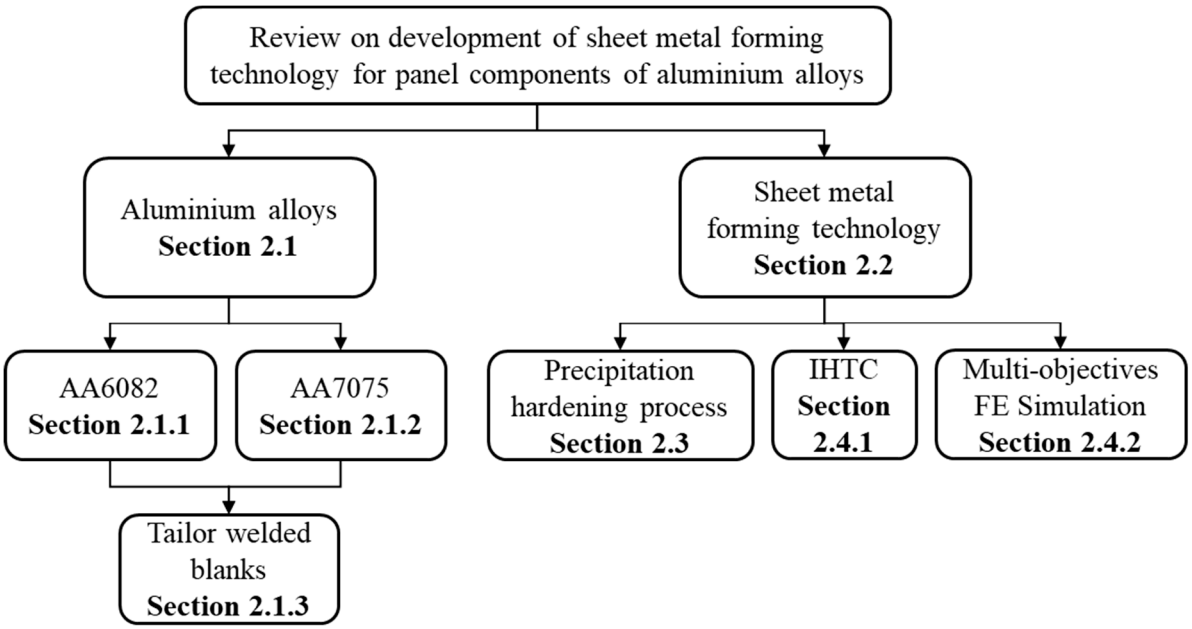

Figure 2.1 Schematic diagram for major sections covered in Chapter 2.

2.1 Aluminium alloys

Nowadays, commercial aluminium alloys can be defined within two main categories, namely, casting alloys and wrought alloys. Normally, casting alloys are mainly used for the product (part) that has non-uniform thickness, for example the head of engine cylinder and housing for a gearbox (Kaufman, 2000). Wrought alloys with their good mechanical properties and surface

finish are mainly used for a product (part) that has complex-shape on the structure (Polmear, 1995). Wrought alloys are broadly classified according to the International Alloys Designation System with a four-digit number introduced as shown in Table 2.1.

Table 2.1 The international wrought aluminium alloy designation system (Davis, 1993).

Alloys series	Major alloying element(s)	Heat-treatable?
1xxx	Minimum 99 % of aluminium	No
2xxx	Copper	Yes
3xxx	Manganese	No
4xxx	Silicon	No
5xxx	Magnesium	No
6xxx	Magnesium and Silicon	Yes
7xxx	Zinc, Magnesium and Copper	Yes
8xxx	Other (e.g. Ni, Ti, etc)	-

According to Table 2.1, the wrought aluminium alloys can be further classified into two types as either heat-treatable or non-heat-treatable alloys (Davis, 1993), where 1xxx, 3xxx, 4xxx and 5xxx series aluminium alloys are defined as non-heat-treatable alloys whereas heat-treatable alloys include 2xxx, 6xxx and 7xxx series aluminium alloys. Cold working is most commonly used in strengthening non-heat-treatable alloys while heat-treatable alloys are highly depending on the temperature. The strength of heat-treatable alloys can be significantly improved by conducting the heat treatment process which includes solution heat treatment, quenching and natural ageing or artificial ageing.

Nevertheless, the specific temper designation is normally displayed following the series number of the aluminium alloy. The most common tempers are summarised in Table 2.2.

As shown in Figure 2.2, the production of commercial aluminium sheet consists of 6 main steps, where the casted ingot is homogenously preheated and follows multiple hot rolling processes. Once hot rolling is completed the H temper of sheet metals could be formed by cold rolling. The lowest strength of material occurs at O temper where the sheet material is unwound from the coil and passed through a continuous annealing line. During the annealing process, the material is heated to above recrystallization temperature and soaked for a specific time, then

quenched immediately to form an unstable W temper. In order to obtain maximum age-hardening response, natural ageing at room temperature or artificial ageing at a temperature is required between 160 and 200 °C (Engler and Hirsch, 2002).

Table 2.2 Temper designation for wrought and cast aluminium alloys (British Standards, 2017).

Tempers	Description
H Temper	Strain-hardened - cold worked after annealing
O Temper	Annealed – the lowest strength temper
W Temper	Solution heat treated – unstable temper normally called 'as-quenched'
T Temper	Heat treated to produce stable tempers, e.g. T4 – Solution heat-treated and natural aged; T6 – Solution heat-treated and artificial aged

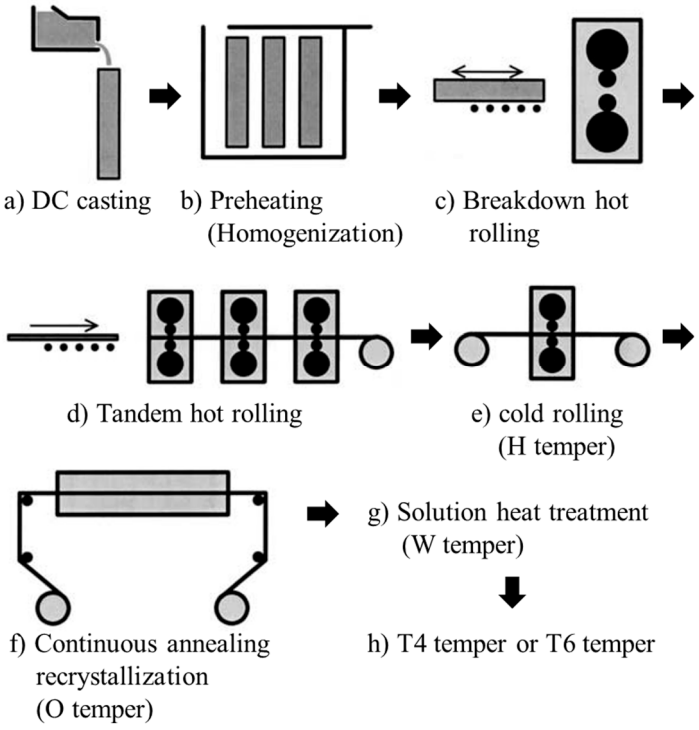

Figure 2.2 Schematic diagram for typical steps of sheet aluminium alloy production (Engler and Hirsch, 2002).

In this research, the heat treatable high strength 6xxx and ultra-high strength 7xxx series sheet aluminium alloys were used as the raw materials with a thickness of 2 mm, as both have fantastic weldability, formability and corrosion resistance.

2.1.1 Aluminium-Magnesium-Silicon (Al-Mg-Si) alloy

Al-Mg-Si alloy has become a popular material used in car structure and body panel manufacturing due to its excellent corrosion resistance and lightweight potential. This alloy is also known as 6xxx series aluminium alloy or AA6xxx. Nowadays, more than 70 types of Al-Mg-Si alloys have been recorded and registered with the aluminium association (Sato and Matsuda, 2003). In 1921, the first commercial AA6051 was introduced to the world (ASTM, 1936). However, due to the low performance of corrosion resistance and strength response to heat treatment, AA6051 failed to attract significant usage. Nine years later, AA6061 was developed to fulfil the commercial requirements and the utilization rate significantly increased by 1930. The material was further improved in 1947 by the development of finer grain sizes after cold working and was named AA6062 (Sanders, 2001).

Figure 2.3 illustrates the classification of AA6xxx-T6 based on different composition ratio between Mg and Si with the corresponding yield strength(Polmear et al., 2017). It is clear to see that the AA6xxx alloy series covers a broad range of yield strength in the range between 150 and 300 MPa at T6 temper, especially the AA6082 which has the greatest strength performance at over 300 MPa when a high weight percentage of both Mg and Si is present. As strength may vary significantly due to the different percentage of alloy composition, car body panels (inner and outer) are normally formed by using AA6060 and AA6061, while AA6082 is mostly used for structural components such as the front door ring and cross member front bulkhead (Mallick, P.K., 2010).

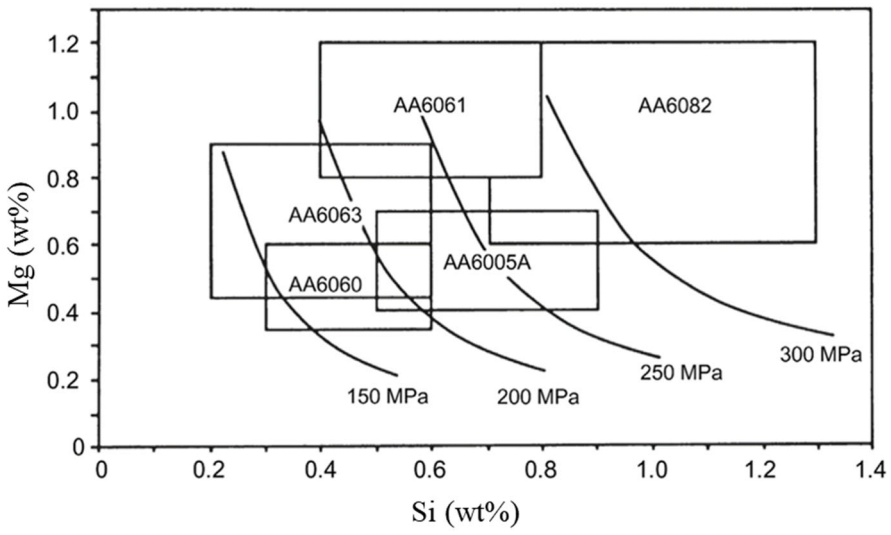

Figure 2.3 The classification of AA6xxx-T6 on different composition ratio between Mg and Si with the corresponding yield strength (Polmear et al., 2017).

2.1.2 Aluminium-Zinc-Magnesium-Copper (Al-Zn-Mg-Cu) alloy

AA7xxx alloy (Al-Zn-Mg-Cu based material based) is an ultra-high strength aluminium alloy with yield strength exceeding 500 MPa. The detailed chemical compositions of commercial AA7xxx grades are listed in Table 2.3.

Table 2.3 Temper designation for wrought and cast aluminium alloys (Campbell, 2006).

Alloy	Si	Fe	Cu	Mn	Mg	Cr	Zn	Ti	Zr
AA7020	0.35	0.4	0.2	0.05-0.5	1.0-1.4	0.1-0.35	4.0-5.0	-	0.08-0.2
AA7050	0.12	0.15	2-2.6	0.1	1.9-2.6	0.04	5.7-6.7	0.06	0.08-0.15
AA7055	0.1	0.15	2-2.6	0.05	1.8-2.3	0.04	7.6-8.4	0.06	0.08-0.25
AA7075	0.4	0.5	1.2-2	0.3	2.1-2.9	0.18-0.28	5.1-6.1	0.2	-
AA7079	0.3	0.4	0.4-0.8	0.1-0.3	2.9-3.7	0.1-0.25	3.8-4.8	0.1	-
AA7085	0.06	0.08	1.3-2	0.04	1.2-1.8	0.04	7-8	0.06	0.08-0.15
AA7150	0.12	0.15	1.9-2.5	0.1	2-2.7	0.04	5.9-6.9	0.06	0.08-0.15

The excellent performance of corrosion resistance, yield strength, machinability, weldability and fracture toughness for AA7xxx alloys (such as AA7010, AA7050 and AA7075) were obtained from the addition of zinc, magnesium and copper (Campbell, 2006, Heinz et al., 2000, Prabhu, 2015). AA7xxx alloys are widely used in the aerospace industry due to their superior material performance, where common aircraft applications included wing ribs, wing stiffener and fuselage (Dursun and Soutis, 2014, Prabhu, 2015, Warner, 2006). In 1940, the first commercial AA7075 was introduced to the world which rapidly began to replace other types of alloys in the aerospace industry such as AA2xxx alloys (Wanhill, 2014). Recently, an increasing number of automobile applications have utilised AA7075 to achieve yield strengths and ultimate tensile strengths greater than 450 and 510 MPa respectively, in order to achieve lightweight designs and improved car body-in-white strength (The Aluminum Association, 2015). In addition, the application of AA7075 in automotive components has been extended to safety-critical parts such as A and B-pillars and bumpers.

2.1.3 Tailor welded blanks

In addition to using aluminium alloys to reduce vehicle weight, the application of Tailor Welded Blanks (TWBs) could further reduce the overall mass and improve the overall structural stiffness by using Dissimilar Alloys - Tailor Weld Blanks (DA-TWBs) (Merklein et al., 2014) Traditionally, a car assembly is produced by forming multiple components and then welding together. Nowadays, with the introduction of TWBs, the sheet blanks are welded together before the forming process begins, and therefore only a simple forming process is required. Figure 2.4 shows an exploded view of potential vehicle components formed by using TWBs (Arcelor Mittal, 2010), the advantages of using TWBs include not only reduced vehicle weight and improved stiffness but also decreased noise, improved dimensional accuracy and improved corrosion resistance (Kinsey and Wu, 2011).

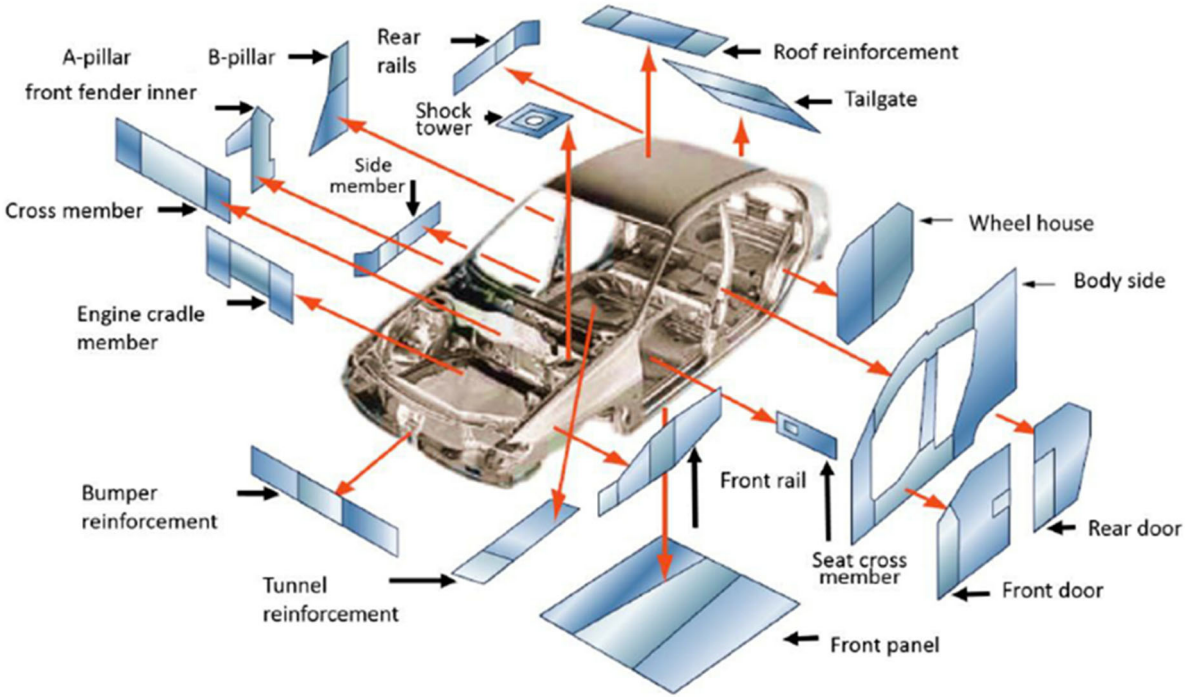

Figure 2.4 The main applications of tailor welded blanks and patchwork blanks in a car body-in-white (ArcelorMittal, 2010).

TWBs are made of blanks of various materials or thickness combinations, where the blanks are welded prior to deformation (Kinsey and Wu, 2011). The use of TWBs allows parts to be formed in a more efficient manner. Different welding methods can be used to weld two base materials together, which includes arc welding, tungsten inert gas welding (Tarng et al., 1999), laser beam welding (Boukha et al., 2012) and friction stir welding (Mishra and Ma, 2005).

Although laser beam welding is the most common welding method, the high reflectivity of aluminium alloys makes the process difficult to control and makes the composition and microstructure of the weld zone difficult to predict with heat-treatable alloys due to the high temperature effect. Fiction stir welding is the most applicable method for ultra-high/high strength aluminium alloys such as AA7xxx and AA6xxx, as the effect of melting and solidify of parent materials are controllable during the welding process (Buffa et al., 2007).

Previously, research focused on Steel to Steel TWBs with different thickness and mechanical properties (Gaied et al., 2009, Xu et al., 2014). However, due to weight-saving requirements for passenger cars, a growing number of OEMs and researchers have investigated the application of Aluminium to Aluminium TWBs. According to the research made on the ductility of similar and dissimilar Aluminium to Aluminium TWBs, it was found that the formability is highly dependent on the different mechanical properties of the base materials (Leitão et al., 2009, Liu et al., 2015b, Liu et al., 2015c). In addition, poor formability occurs at room temperature due to the limited ductility of the base aluminium alloys especially at the weld zone (Feistauer et al., 2014). Nevertheless, studies suggested that forming TWBs at elevated temperatures enhance the formability and improve the post-form strength (Bhanodaya Kiran Babu et al., 2014). Therefore, a suitable forming process at hot and warm conditions is desired.

2.2 Forming technologies of aluminium alloys for thin-wall components

In order to meet the increasing demands for weight reduction and maintain constant vehicle size and safety performance, a wide range of high and ultra-high strength aluminium alloys have been used in the automotive industry. Mass production of vehicles has become one of the challenges for carmakers as there are increased demands for aluminium sheet components of added shape complexity and improved mechanical properties (Ramezani and Ripin, 2012). To overcome this challenge, advanced, efficient and economical sheet metal forming technologies for aluminium alloys such as cold, warm and hot stamping have been commonly utilised and are reviewed.

2.2.1 Cold stamping

Cold stamping using rigid dies is currently the most common forming technique used for forming aluminium sheet components in the automotive industry, especially for non-heat treatable AA5xxx and heat treatable AA6xxx (Zheng et al., 2018). AA5754 and low-strength AA6xxx in the T4 and W-temper exhibit lower strength (relatively good formability) at room temperature conditions (Polmear, 2005, Sáenz de Argandoña et al., 2015). However, further additional heat treatment may be applied to improve the strength of heat treatable materials to T6 temper (Zheng et al., 2018). However, conventional cold stamping is difficult for forming high strength aluminium alloys into complex shapes due to the lower formability as a result of insufficient heat treatment. Figure 2.5 illustrates additional disadvantages to cold stamping including excessive springback and poor forming profile of the formed component, which will result in additional issues such as a reduced tool life and significant tool wear such as galling (Fan et al., 2015, Wang et al., 2017). Therefore, forming complex shaped components from high strength sheet aluminium alloys with warm and hot stamping is much more preferable than cold stamping.

Figure 2.5 Cold stamping drawback a) Springback and b) shape distortion (Fan et al., 2015, Wang et al., 2017, Zheng et al., 2018).

2.2.2 Warm stamping

Warm forming is performed at temperatures lower than the recrystallization temperature, in the range of 150 to 350 °C, while hot forming is performed above the recrystallization temperature (Harrison et al., 2015). It can either be performed in isothermal (heated punch and die with hot blank) or non-isothermal (cooled punch and die with hot blank) conditions. Isothermal conditions are normally utilised, however, formability was also shown to improve by generating temperature gradients in the sheet being deformed by partially heating the tools (Li and Ghosh, 2004). The first commercialized warm forming solution in Europe was AMAG TopForm® UHS used to produce the side impact beams in the BMW i8 from high strength

AA7075 (Grohmann, 2016). Warm stamping offers a large increase on material ductility and forming limit and the potential to reduce springback compared with cold stamping (Abedrabbo et al., 2006a, Kim and Koç, 2008, Shi et al., 2012). On the other hand, warm stamping may be unsuitable for high-strength heat treatable aluminium alloys as the heating might affect the microstructure and post-form strength of the alloys (Kumar et al., 2013). However, this drawback has been overcome by using the ultra-fast heating method presented within the current research.

2.2.3 Hot stamping

Hot stamping can increase the formability and reduce springback, but it destroys the desirable microstructure. A post-forming heat treatment (Solution heat treatment - SHT) is thus required to restore the microstructure, although it results in the distortion of the formed components during quenching after the SHT. These disadvantages are also encountered in forming engineering components from other materials. In an effort to overcome these disadvantages, various studies have been undertaken and special processes have been developed to address particular issues in forming particular types of components. Solution Heat treatment, Forming, and in-die Quenching, or HFQ® (Foster et al., 2010, Imperial College London, 2020), is a hot forming process that was developed to enable the production of complex-shaped lightweight components from aluminium alloys.

The HFQ® process is shown in Figure 2.6 consists of heating an aluminium alloy sheet blank to its SHT temperature so that its metallurgical structure becomes a homogeneous solid solution with high ductility and hence good formability. The blank is then transferred to a press for stamping. The formed part is then held in the water-cooled tool for a few seconds to quench it to avoid the formation of precipitates (Imperial College London, 2020).

The HFQ® process combines material heat treatment, die-forming and quenching in one operation. This reduces production steps and facilitates the stamping of high strength, high precision, and complex-shaped lightweight Al-alloy panels in an efficient and cost-effective way (Foster et al., 2010). Consequently, this novel technology has paved the way to achieving a component price which makes possible the widespread adoption of Al-alloy panel parts on medium and high volume vehicles. The HFQ® process uses standard grades of aluminium sheets (5xxx, 6xxx and 7xxx series), which can be formed into shapes as complex as those produced in sheet steel (Wang et al., 2011). Press forces required are significantly lower than

those used for steel parts, which reduces pressing energy. Being able to produce large complex shapes in a single pressing reduces fabrication costs by reducing the need for joining enabling cost-competitive chassis and body assemblies (Imperial College London, 2020).

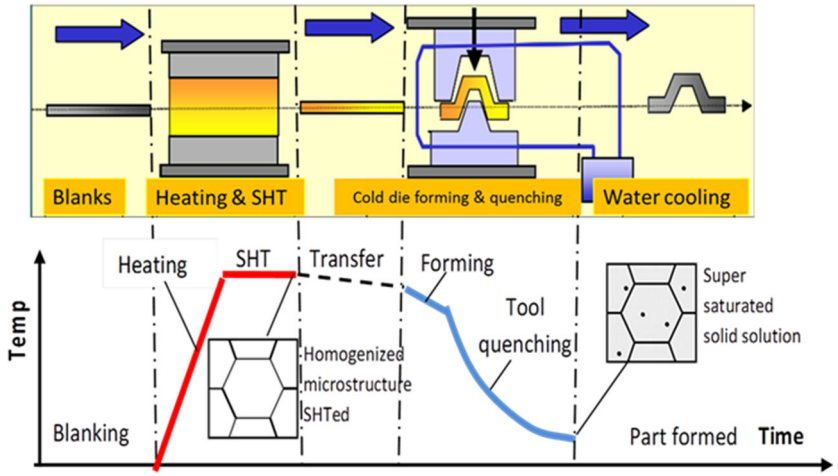

Figure 2.6 Schematic diagram of the HFQ forming process (Imperial College London, 2020).

In order to overcome the drawback of low formability of aluminium alloys at room temperature, HFQ® technology was applied in the literature (El Fakir et al., 2014), in which an AA5754-H111 blank with 1.5 mm thickness was first heated in a furnace to its solution heat treatment temperature of 480 ˚C at a heating rate of 1 ˚C/s, followed by a transfer from the furnace to a press machine within 10 seconds. Subsequently, the cold forming tools deformed the hot blank at a stamping speed of 250 mm/s into the desired shape. A different hot stamping process was used in the study of (Maeno et al., 2017). Specifically, a 1.3 mm thick 2025 aluminium alloy blank in the T4 state was electrically-resistance heated to a target temperature lower than its solution heat treatment temperature, and then quickly transferred to a press machine within 0.2 seconds, followed by deformation in cold forming tools.

2.2.4 Post-form strength and springback under warm/hot forming

2.2.4.1 Post-form strength

In order to achieve a high post-form strength of the formed components, considerable efforts have been made to study and optimise the processing parameters in the forming processes. It has been proven that the post-form strength of the aluminium alloys was fully retained after artificial ageing at a fast heating rate of approximately 120˚C/s. However, it decreased with decreasing heating rate and reached approximately 75% of that of the as-received materials at a slow heating rate of 3˚C/s. The solid solution of the aluminium alloy was maintained, and

only small clusters were dissolved at a fast heating rate. As a result, the post-form strength increased with increasing heating rate (Maeno et al., 2017). A similar effect was also observed in the study of Zheng et al. (Zheng et al., 2019), in which the effect of forming temperature on the post-form strength of AA7075 was investigated. When the heating rate was not sufficient, the coarse particles precipitated, and their growth rates further increased with decreasing forming temperature, thus reducing the post-form strength. Although the SHT temperature ensured that all precipitates were dissolved into the aluminium matrix, the subsequent soaking time and quenching rate determined whether a Supersaturate Solid Solution (SSSS) could be obtained and thus the post-form strength of formed components could be fully retained after artificial ageing. (Fan et al., 2013) found that the post-form strength of 6A02 aluminium alloy increased from 134.7 to 315.6 MPa when the soaking time increased from 5 to 50 minutes. As a result of a better dissolution of precipitates into the aluminium matrix at a longer soaking time, the post-form strength of the aluminium alloy therefore increased. In addition, the post-form strength also increased with increasing quenching rate due to the rapid freeze of the SSSS state. Under the hot stamping conditions, the quenching rate for AA7075 has to achieve 450˚C/s to prevent secondary phase from being precipitated and thus obtain a high post-form strength after artificial ageing (Keci et al., 2014, Zhang et al., 2016).

2.2.4.2 Springback

The main challenge for high-strength aluminium alloys, is their low formability at room temperature and the subsequent springback. Springback is mainly due to the elastic recovery of sheet metal after forming, resulting in a poor net shape. Studying springback for the purposes of prediction has been investigated in cold forming conditions and is well documented in handbooks (Altan and Tekkaya, 2012, Gasson, 2003). However, springback investigations at warm and hot forming conditions are relatively few in number (Kim and Koç, 2008, Wang et al., 2017). Common industry practice is to use predictions in simulating the forming process and over bending the part to achieve the final dimensional accuracy as close as possible to the desired target. Hot and warm stamping helps to heavily reduce and, in some cases, eliminate the amount of springback experienced by the formed part. This mitigates the necessity of springback reducing methods such as over-bending.

Currently, there is a wide range of methods to identify and measure the springback. In 2011, the most commonly used method was introduced in the NUMISHEET conference to measure the springback of a post-formed U-shaped component (Kwansoo et al., 2011). Figure 2.7

illustrates the measuring method, where θ_1 is the angle between the bottom and the sidewall and θ_2 is the angle between the flange and the sidewall. In addition, there are two types of equipment used to measure the springback, including the optical scanning system (ATOS system by GOM) and the contact profile measurement system (Coordinate Measuring Machine – CMM) (Keum, Y.T. and Han, B.Y., 2002).

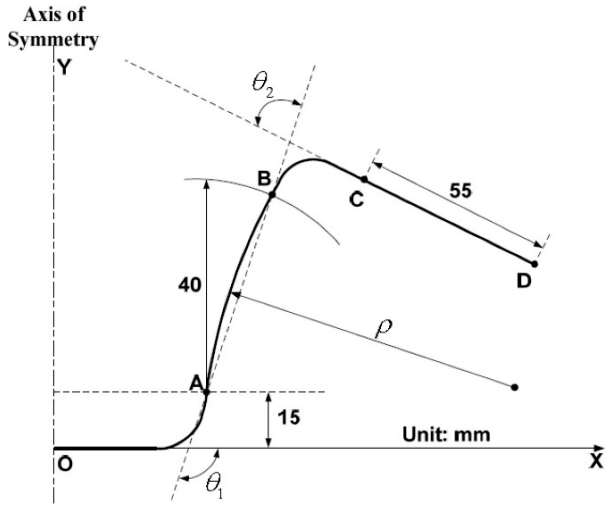

Figure 2.7 Benchmark profile and parameters of U-Shaped springback measurement (Kwansoo et al., 2011).

In the past years, many research studies have focused on the study the springback for sheet aluminium alloys under hot and warm forming processes. The effect of forming temperature (blank temperature) and forming speed (punch speed or die closing speed) are discussed in further detail below.

Springback decreases with increasing temperature, which has been found by many researchers. AA1050 sheet has been found to offer significantly decreased springback when the forming temperature was over 150 °C and rapidly decreases at a warm forming temperature in the range between 200 and 250 °C (Keum, Y.T. and Han, B.Y., 2002). A reduction of springback by up to 20% was achieved by using a hot die (200 °C) and cold punch (-10 °C) at a slow forming speed of 1 mm/s (Moon et al., 2003). The mechanical behaviour and springback of AA5754-O were investigated under warm forming conditions for cup-shaped deep drawing tests, and it was found that the tangential stress in the cup wall was the main factor affecting springback (Laurent et al., 2011).

In addition, forming speed is another important process parameter in warm and hot stamping since it not only influences the productivity but also affects the sensitivity of precipitation

hardening in heat treatable aluminium alloys (Palumbo and Tricarico, 2007). A substantial amount of research has indicated that increasing forming speed at warm forming conditions leads to a great reduction of springback (Ghosh et al., 2014, Palumbo et al., 2015, Simões et al., 2019). This was especially proven in the investigation conducted by (Simões et al., 2019) with two Al-Mg-Si alloys, to determine the effect of punch speed on the quality of forming a cylindrical cup under warm forming conditions. It was further verified that springback decreased with increasing forming speed. This is because the higher forming speed leads to higher strain rate which has a considerable effect when designing warm forming processes with heat treatable aluminium alloys.

2.2.5 Advantages and limitations of conventional forming processes

Conventional warm and hot stamping technologies have been used to improve the formability at elevated temperature for high/ultra-high strength aluminium alloys, which enables the mass production of high strength complex shaped components. In addition, springback was dramatically reduced by using these technologies, which enables for good profile accuracy of formed components.

On the other hand, the conventional warm and hot forming process is costly due to the fact that multiple heat treatment processes are used. In addition, for some of the alloys produced by conventional rolling, the solution heat treatment is up to 30 minutes, which is not suitable for automotive mass production rates and energy consumption. Moreover, the ageing process which is used to restore the strength of the formed component is highly inefficient, as it is time consuming and costly resulting in production line delays, which reduces the benefits that can be obtained from the warm and hot stamping process. Nevertheless, completed components formed by warm and hot stamping, occupy much more space than coiled sheet material from which they have been made. Therefore, relatively few parts may be aged within a given furnace at one time, which would result in poor productivity and is impractical for high volume production. Therefore, it is challenging to improve the production rate and achieve further cost savings in conventional forming technologies, hence, necessitating the development of novel forming technologies. Recently, a novel sheet metal forming process called ‘Fast light Alloys Stamping Technology (FAST)’ was developed and primarily studied for AA6082, AA7075 and DA-TWBs (Cai et al., 2019, Cai et al., 2020).

2.3 Precipitation hardening processes of 6xxx and 7xxx series aluminium alloys

Precipitation hardening or age hardening is a process that enables a supersaturated solid solution (SSSS) microstructure to gain enough driving energy to grow to finely dispersed precipitates, which enhance the mechanical properties of heat-treatable aluminium alloys. The process consists of SHT, quenching and artificial ageing (or natural ageing) as shown in Figure 2.8. In addition, precipitation hardening occurs in heat treatable aluminium alloys by forcing dislocations to either cut through small precipitates or bypass the larger ones. A large amount of research has been carried out to investigate the principal theory of precipitation hardening processes.

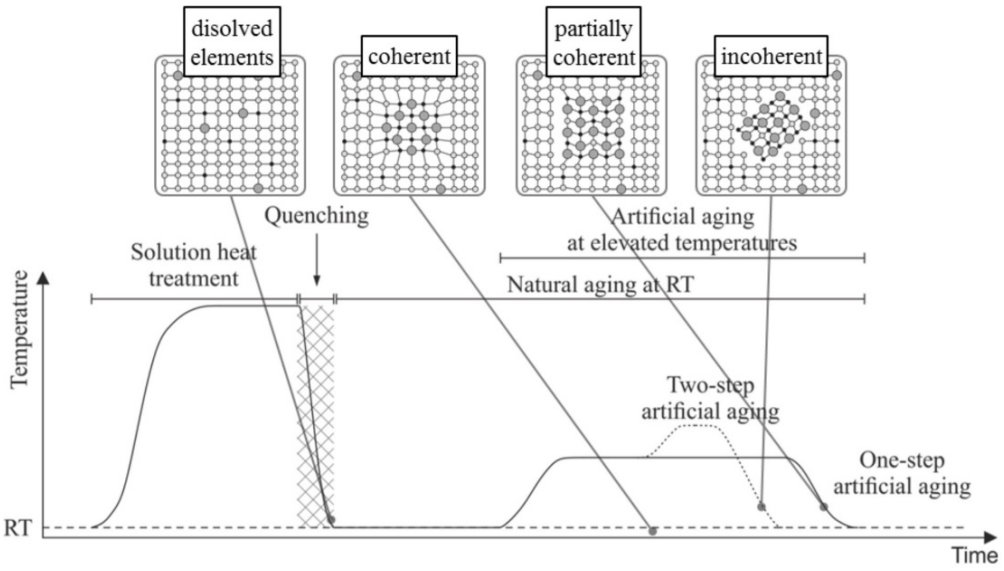

Figure 2.8 The heat treatment profile of 7xxx aluminium alloys (Ostermann, 1998, Behrens et al., 2017).

2.3.1 Process of precipitation hardening

In SHT, the aluminium alloy is heated above the solvus temperature, which is alloy specific, at a rate of 1 °C/s and is allowed to soak (specific time depends on size) to allow the whole sample to reach the solvus temperature. This process enables the dissolving of all phases into one homogenous solid solution, which is the α-phase shown in Figure 2.9. In addition, the SHT temperature for AA6082 should be limited to a range between 500 and 585 °C (Li et al., 2015).

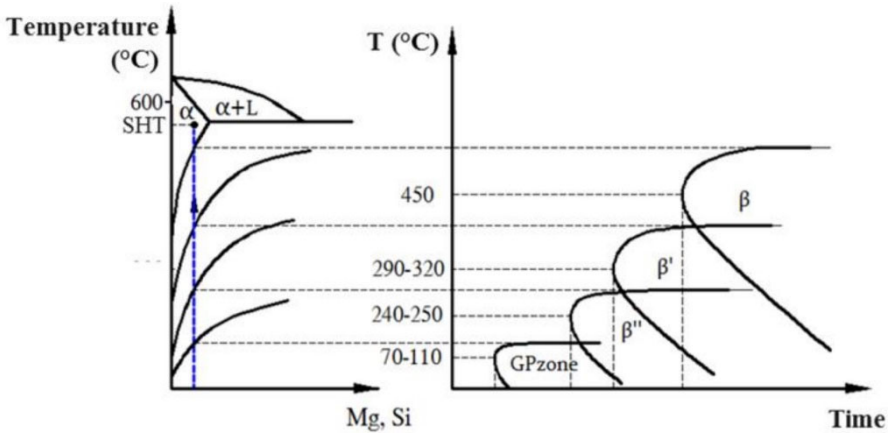

Figure 2.9 Schematic phase diagram and time temperature transformation of precipitates in AA6082 (Li et al., 2015).

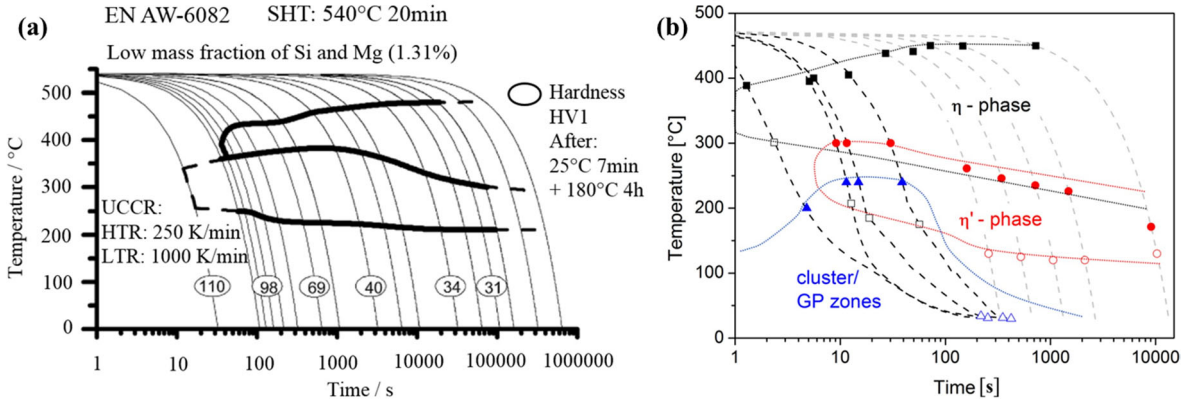

Figure 2.10 The continuous cooling precipitation diagram of a) AA6082 (Milkereit et al., 2012) and b) AA7449 (Schloth, 2015).

Rapid quenching immediately follows the SHT to create a SSSS within the material matrix. Quenching rate is the most important factor in the precipitation hardening process, with regards to the ageing process. A quench rate at or exceeding the critical quenching rate would enable SSSS of the material. In Figure 2.10, the continuous cooling precipitation (CCP) diagram illustrates the slowest cooling rate that needs to be achieved in order to prevent the precipitation of unwanted secondary phases and precipitates during cooling (Milkereit et al., 2012, Schloth, 2015). By comparing both CCP diagrams, it was found that the ultra-high strength AA7xxx required a much faster critical cooling rate than high strength AA6xxx. It is clear that the cooling from SHT temperature to Room Temperature (RT) is less than one second, while only requiring cooling within 30 seconds to prevent precipitation. Therefore, AA7xxx is more time sensitive than AA6xxx and prevention of precipitation during cooling is essential to achieve an optimal age-hardening process.

AA6xxx: SSSS → Co-clusters → GP-I zone → GP-II zone (β'') → β' → $\beta(Mg_2Si)$

AA7xxx: SSSS → Co-clusters → GP zone → η' → $\eta(MgZn_2)$

Figure 2.11 The sequence of the precipitation sequence of AA6xxx and AA7xxx.

Figure 2.11 illustrates the precipitation sequence of Al-Mg-Si and Al-Mg-Zn alloys (Lloyd and Chaturvedi, 1982, Greiser et al., 1999, Berg et al., 2001, Chrominski and Lewandowska, 2016). The complex process normally involves multiple stages: starting with the formation of solute clusters, then metastable Guinier-Preston (GP) zones and reaches the final equilibrium phase via the formation of multiple intermediately precipitates. In the case of AA6XXX al-alloy, Co-clusters are formed by Mg and Si in the aluminium matrix with un-defined structure. When co-clusters grow further, GP zones will emerge with a spherical structure within the aluminium matrix. β'' phase, with the composition of MgSi, has been proved as the peak aged condition for the highest post strength of the material. This is because the size of β'' is large enough to provide high strength resistance for dislocations to cut, and appropriately small to avoid bowing. However, ageing for a long time will pass the material through the $\beta'' \rightarrow \beta' \rightarrow \beta$ phases, which causes over-ageing and thus a reduction in strength. In addition, the time for conventional ageing takes approximately 8-10 hours for AA6xxx (Greiser et al., 1999, Chrominski and Lewandowska, 2016).

For a 7xxx series al-alloy, the ageing process could take up to 48 hours (Lloyd and Chaturvedi, 1982, Berg et al., 2001). The Co-clusters are formed by Mg and Zn in the aluminium matrix. Precipitation often begins with the formation of GP zones, and two types of GP zones can usually co-exist in the matrix called GPI zones and GPII zones. During ageing, GP Zones transform into metastable hexagonal phase η' precipitates with longer ageing time at an ageing temperature above 100 °C but below 190°C, hence the equilibrium precipitate η will be formed (Berg et al., 2001, Liu et al., 2015a). On the other hand, ageing temperature plays an important role in the precipitation hardening, as the GP zone will dissolve again instead of converting to η' when the temperature is above 190 °C. Nevertheless, the η phase is the stable equilibrium phase at room temperature, but it has lower strength compared with the material at the phase of η' as over-ageing begins to occur (Li et al., 1999, Berg et al., 2001, Liu et al., 2015a).

2.4 Interfacial heat transfer coefficient

In non-isothermal warm and hot stamping processes, a hot blank is deformed by cold forming tools, and thus heat transfer occurs. The interfacial heat transfer coefficient (IHTC) is, therefore, an essential boundary condition in such forming technologies for obtaining precise temperature fields from the formed components in finite element (FE) simulations, as described by (Karbasian and Tekkaya, 2010).

2.4.1 Effect of contact pressure and tool coating on the IHTC

By using a precise definition of the IHTC by Liu et al (2017b; 2017c), the processing window and tool design were subsequently optimised to attain the critical cooling rate. Hence, the IHTC has been characterised in previous research to study its influential factors. Different trends of the IHTC were found as the contact pressure was increased, for example, Figure 2.12 illustrates an exponential trend as determined by Liu et al (2018b), a power law trend as shown by Chang et al (2016) and a linear trend shown by Caron et al (2014), due to a larger real contact area and thus heat transfer occurring at higher contact pressures. Additionally, the IHTC decreased with the application of low thermal-conductive tool coatings, such as glass-based coatings in the study of Bai et al (2012). However, this value was increased by the application of high thermal-conductivity tool coatings, such as silver-based coatings investigated in the work of Li et al (2000).

In the previous studies, the IHTC values were determined at specific initial blank temperatures. However different stamping processes utilise different initial blank temperatures, or forming temperatures, that depend on the component being formed and the desired post-form properties. In order to predict the IHTC evolutions as a function of contact pressure and tool coating, Liu et al (2019b) developed a mechanism-based model, which was then implemented in the Knowledge Based Cloud-Finite Element (KBC-FE) simulation technique developed by Wang et al (2019), enabling the multi-objective simulation of non-isothermal forming thus saving on the development of user-defined subroutines in conjunction with FE software. The temperature-dependent IHTC could be implemented in the KBC-FE to improve the multi-objective simulations, which were subsequently validated by using the experimental results of warm and hot stamping tests under different temperature conditions.

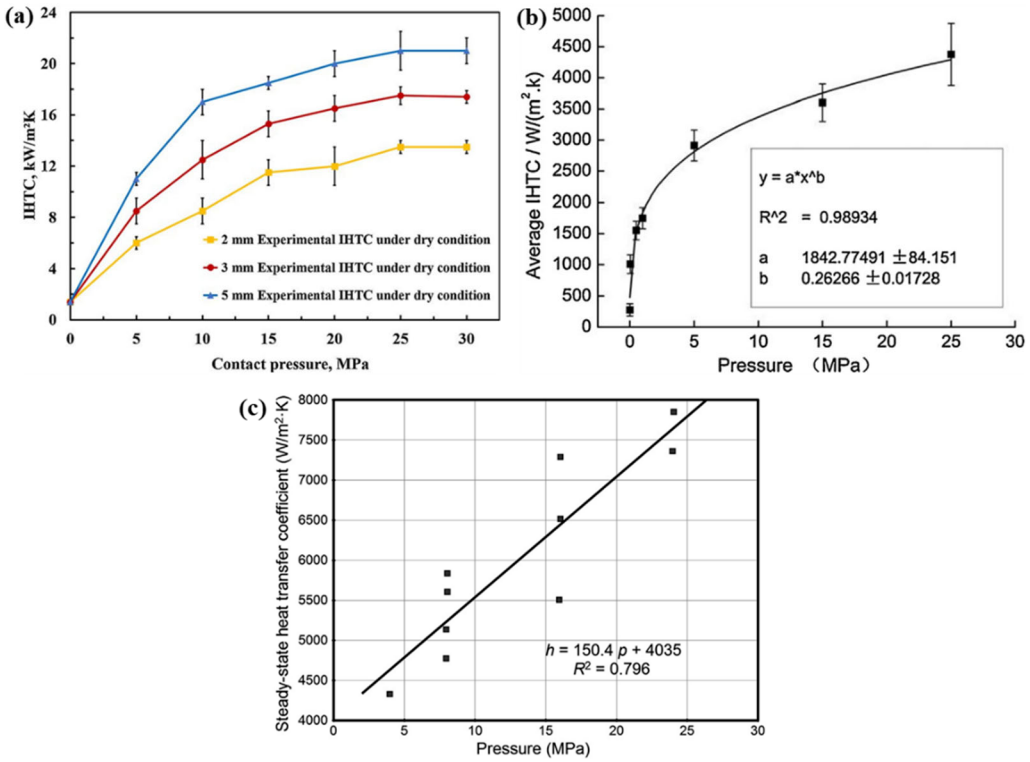

Figure 2.12 Relationship between the IHTC and contact pressure (a) exponential trend (Liu et al., 2018b), (b) power law trend (Chang et al., 2016) and (c) linear trend (Caron et al., 2014).

2.4.2 Implementation in finite element simulation

Finite element analysis (FEA) software is capable of providing solutions for metal forming processes and optimising the process window without considerable physical efforts (Tekkaya, 2000, Karbasian and Tekkaya, 2010, Merklein et al., 2016). FE simulation of hot stamping processes featuring the complex nature of thermal and mechanical fields requires the implementation of accurate material properties and boundary conditions, such as the flow stress dependent on the temperature and strain rate (Garrett et al., 2005), the interfacial heat transfer coefficient (Liu et al., 2018b) and friction coefficient (Hu et al., 2019) dependent on the temperature, contact pressure, tool material, lubricant and coating. Subsequently, the simulated results, including stress, strain and thinning, are used to preliminarily evaluate the quality of the formed components. However, under the complex hot stamping conditions, the failure prediction of the formed components could not be simply determined by the strain and thinning but evaluated by the forming limit as a comprehensive result of temperature, strain rate and loading path (Gao et al., 2017). In addition, the critical quenching rate has to be met to avoid the intersection between the temperature evolutions and CCP diagram of the material, in order to achieve the desired microstructure and post-form strength (Liu et al., 2017a, Zhang et al.,

2019). Those advanced evaluation criteria of the formed components essential to the hot stamping processes could be computed by post-processing the simulated results in the FE software or user-defined subroutines (Lin and Dean, 2005, Abedrabbo et al., 2006b, Li et al., 2019). Therefore, the implementation of accurate material properties and boundary conditions as well as the computation of the advanced evaluation criterion are critical to the FEA of hot stamping processes (Zhou et al., 2016, Wang et al., 2019).

AutoForm and Pam-Stamp Forming are two typical FE software packages in the market that offer comprehensive features for modelling sheet metal behaviour during metal forming processes. Its powerful, efficient solver and user-friendly interface have made AutoForm and Pam-Stamp Forming the most widely used FE software in the sheet metal forming industry. Both software packages provide functionalities to simulate heating, forming and quenching processes, from which the temperature field, thinning distribution, and quenching rate of the formed component could be obtained. Although these are important properties required for evaluating the quality of formed components, the assessment remains incomplete without the ability to obtain more advanced, reliable results through multi-objective simulation of the process (Wang et al., 2019). The prediction of formability, quenching efficiency and post-form strength are critical properties that affect the quality of the formed components. However, these properties cannot be directly acquired using the functions provided by typical FE software packages. Although time-consuming subroutines are widely used to acquire these results, they may not be applicable for all FE software packages. Moreover, the development of such subroutines often requires multi-disciplinary expertise and requires specific knowledge to tailor them to the software being used (Zhou et al., 2016). Therefore, a multi-objective FE simulation framework for hot stamping of aluminium alloys is in critical demand. In addition, the accuracy of FE simulation results is dependent on the thermomechanical boundary conditions under process-relevant conditions. These include the flow stress (El Fakir et al., 2014), coefficient of friction (Hu et al., 2017) and IHTC (Liu et al., 2017c), which govern material behaviour and couple the mechanical and thermal fields. Such thermomechanical boundary conditions should be determined under process-specific conditions to allow outputs of the FE simulation to be accurately evaluated.

2.5 Summary

In this chapter, conventional forming technologies for producing high/ultra-high strength aluminium alloys components and the related studies on mechanical properties and precipitates hardening process have been reviewed. It was found that the use of TWBs would further reduce the overall mass and improve the structural stiffness. Warm and hot stamping processes can increase the formability and reduce springback of complex shaped parts made from AA6xxx and AA7xxx. The improvement of post-form strength was contributed by applying longer soaking time at SHT temperature, fast heating rate, shorter transfer time and fast quenching rate. Springback decreased with increasing forming temperature and fast forming speed. However, it is still challenging to further improve the production rate and achieve further cost savings in the warm and hot stamping processes, due to the lengthy heat treatment and artificial ageing times. In order to overcome this problem, a novel sheet metal forming process called 'Fast light Alloys Stamping Technology (FAST)' was developed and primarily studied for AA6082, AA7075 and DA-TWBs. In addition, contact pressure and tool coating effect on IHTC were reviewed which shows the positive relationship between contact pressure and IHTC value, and an inverse relationship with the application.

Chapter 3. Materials and experimental procedures

This chapter is divided into four sections and outlines the experimental tests that were conducted on the sheet aluminium alloys AA6082 and AA7075. Firstly, the detailed chemical composition and mechanical properties of each as received material is clearly stated. Secondly, the concept of the FAST process for DA-TWBs is demonstrated in three main stages including material pre-treatment, FAST forming process and OEM paint bake cycle. Thirdly, the thermo-mechanical properties of AA6082 and AA7075 performed through uniaxial tensile tests and strength degradation tests are presented. The uniaxial tensile tests were conducted to evaluate the ductility of testing materials under various temperatures and strain rates. The strength degradation tests were conducted to characterise the post-PBC strength of the AA6082 and AA7075 under the FAST conditions by comparing the residual hardness (post-PBC hardness) of heated specimens under various forming conditions, such as material pre-treatment temperatures and time, heating rates, forming temperatures, soaking periods and quenching sources. Finally, a forming toolset was designed, fabricated and assembled on a novel lab-scale production line called Uni-form, which enabled FAST forming tests on the AA6082, AA7075 and DA-TWBs to be realised and verified. Springback of the AA6082 and AA7075 was evaluated after bending at various temperatures and forming speeds. Post-PBC strength of formed parts at different locations was characterised through uniaxial tensile tests at room temperature. The structure of this chapter is shown in Figure 3.1.

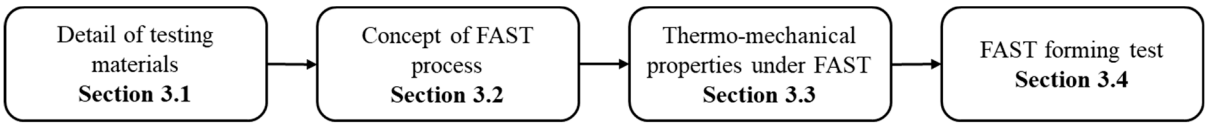

Figure 3.1 The schematic diagram for the major sections covered in Chapter 3.

Two developed test facilities in Chapter 3 lead to two patents:

" Cai, Z., Liu, X., Dhawan, S., Fakir, O. El., Lin, J., Wang, L., 2019. A compact automatic simulating facility for non-isothermal forming processes. Patent application number: CN201911035650.9"

"Luan, X., Cai, Z., Sun, Y., Zhang, Q., Fakir, O. EL., Wu, G., Lin, J., Wang, L., 2019. A device for simulating the hot stamping process of a sheet. Patent application number: CN201910707785.9."

3.1 Testing material

The testing materials used for all the tests were commercial sheet aluminium alloys AA6082 and AA7075 which were provided by the material supplier Smiths Metal Centres Ltd. The as-received materials were both rolled sheet with a thickness of 2 mm and chemical composition (wt. %) is shown in Table 3.1.

Table 3.1 Chemical compositions of the aluminium alloys in weight proportion (wt. %) (Klampfer, 2017).

Composition	Si	Fe	Cu	Mn	Mg	Cr	Zn	Ti	Al
AA6082	0.9	0.38	0.08	0.42	0.7	0.02	0.05	0.03	97.42
AA7075	0.4	0.5	1.5	0.3	2.5	0.22	5.6	0.2	88.78

In order to evaluate the mechanical properties for both materials at as-received conditions, the international standard ASTM E8 (Instron, 2020a) was applied to uniaxial tensile tests on an 50 kN Instron machine at a strain rate of 0.001 /s, and the dog-bone shaped tensile samples with the suggested standard dimensions were waterjet cut from as-received sheet material. The initial thickness of both test materials was 2 mm. The hardness of as-received aluminium alloy sheets was tested using a Vickers indenter with a force of 50 N (HV5). As shown in Table 3.2, the testing material AA6082 has a yield strength of approximately 300 MPa while AA7075 has a much greater value of approximately 500 MPa, and around 10 % elongation at fracture for both materials at room temperature. The mean hardness values obtained for the as-received materials were approximately 120 HV for AA6082 and 180 HV for AA7075. In addition, the standard mechanical properties of commercial materials were also included in Table 3.2 for comparison.

Table 3.2 Mechanical properties of as-received aluminium alloys (Make it from, 2020).

Mechanical Properties	Tensile Strength (MPa)		Yield Strength (MPa)		Young's Modulus (GPa)		Elongation at Fracture (%)		Vicker's Hardness (HV_5)	
	Test	Standard	T	S	T	S	T	S	T	S
AA6082-T6	334	330	295.9	270	72.3	69	10	9.8	120	104
AA7075-T6	538	560	491.1	480	77.4	70	11	7.9	180	165

3.2 The concept of the FAST process of the DA-TWBs

A novel Fast light Alloys Stamping Technology (FAST) was developed to enable the mass production of complex-shaped high strength aluminium panel components. The proposed method was expected to use ultra-fast heating of an aluminium alloy sheet to an appropriate temperature, which reduces the total forming cycle time to under 8 seconds whilst reducing energy consumption. In addition to the benefit of using FAST process, it has been found that a similar strength of as-received material can be retained in the formed components, and the springback effect is also reduced or eliminated depending on the complexity of the component. The feasibility of the FAST was initially studied on the AA6082 and AA7075 respectively, then applied to the application of DA-TWBs by using the common processing window that was suitable for both the AA6082 and AA7075 alloys. The detailed results and discussion of the implementation of FAST in AA6082, AA7075 and DA-TWBs are presented in Chapter 4.

The working principle and corresponding temperature evolution during the FAST process of the DA-TWBs are illustrated in Figure 3.2.

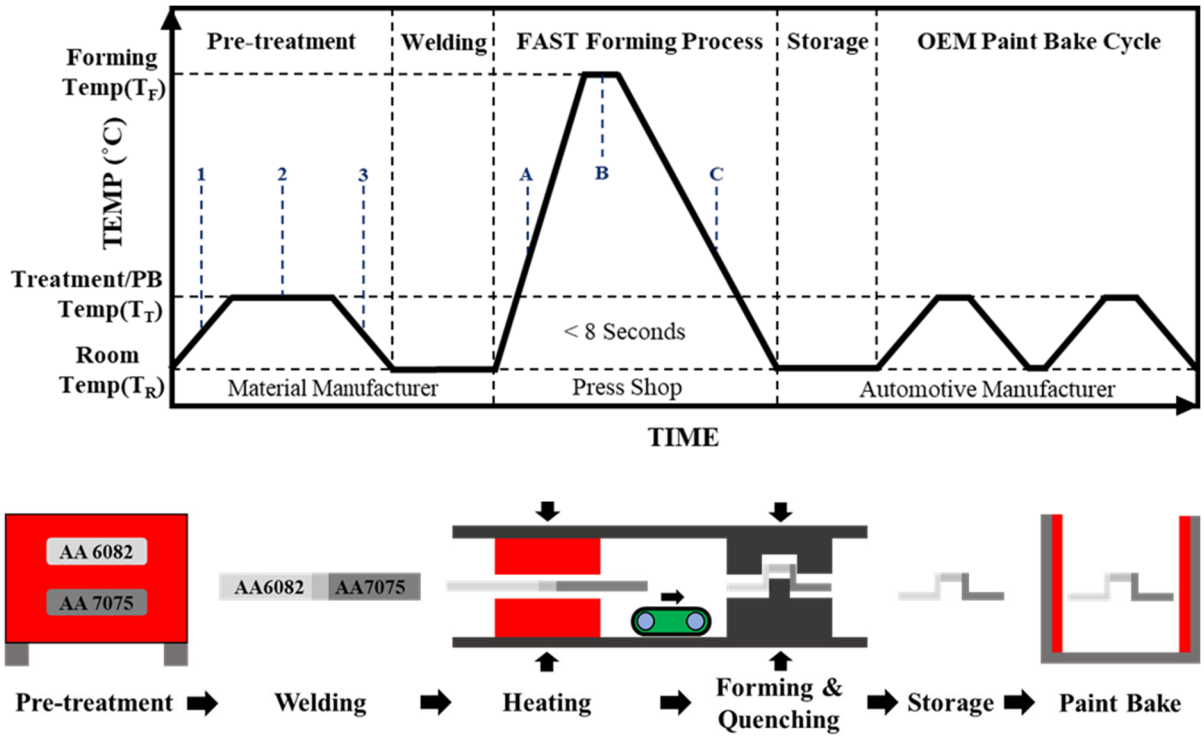

Figure 3.2 Thermal profile and schematic diagram of FAST processes to form the DA-TWBs.

The proposed method contains three main stages including material pre-treatment, FAST forming process and OEM paint bake cycle. Two individual base materials have been pre-

treated in a furnace at a specific treatment temperature for a specific time, then friction stir welded together to become DA-TWBs. During the non-isothermal fast forming process, a powerful contact heating facility was integrated between the forming tool, which provides a rapid heating rate and hence shortens the heating time. The cold forming tool closes immediately at a rapid speed by applying a specific die closing pressure to form and quench the aluminium alloy sheet to room temperature. The detailed process of FAST forming of DA-TWBs comprised the following steps:

- The first step is pre-treatment of two base materials individually:
    1. Placing the material into the furnace and heating the sheet metal to a specific treatment temperature;
    2. Soaking at the treatment temperature for a specific period;
    3. Removing the sheet metal from the furnace and cooling naturally to room temperature.
- The second step involves welding the two base materials together to produce DA-TWBs by friction stir welding.
- The third step is to form the DA-TWBs into desired shapes by the procedure:
    A. Heating: heat the DA-TWBs at a critical fast heating rate to reach the critical forming temperature. Both optimal values were determined by comparing the post-PBC strength properties and springback effect with various heating rates and forming temperatures.
    B. Transfer: transfer the heated blank from heating station to forming station within a short period via a precisely controlled automated conveyor system.
    C. Forming and quenching: the DA-TWBs are immediately formed into the desired shape at the appropriate forming temperature within a set of cold dies and cooled at a critical quenching rate, under a critical die closing pressure determined via testing.
- The fourth step is storage and transportation of the formed component from the press shop to the car assembly line. The material is able to be stored at room temperature without unfavourable natural ageing effects on the strength recovery.
- The fifth step is to convert the traditional OEM paint bake cycle into a form of post-artificial ageing process to restore the post form strength. In this research, the paint bake cycle was

provided by one of the project sponsors and fixed as dual cycles with 20 minutes baking at 180 °C for each cycle.

In order to further improve the efficiency of product development and production rate, the stages of material pre-treatment and welding could be completed by the material manufacturer or supplier, and the OEM paint bake cycle could be completed on-site with the automotive manufacturer.

3.3 Thermo-mechanical properties investigation under the FAST process

3.3.1 Uniaxial tensile tests

Uniaxial tensile tests were conducted to determine the thermo-mechanical properties of two base materials AA6082 and AA7075 at FAST conditions using a Gleeble 3800 thermo-mechanical simulation and testing system. The test machine was capable of heating specimens at a rate of more than 10000 °C/s by using direct resistance heating. Quenching with the test specimen can be achieved by either air quenching tubes or water cooling channels, which allows the control of the cooling rate during the test. The mechanical system is capable of up to 10 tonnes of tension load and 20 tonnes of compression load. In addition, the testing system allows for pre-programming of the thermal and mechanical history before the test, which provides precise control of the experimental process.

3.3.1.1 Specimen design and preparation

Axisymmetric dog-bone shaped specimens were manufactured from the rolled sheet alloy by laser cutter, along the longitudinal direction which parallels to the rolling direction of the sheet blank. As shown in Figure 3.3 (a), the design of the specimen indicated that the width and parallel length of the gauge section was 12 mm and 50 mm, respectively. The specimen was then fixed within low thermal conductivity stainless steel grips, clamped between jaws with one set of position pins to ensure the test sample was correctly placed. The C-Gauge transducer was positioned in the mid-point of the specimen during the test, which enables the real-time recoding of width change during testing. A pair of K-type thermocouples were spot-welded (spot welding voltage 30 V) to the centre of each specimen to provide accurate feedback control of the temperature to the system. In order to determine the effective gauge length for the

designed specimen, the temperature distribution along the test sample was investigated during the first test with four sets of thermocouples. The distribution of each pair of thermocouples is shown in Figure 3.3(b), where TC1 is the thermocouple welded at the mid-length of the specimen, and TC2, TC3 and TC4 are located at 5 mm, 10 mm and 15mm from the centre position respectively.

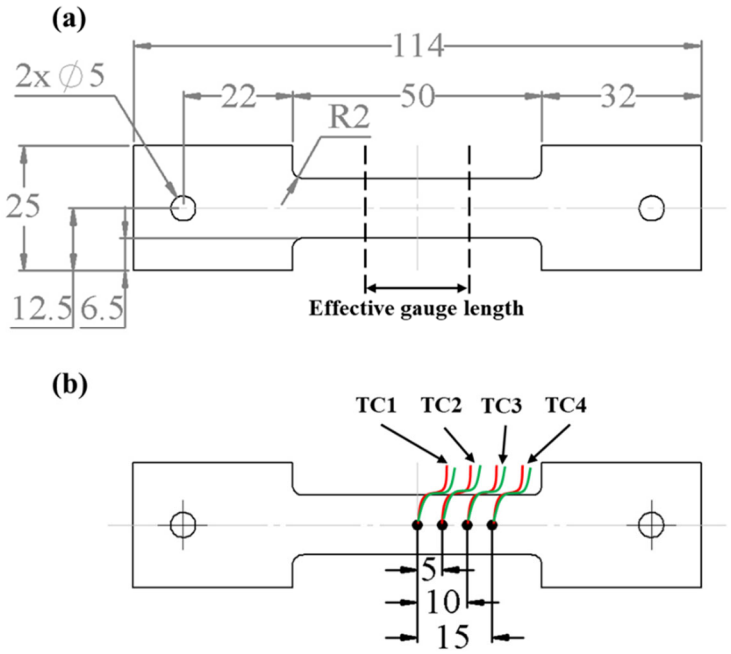

Figure 3.3 Dog-bone shaped specimen design (dimensions are in mm) with effective gauge length and different thermocouple locations (a) specimen design and (b) the location of 4 pairs of thermocouples attached.

To prepare the specimen for each test, the first step was to polish the surface and edges of the specimen with fine sand paper, which provides a clean surface for welding the wires of the thermocouples, and avoids any sharp edges causing stress and heat concentrations during the test. Secondly, the sample width and thickness were measured and recorded at three different locations along the effective gauge area. Thirdly, the pairs of the thermocouple were spot-welded on the sample. Finally, the sample was placed with a set of jaws and clamped into the testing system, and operated with a pre-set test program.

3.3.1.2 Experimental set up and test programme

Figure 3.4 shows the uniaxial tensile test set up on a Gleeble thermo-mechanical testing machine consisting of a controller with a digital screen to show the real-time data during the test. A support unit provides heating and cooling through the testing chamber. Inside the testing

chamber, the specimen was clamped, and C-Gauge was attached to the middle of the specimen and connected to the system for real-time data transfer. A powerful resistance heating system provides a fast heating rate up to 50 °C/s, and the pair of thermocouples welded to the middle of the test sample were attached to the system, thus providing precise control of the testing temperature. During the deformation process, the actuator pulled at one end of the specimen until fracture occurred.

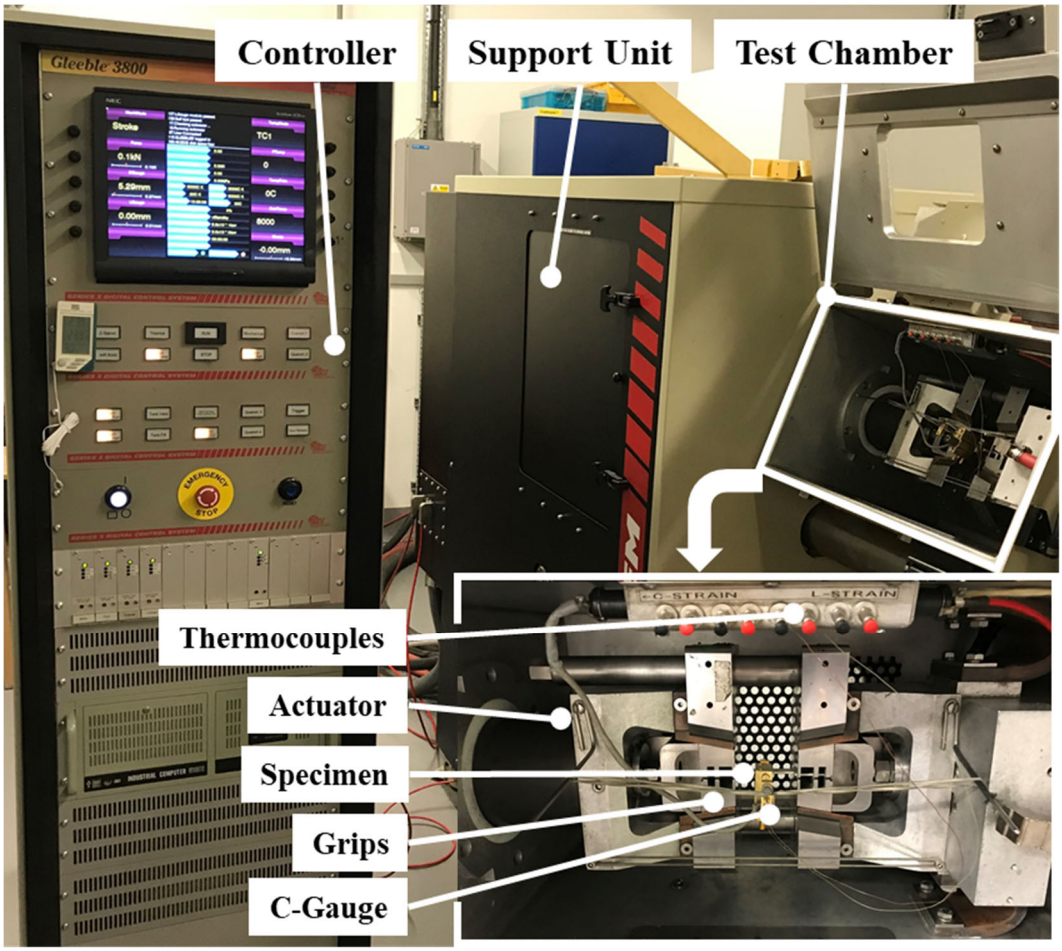

Figure 3.4 Uniaxial tensile test set up on the Gleeble 3800 simulator.

The thermo-mechanical properties of the AA6082 and AA7075 with the effect of temperature and strain rates were evaluated in the experimental program which is shown in Figure 3.5. Specimens were first heated to a temperature 25 °C lower than the target temperature at a fast heating rate of 50 °C/s and then slowly heated to the target temperature at a rate of 5 °C/s. The purpose of such a heating profile was to avoid temperature overshoot, and also ensure no fluctuation or overheating would occur. Once the specimen reached the target temperature, the force-controlled system set the force to zero which enabled the actuator to automatically compensate for thermal expansion, as the specimen will expand with increasing temperature.

Subsequently, the Gleeble system was set to stroke control, enabling accurate control of the displacement of the grips and thus the strain rate. During the tensile test, the specimen temperature was maintained at the target temperature, and naturally cooled to room temperature once fracture occurred.

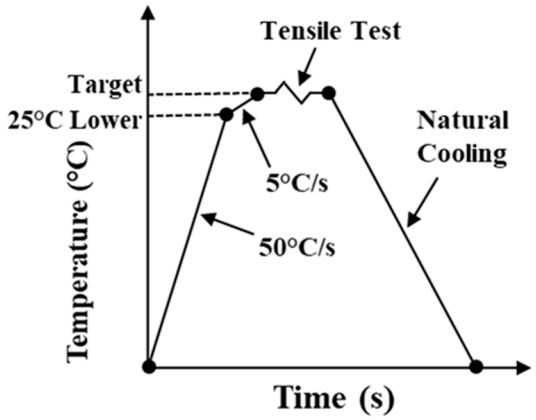

Figure 3.5 Schematic diagram for the uniaxial tensile test.

The detailed test matrix for the uniaxial tensile tests is shown in Table 3.3, for the AA6082 and AA7075 both at T4 temper (Solution heat treated and natural aged). The testing temperature ranged between 300 °C and the solution heat treatment temperature (535 °C for AA6082 and 490 °C for AA7075). The solution heat treatment temperature was provided by the material supplier which was specific for each type of material. The temperature effect on the viscoelastic response was studied by using a constant strain rate of 1 s^{-1}, which is the strain rate most commonly used for the high-speed forming process. The effect of strain rate was investigated at 535 °C and 425 °C for AA6082 and AA7075, respectively, which are common temperatures for stamping 6xxx and 7xxx aluminium alloys.

Table 3.3 Uniaxial tensile test matrixes ('√' represents the selected test conditions).

Materials	Temperature (°C) / Strain rate (s^{-1})	300	350	400	425	450	490	500	535
AA6082	0.1								√
	1	√	√	√		√		√	√
	3								√
	5								√
AA7075	0.1				√				
	1	√	√	√	√	√	√		
	3				√				
	5				√				

3.3.1.3 True stress and true strain data processing

The stress-strain curves of each testing condition were obtained by post-processing of the Gleeble data. The tensile force was measured using a load cell which was fixed to the machine. The total force over the area (measured before and after the test) of the specimen with the effective gauge length was used to determine the relative stress. Strain can be calculated by defining the effective gauge length which ends at the position where a 5 °C difference is obtained from the centre testing point. Therefore, the engineering stress-strain curves were obtained by combining the strain and stress results, and the true stress and strain can be converted by using the following equations:

$$Engineering\ strain, e = \frac{(L - L_0)}{L_0} \tag{3.1}$$

$$True\ strain, \varepsilon = \ln(1 + e) \tag{3.2}$$

$$Engineering\ stress, \delta = \frac{F}{A} \tag{3.3}$$

$$True\ stress, \sigma = \delta(1 + e) \tag{3.4}$$

3.3.2 Strength degradation tests

In the strength degradation tests, the effect of pre-treatment time, heating rate, forming temperature, soaking time and quenching rate for the FAST process were investigated, and the post-PBC hardness of the specimen was compared before and after each test to evaluate the change on post-PBC strength. Four test machines were used in this test, namely the thermo-mechanical simulator Gleeble 3800, Zwick hardness indicator, Lenton furnace and Instron environmental chamber.

3.3.2.1 Specimen design and experimental set up

Axisymmetric rectangular specimens with a thickness of 2 mm were manufactured from the rolled sheet alloys by laser cutter, along the longitudinal direction which parallels to the rolling direction of the sheet blank. Figure 3.6 (a) shows the specimen design and the location of the welded thermocouples. The width and length of the specimen was designed to be 10 mm and 106 mm, respectively. The pair of thermocouples were welded on the surface which was located at the centre of the test sample. Figure 3.6 (b) indicates the locations where the hardness was measured on the side of the sample, and at least 5 measurements around the centre point were taken.

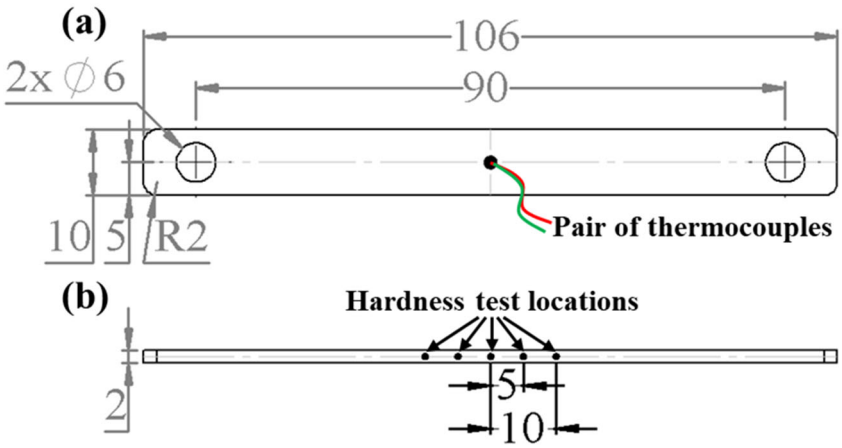

Figure 3.6 Strength evaluation test (a) specimen design (dimensions are in mm) with thermocouples attached at the top view and (b) locations for hardness test at the side view.

Before each test, it is necessary for the test material to be at “the softest” (supersaturated solid solution state) condition where the highest ductility of material flow occurred. The as-quenched condition was obtained by solution heat treatment in a furnace. During the solution heat treatment, the Lenton furnace shown in Figure 3.7 (a) with temperature capability ranging from

0 to 900 °C was set to the required solution heat temperature with two identical steel blocks (250×80×15 mm^3) placed inside. A pair of K-type thermocouples with one end fixed to the specimen was held between the steel blocks in order to monitor the temperature with a digital thermometer. It was required to hold for a certain period (dependent on the target temperature) until the temperature shown in the thermometer reached the target temperature and remained stable. The specimens were placed uniformly between the steel blocks during the heat treatments (sandwich structure), which ensures both sides of the specimen were in good contact with the heated blocks. As the specific heat capacity of steel is larger than air, the usage of blocks acts as a thermal reservoir and minimises severe temperature fluctuations caused by the airflow when opening and closing the furnace doors.

The SHT temperatures for AA6082 and AA7075 were 535 °C and 490 °C, respectively, and the soaking time was 30 minutes for both materials. Once SHT was completed, the fast quenching of the specimen to obtain the supersaturated solid solution state was achieved by quickly removing all the specimens from the furnace and dropping into the water tank.

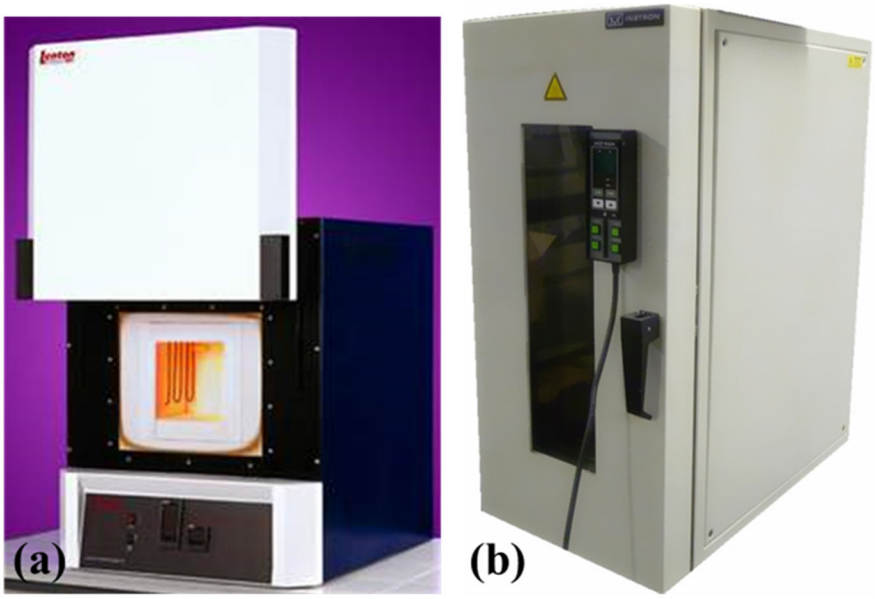

Figure 3.7 Facilities used in the material pre-treatment test (a) Lenton furnace (Lenton, 2020) and (b) Instron environmental chamber (Instron, 2020b).

After the water quench, in order to avoid the natural ageing effect at room temperature, all the specimens were immediately placed into the environmental chamber for pre-treatment. As shown in Figure 3.7 (b), an Instron environmental chamber with temperature range capability between 0 and 250 °C were used for pre-treatment (pre-ageing) on the specimens. A similar

experimental setup including the two metal blocks and a pair of K-type thermocouples were used to maintain and monitor the temperature, respectively.

The Gleeble 3800 thermo-mechanical simulator shown in Figure 3.8, was used to investigate the effect of heating rate, soaking time, forming temperature and quenching rate on the post-PBC hardness of the AA6082 and AA7075 specimens under the FAST test condition. The rectangular specimen was clamped between the stainless steel grips, and two quenching channels were adopted to perform water quenching for both sides of the specimen. Stroke control was not used as there was no deformation required on the specimen during the strength degradation test. However, the thermal and force control was programmed with respect to time for the precise control of the test conditions. Moreover, the force was set to zero immediately after the heating process was completed, to compensate for the thermal expansion of the specimen.

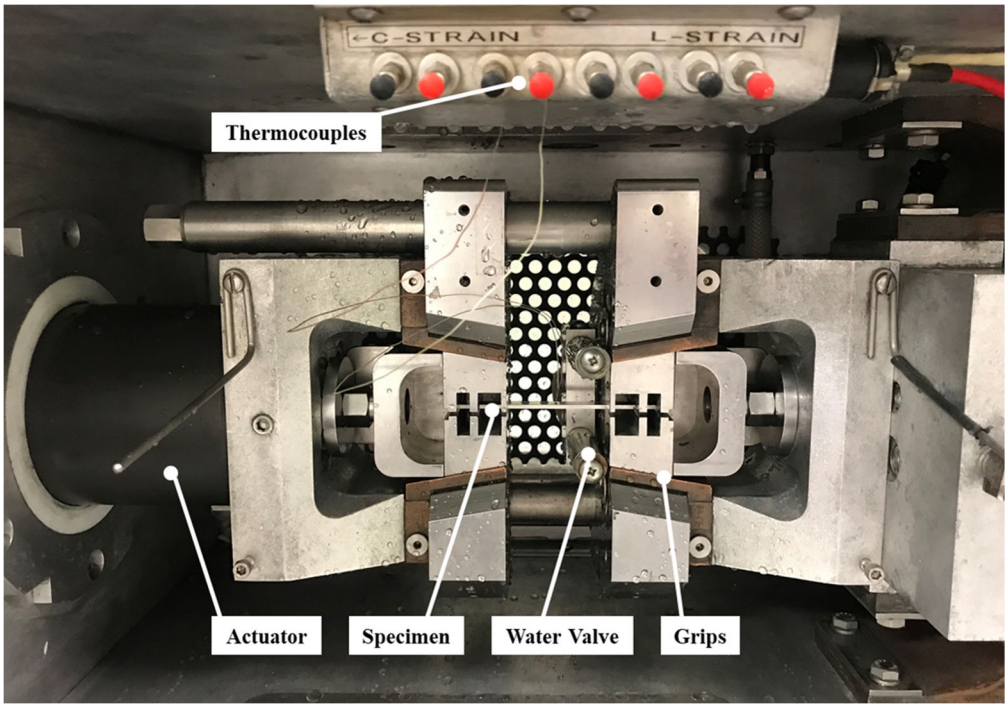

Figure 3.8 Strength evaluation test set up on Gleeble 3800 simulator.

In the present work, hardness was used to indicate the strength of all specimens. Vickers microhardness measurements were taken by using a Zwick hardness indenter on the surface of well-polished samples before and after each test condition, in order to determine the specimen performance. The, test samples were polished with sandpaper (grade 400) discs which were attached on the Labopol-25 grinding machine as shown in Figure 3.9, to remove any sharp edges that cause heat concentration during testing and also to provide good surface quality for

subsequent hardness tests. The Zwick hardness tester is shown in Figure 3.10, where all the hardness measurements were made by using a 50 N (HV5) load and 10 seconds dwell time at room temperature, and a total of 5 tests were performed for each specimen to obtain the mean hardness value.

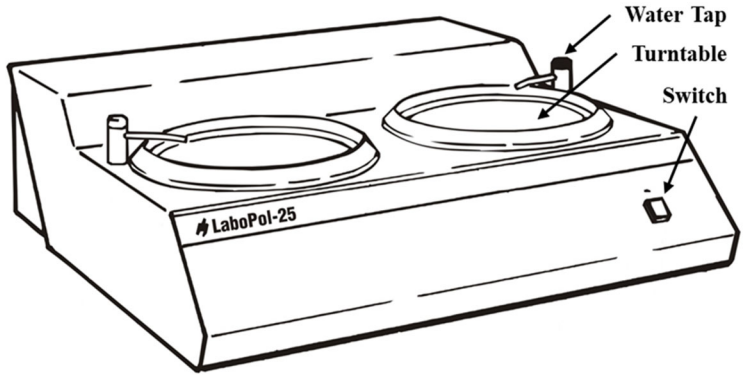

Figure 3.9 Labopol-25 grinding machine for polishing the test specimen (Struers, 2020).

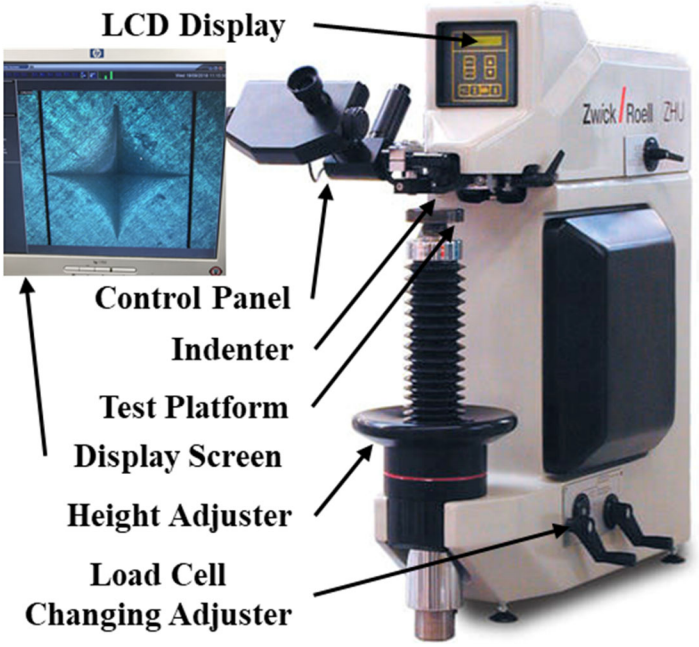

Figure 3.10 Hardness tester Zwick Roell ZHU (Zwick/Roell, 2020).

3.3.2.2 Experimental programme

The detailed test plan and parameters are shown in Figure 3.11, where a total of 5 variables were investigated, in order to evaluate the optimal forming condition for the FAST forming of AA6082 and AA7075 materials. In case (a), the effect of pre-treatment was evaluated by placing the specimen in the environmental chamber with various time periods ranging from 0 to 150 minutes, at a constant pre-treatment temperature of 180 °C and 120 °C for AA6082 and

AA7075 respectively. In case (b), different heating rates ranging from 1 to 200 °C/s were applied to investigate the heating rate effect on post-PBC hardness, where the target temperature for both materials was set to 300 °C in order to maintain consistency between tests. In case (c), the effect of soaking time on post-PBC hardness was carried out by heating the specimens to 300 °C with a fast-heating rate of 50 °C/s followed by soaking for a period of time between 0 and 8 seconds. In case (d), different target (forming) temperatures varying from room temperature to material SHT temperature were applied to investigate the temperature effect on post-PBC hardness, at a fast heating rate of 50 °C/s and zero soaking time. In case (e), the specimens were heated at a rapid heating rate of 50 °C/s to 300 °C and subsequently quenched to the room temperature by cool die and water, respectively. The cooling rate of the cool die and water was approximately 150 and 400 °C/s. A dedicated test rig IHTC-mate was utilised to conduct the die quenching tests, with the equipment design and test setup presented in Chapter 4.

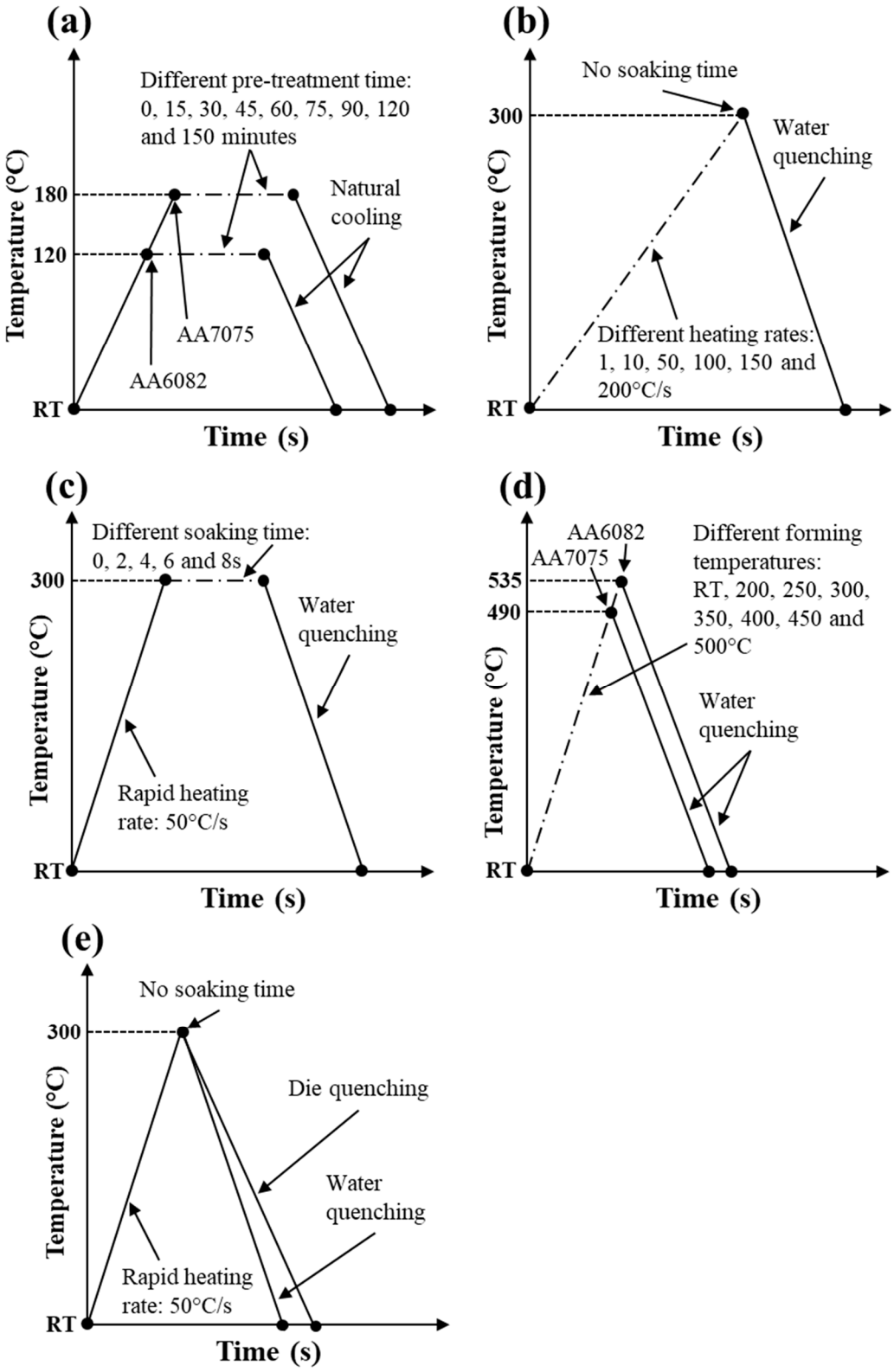

Figure 3.11 Strength evaluation test program for conditions at different (a) pre-treatment time (b) heating rates (c) soaking time (d) forming temperatures and (e) quenching sources.

3.4 FAST forming tests

In order to validate the feasibility of the proposed FAST process for the AA6082, AA7075 and DA-TWBs, a dedicated lab-scale pilot production line namely "*Uni-Form*" was designed and patented by the author's research group (Luan et al., 2019), which enabled the optimal processing parameters obtained from the Gleeble system to be realised and verified in lab-scale. U-shaped components were formed under the FAST process with the selected testing materials via the *Uni-Form* pilot production line.

3.4.1 Experimental set up and forming tool design

The FAST process involving pre-treatment, ultra-fast heating, hot or warm stamping and rapid quenching can be simulated through the *Uni-Form* testing facility. The overall design of *Uni-Form* is shown in Figure 3.12, and consists of four basic subsystems which include furnace, forming tool, incubation chamber and conveyor. Each subsystem can be removed and replaced with other designed modules according to the component shapes and requirements of the forming process. A furnace was assembled near the support frame and forming toolsets which enabled the rapid transfer between the heating station and forming station, in order to prevent heat loss during an extended transfer period. The furnace consists of two powerful contact heating plates, which can provide a maximum heating rate up to 200 °C/s and maximum forming temperature of 650 °C. During the forming tests, two hot tubular air platen heaters in the heating system were pressed to heat the cold blank on both sides (top and bottom), then quickly transferred to the forming station via the conveyor system once the target temperature was reached. The conveyor system was made with dual polymer belt with automatic control, which allows the precise transfer of the specimen between the modules. The incubation chamber was used for material pre-treatment and specific OEM paint bake cycle to simulate the FAST process for industrial application. The forming toolset was designed specifically according to the geometry of the final component, and the blank holding force can be adjusted by using the two supported gas springs. The control information of each sub-system was stored on a PIC 4331 microcontroller, which can be easily programmed in C language. In future applications, the processing windows of the different forming process can be programmed and modified remotely via the cloud based FEA platform "Smart Forming", details of which are further discussed in Chapter 6.

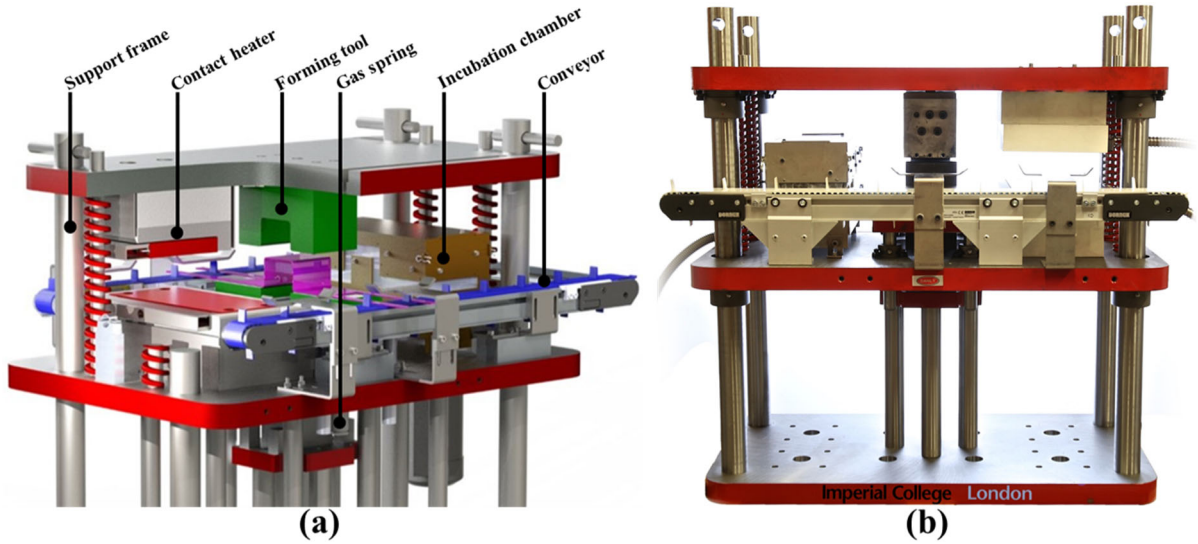

Figure 3.12 The *Uni-Form* pilot production line (a) design in 3D view and (b) final assembly.

The "*Uni-Form*" system was fitted within a 100 tons hydraulic testing machine as shown in Figure 3.13. There were 28 gas springs fitted in the cushion positioned at the base of the machine, which provided adjustable stamping force by charging to 30 bar with 2 independent circuits. Phoenix and "*Uni-Form*" control systems were connected through digital computers. The dedicated heating rate and forming target temperature were entered in the "*Uni-Form*" box and the corresponding forming speed and transfer time were entered in the Phoenix control system. Once the controller was activated, the system automatically operated the entire forming cycle. The safety light guard and emergency stops located around the press machine enabled the safe operation of the equipment.

A U-shaped toolset was designed to conduct forming tests in the present research, with the engineering drawings and 3D view of the die and punch shown in Figure 3.14. The material of toolset was P20 steel and the die clearance was designed to be 0.2 mm which is 10% of the test specimen thickness. During the test, the upper die was moving down towards to lower punch to form the U-shaped component. In addition, there were 6 cooling channels designed to enable the repeatability of the tests.

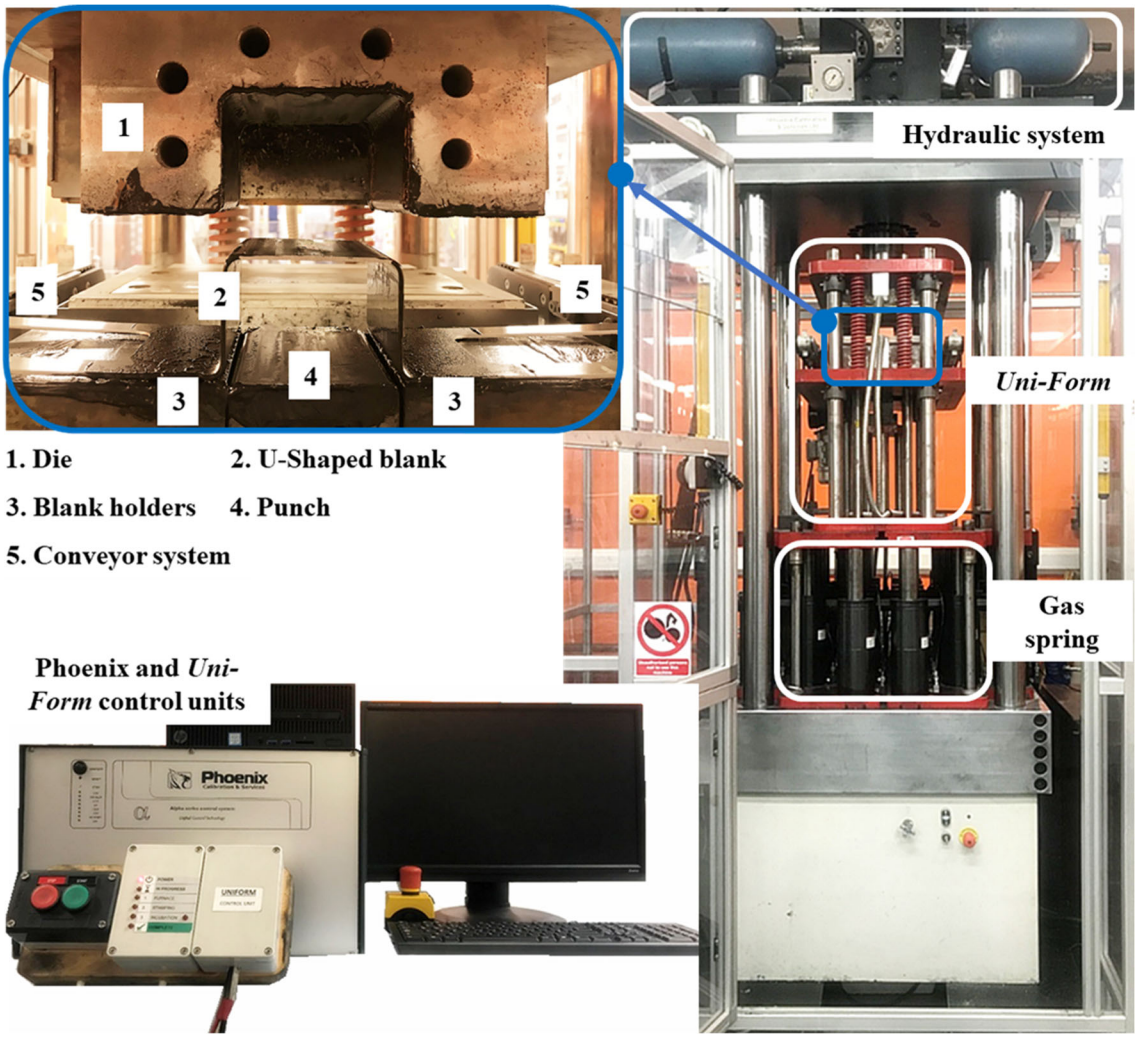

Figure 3.13 Schematic diagrams of the Uni-form within 100 Tons hydraulic press machine and control units.

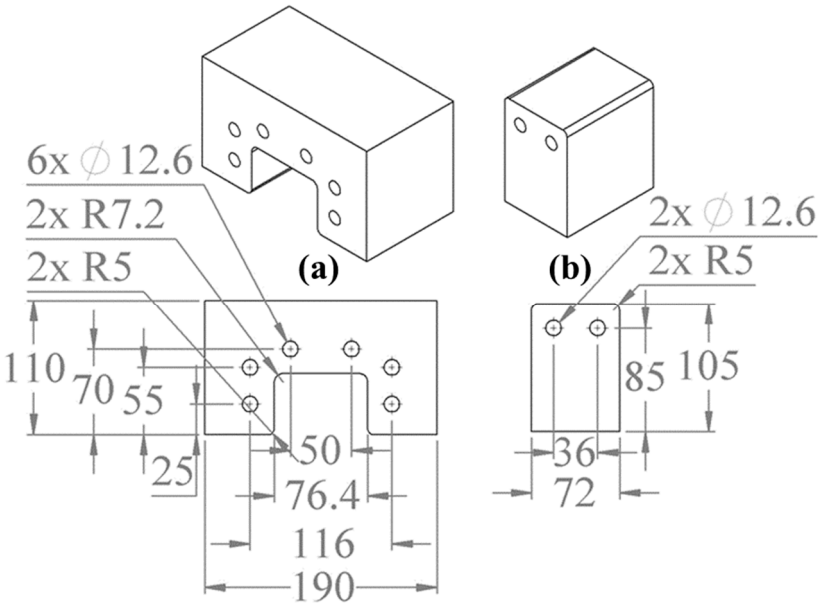

Figure 3.14 Schematic diagram of U-Shaped forming toolset (dimensions are in mm).

3.4.2 Specimen design and experimental program

Figure 3.15 shows the specimen design for the FAST test using the "*Uni-Form*" system. Three pairs of thermocouples were inserted at the designated locations which represent the centre (mid-point), far side (80 mm away from the centre) and near side (40 mm away from the centre). By evaluating the temperature distribution at these three locations, it was found that there was less than 5 % difference between the centre and the edges, which verified the adequate temperature homogeneity in the specimens.

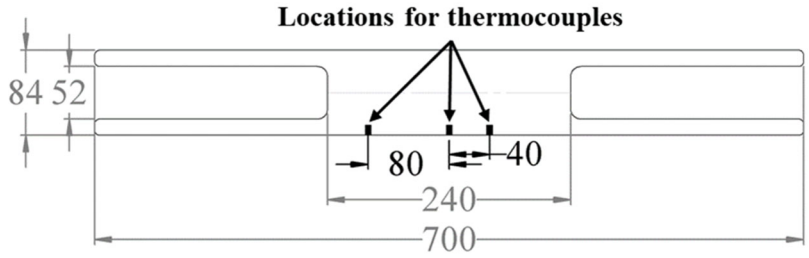

Figure 3.15 Design of U-Shaped forming test specimen (dimension in mm) with thermocouple locations.

Table 3.4 shows the test matrix for U-shaped forming via the "Uni-Form" system. Before each test, the lubricant (Omega 35) was evenly applied to the contact area between the die and punch. The specimen was transferred to the heating station for fast heating from room temperature to the pre-set target temperature at a heating rate at 50 °C/s, then quickly transferred to the forming station via the conveyor system at the time under 4 seconds. Simultaneously, the hot blank was formed at a pre-set forming speed with a 10 kN blank-holding force, and the cold die and punch remained closed for 5 seconds for quenching and reduced springback. The effect of forming temperature, from room temperature to the SHT temperature in both materials was investigated at a forming speed of 250 mm/s. In addition, the effect of forming speed at 75, 150, 250 and 350 mm/s were evaluated at a forming temperature of 300 °C.

Table 3.4 Test matrix for U-shaped forming under FAST conditions.

Materials	Forming Speeds (mm/s) / Temperatures (°C)	RT	200	250	300	400	490	500	535
AA6082	75				√				
	150				√				
	250	√	√	√	√	√		√	√
	350				√				
AA7075	75				√				
	150				√				
	250	√	√	√	√	√	√		
	350				√				

3.4.3 Post-PBC properties evaluation

In order to expand the industrial application of the selected materials, it is necessary to determine the mechanical properties of the formed parts, such as post-PBC hardness/strength.

3.4.3.1 Post-PBC hardness evaluation of U-shaped components

To confirm the uniformity of the components at the post-PBC stage under various FAST test conditions, Vickers hardness tests (HV5) were conducted at the five different regions of the formed component as shown in Figure 3.16, which includes the top, bottom and sidewall. The average value was calculated to represent the mean hardness of the formed part.

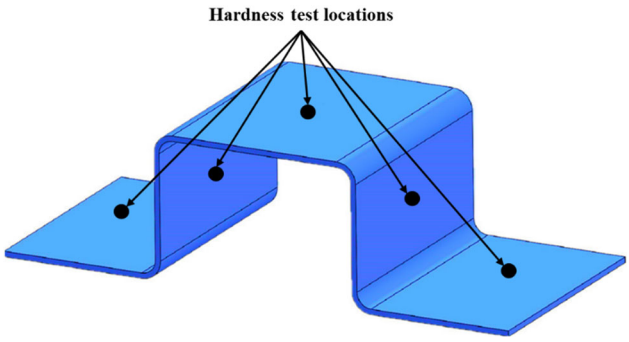

Figure 3.16 Location of test points for U-shape specimen in post-PBC hardness test.

3.4.3.2 Post-PBC strength evaluation of U-shaped components

Post-PBC strength on formed U-shaped components was evaluated through uniaxial tensile tests at room temperature, three dog-bone shaped specimens were waterjet cut from the top region of each formed component, as shown in Figure 3.17 (b). The reason for using waterjet instead of later cutting was to prevent heating and potential alteration of the microstructure in the heat affected zone. Figure 3.17 (a) shows the design of the test specimen, the gauge length was 32 mm and the corresponding width was 6 mm.

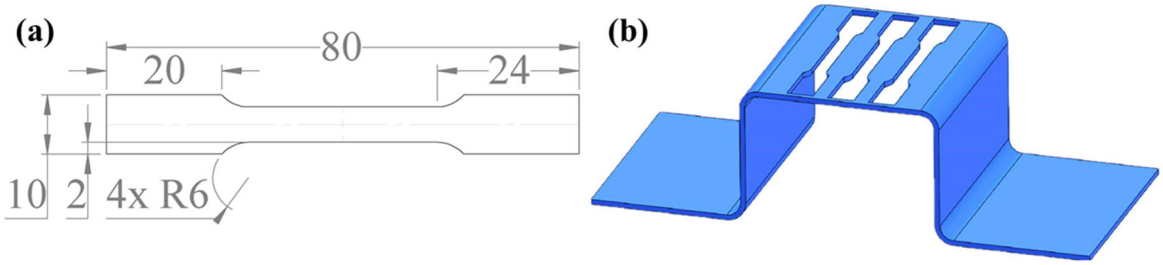

Figure 3.17 Specimen preparation for post-PBC strength evaluation (a) design (dimensions are in mm) and (b) location of tensile test specimens from formed u-shaped parts.

Before each test, the width and thickness of the samples were measured at three different locations and recorded so that the stress can be calculated during the post-processing of the results. A random speckle pattern was sprayed onto the surface of the specimen and the test pieces were assembled into an Instron 3369 tensile testing machine.

Digital Image Correlation (DIC) was used as it is a state of art technology for measuring deformation and failure of the material. DIC uses a full field, non-contact optical technology which is well suited for material characterization both in the elastic and plastic ranges. Figure 3.18 shows the detailed setup for the uniaxial tensile test on the Instron machine. The specimen was clamped by the top and bottom grips to avoid any movement during the test. A computer was connected to the load cell to record the real-time load-displacement. A high-speed camera and light source were employed in the DIC system, the frame rate of the camera was set as 1 fps for the tensile test at a strain rate of 0.001 /s. Strain could be calculated from the recorded images via ARAMIS software. The corresponding stress could be calculated from the force measurements stored on the computer. Therefore, the post-PBC strength can be represented by true stress-strain by converting the engineering stress-strain recorded values.

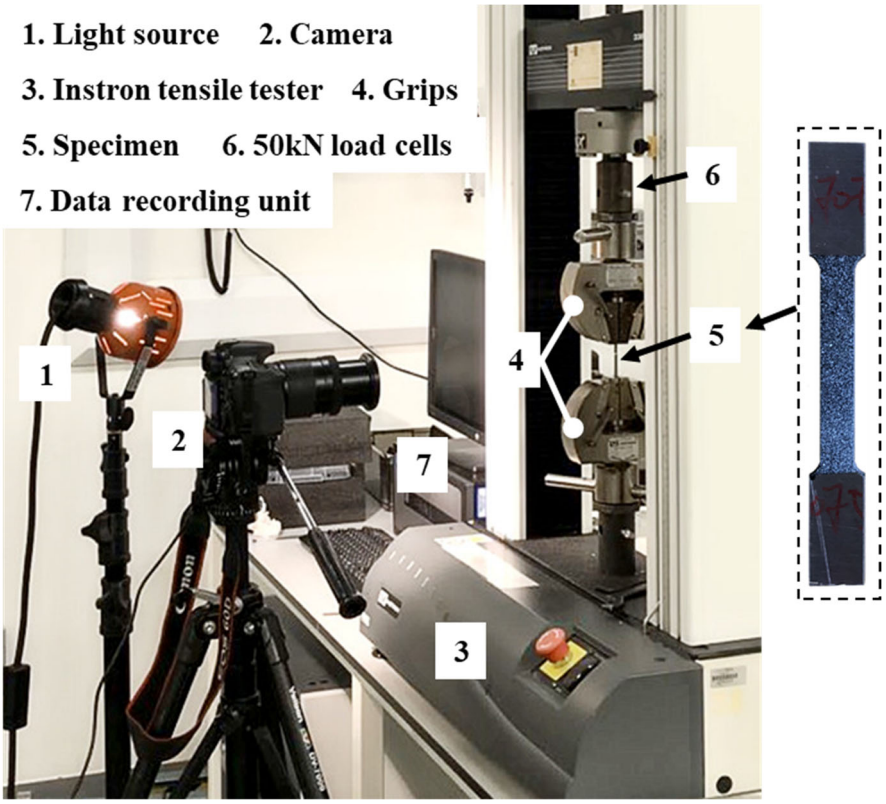

Figure 3.18 Schematic diagram of tensile test set up at room temperature with DIC system.

3.4.4 Springback analysis process

Springback of the AA6082 and AA7075 was investigated after stretch bending under various forming temperatures and forming speeds. For accurate measurement of springback, the deflection angles were measured by first scanning the edges of the formed components by using Coordinate Measurement Machine (CMM) and digital scanner, then using image processing software to define the outlines of the edges and finally using a 2D drawing software SolidWorks to define vertical and horizontal lines along the edge as seen in Figure 3.19. Finally, the angles θ_A and θ_B were determined to evaluate the associated springback.

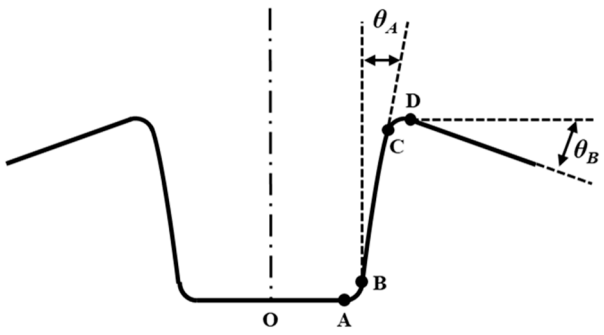

Figure 3.19 Indication of measurement of springback angle θ_A and θ_B for U-shaped formed components.

In order to further investigate the springback behaviour of the AA6082 and AA7075 under FAST conditions, the FE simulation for the U-shaped bending was developed and validated with experimental results. The FE springback simulation setup can be found in the Appendix section.

3.5 Summary

In this chapter, two materials of AA6082 and AA7075 were introduced to produce Dissimilar Alloys – Tailor Welded Blanks (DA-TWBs). A novel sheet metal forming technology, Fast light Alloys Stamping Technology (FAST) was proposed, which increases the mass production rate and reduces the development and production cycle time for stamped vehicle components. Uniaxial tensile tests were designed and conducted to investigate the material flow behaviour at different forming temperatures and strain rates. Strength degradation tests were performed to investigate post-PBC hardness as a function of pre-treatment time, heating rate, soaking time, forming temperature and quenching rate. A U-shaped forming test via a dedicated automatic pilot production line "*Uni-Form*" was used to verify the FAST process. A series of post-PBC properties and springback were investigated at various forming temperatures and forming speeds to determine the accuracy and performance of the components.

Chapter 4. Development of FAST process and implementation on forming U-shaped components made from DA-TWBs

In this chapter, the results obtained from the experiments which were introduced in the previous chapter are presented and discussed in detail. Specifically, the structure of this chapter is shown in Figure 4.1.

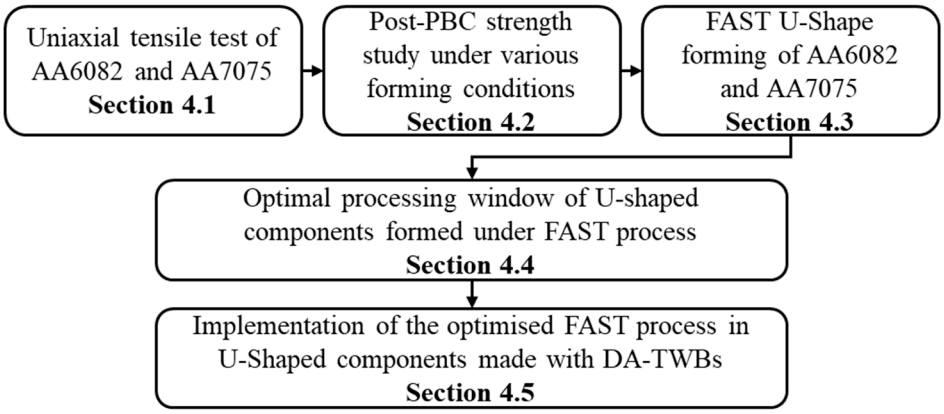

Figure 4.1 Schematic diagram for major sections covered in Chapter 4.

Firstly, the thermo-mechanical properties and viscoplastic deformation of the AA6082 and AA7075 alloys under FAST conditions were evaluated with the effect of temperature and strain rate on the material properties. Secondly, based on the strength degradation test results, the post-PBC hardness evolution of the AA6082 and AA7075 under FAST conditions was analysed, in terms of pre-treatment time, heating rate, soaking time, forming temperature and quenching rate. Thirdly, forming trials for the proposed FAST process were conducted through dedicated pilot production line "Uni-Form". The post-PBC hardness and springback of formed

---

The work performed in Chapter 4 leads to the publication of patent: "Cai, Z., Liu, X., Zhang, Q., Wu, G., Zhu, M., Wang, L., 2020. Method of forming parts from tailor-welded blanks manufactured by dissimilar alloys. Patent application number: CN2020xxxxxxxx.x (Currently in the stage of Prior Art Review in the UK and China)

Chapter 4 is based on the publication: "Cai, Z., Batthyangy, P., Dhawan, S., Zhang, Q., Sun, Y., Luan, X., Wang, L., 2018. Study of springback for high strength aluminium alloys under hot stamping. Advanced high strength steel and press hardening. 117-121. Doi: 10.1142/9789813277984_0019"

U-shaped components were investigated under different forming temperatures and forming U-shaped components were investigated under different forming temperatures and forming speeds. Finally, an optimal FAST forming condition for forming U-shaped components made from DA-TWBs was summarised, which includes the detailed processing window of material pre-treatment, forming and post paint-back cycles. Additionally, in order to verify the proposed forming parameters, a U-shaped component made from DA-TWBs was formed under the optimal FAST conditions. The post-PBC properties including post-PBC hardness, springback and thickness reduction were also investigated in detail.

4.1 Thermo-mechanical properties of the aluminium alloys at various test conditions via uniaxial tensile test

4.1.1 Temperature distribution of the AA6082 and AA7075 at elevated temperature

The temperature distribution of the dog-bone shaped specimens used in uniaxial tensile test, ranging between 300 and 500 °C is illustrated in Figure 4.2.

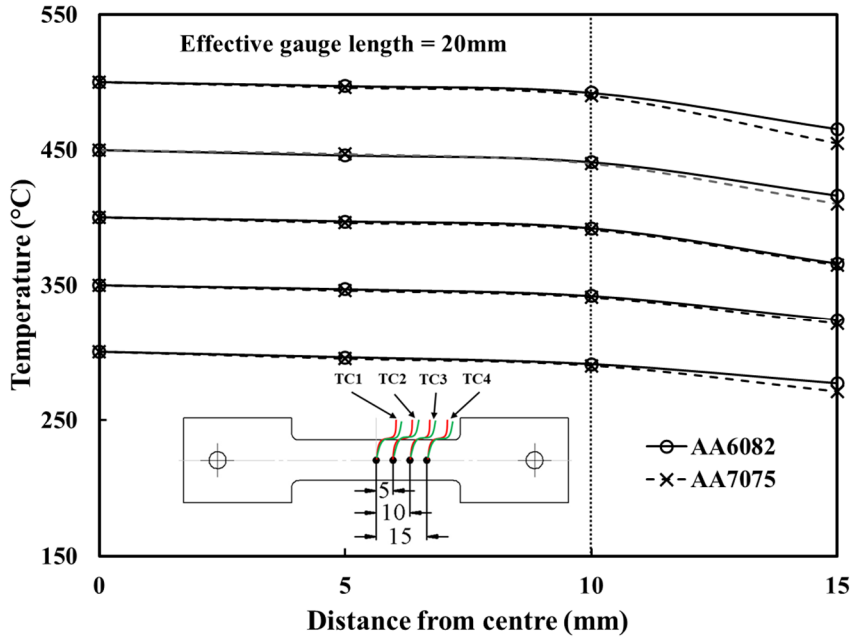

Figure 4.2 Temperature distribution in the dog-bone shaped specimen at various temperatures for the AA6082 and AA7075 respectively.

A similar trend of the temperature evolution is observed at various temperatures for both materials, with a decreasing temperature slope (temperature gradient) occurring after 10 mm (TC3) from the centre. A maximum temperature difference occurs at 15 mm (TC4) from the centre. At TC4, the temperature difference (ΔT) compared to the centre point (TC1), is in the average of 30 °C. In addition, it is clear to see that the temperature difference (ΔT) in the AA7075 is greater than in AA6082 at the position of TC4. The lower thermal conductivity of AA7075 (130 $Wm^{-1}K^{-1}$) compared to AA6082 (180 $Wm^{-1}K^{-1}$) can explain the difference between these two materials (Aalco, 2020, ASM, 2020).

Table 4.1 shows the temperature difference between TC3 (10 mm from the centre) and the centre point TC1 in the AA6082 and AA7075, respectively. It is clear to see that the temperature difference increases with increasing test temperature, and there is only a minor change of temperature difference within 10 °C. According to previous research, the effective gauge length is selected when the temperature difference (ΔT) is within 10 °C to the centre temperature in uniaxial tensile tests (Shao et al., 2017). Therefore, the effective gauge length of 20 mm can be defined for the specimen, and this value is used to calculate the true strain during post-processing of experimental data.

Table 4.1 Temperature difference between TC3 (10mm) and centre point TC1.

Temperature at TC_1 (°C)	**300**	**350**	**400**	**450**	**500**
ΔT (°C) in AA6082	7.58	7.84	8.45	8.97	9.23
ΔT (°C) in AA7075	7.64	7.93	8.67	9.03	9.46

4.1.2 Flow stress-strain curves

The effects of temperature and strain rate on the flow behaviour of the AA6082 and AA7075 were investigated at a temperature range between 300 °C and the SHT temperature, with strain rates tested from 0.1 to 5 s^{-1}. The true stress-strain curves for the two effects are illustrated in Figure 4.3 and 4.4.

4.1.2.1 Study on the effect of temperature of the AA6082 and AA7075

The true stress-strain curves for AA6082 are shown in Figure 4.3 (a), which indicated that the increase of testing temperature leads to a decrease in flow stress but an increase in the ductility of the material.

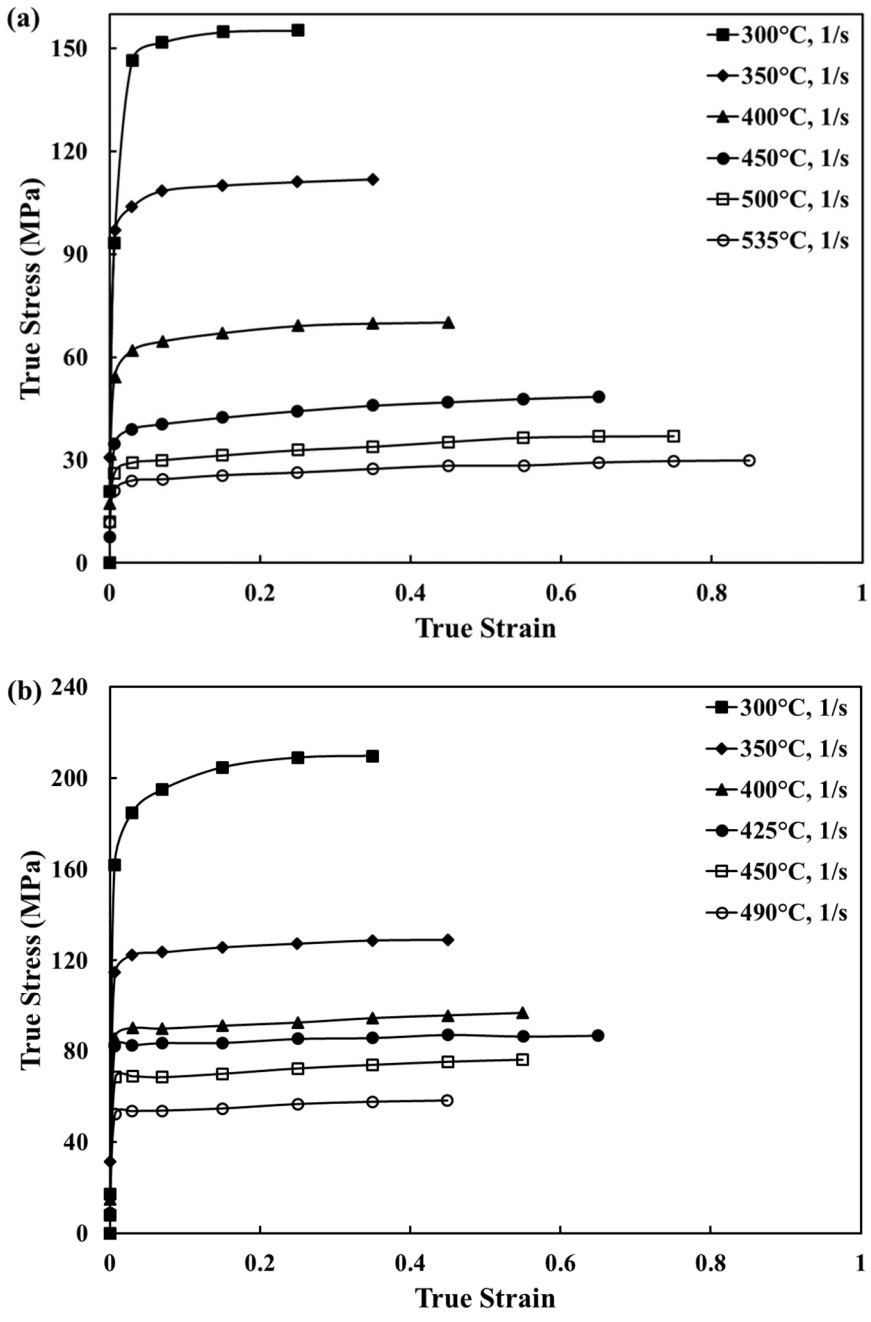

Figure 4.3 Flow stress-strain curve of (a) AA6082 and (b) AA7075 at different temperatures.

The failure strain (strain at fracture) increases from 0.25 to 0.85 when the temperature increases from 300 to 535 °C. According to the previous research, this phenomenon is thermally

activated as the mobility of dislocations is enhanced at higher temperatures due to the activation of diffusion-controlled processes, such as grain boundary rotation and dynamic recovery (Mohamed et al., 2012). However, this phenomenon was not observed in the case of AA7075.

Figure 4.3 (b) shows the true stress-strain curves of AA7075, which indicated that the flow stress decreased with increasing temperature, although the failure strain increased when the temperature was raised from 300 to 425 °C. The reduction in flow stress and increase in failure strain can be explained by thermally activated deformation mechanisms. As the temperature increases, the mobility of atoms and dislocations is enhanced. Therefore, the material becomes softer and more ductile. However, after 425 °C, the ductility decreased sharply. The failure strain at 490 °C is approximately 0.45 which is the same as the test performed at 350 °C. A similar trend was observed from previous research with other Al-Cu based alloys such as AA2024 (Wang et al., 2011).

For the typical heat-treatable aluminium alloys mostly used in the car industry, such as 6 series aluminium alloys, the soluble precipitates and inclusions dissolve into the matrix at SHT temperature. Therefore, the ductility of the alloys increases to the maximum value, which is due to the increase of dislocation motion during deformation (Davis, 2004). On the other hand, the ductility of AA7075 was reduced at SHT temperature due to the low melting eutectic phase Cu and Mg (Wang et al., 2011). In conclusion, the flow stress decreased with increasing testing temperature and reached the maximum failure strain at 535 °C and 425 °C for the AA6082 and AA7075, respectively.

4.1.2.2 Study on the effect of strain rate of the AA6082 and AA7075

The effect of strain rate on the flow stress at 535 °C and 425 °C are shown in Figure 4.4, which shows the relationship between strain rate and material ductility. In Figure 4.4 (a), the flow stress and ductility of AA6082 increase with increasing strain rate due to the strain rate hardening effect. Similar results were found in the literature (Lassance et al., 2007). The failure strain increased from 0.65 to 0.95 when the strain rate increased from 0.1 to 5 s^{-1}. The effect of grain growth theory can be used to explain this phenomenon, as the grain size grows within the aluminium matrix at a lower strain rate (Mohamed et al., 2012). In addition, the reduction of dislocation spacing leads to an increase in flow stress. In Figure 4.4 (b), the flow stress of AA7075 increases with increasing strain rate due to the strain rate hardening effect. On the other hand, the lower failure strain of AA7075 occurs at high strain rate. The failure strain

reduced from 0.72 to 0.45 when the strain rate increased from 0.1 to 5 s^{-1}. Therefore, the increasing strain rate has a positive effect on the ductility of AA6082 but a negative effect on AA7075. Moreover, an increase in strain rate leads to increasing material flow stress.

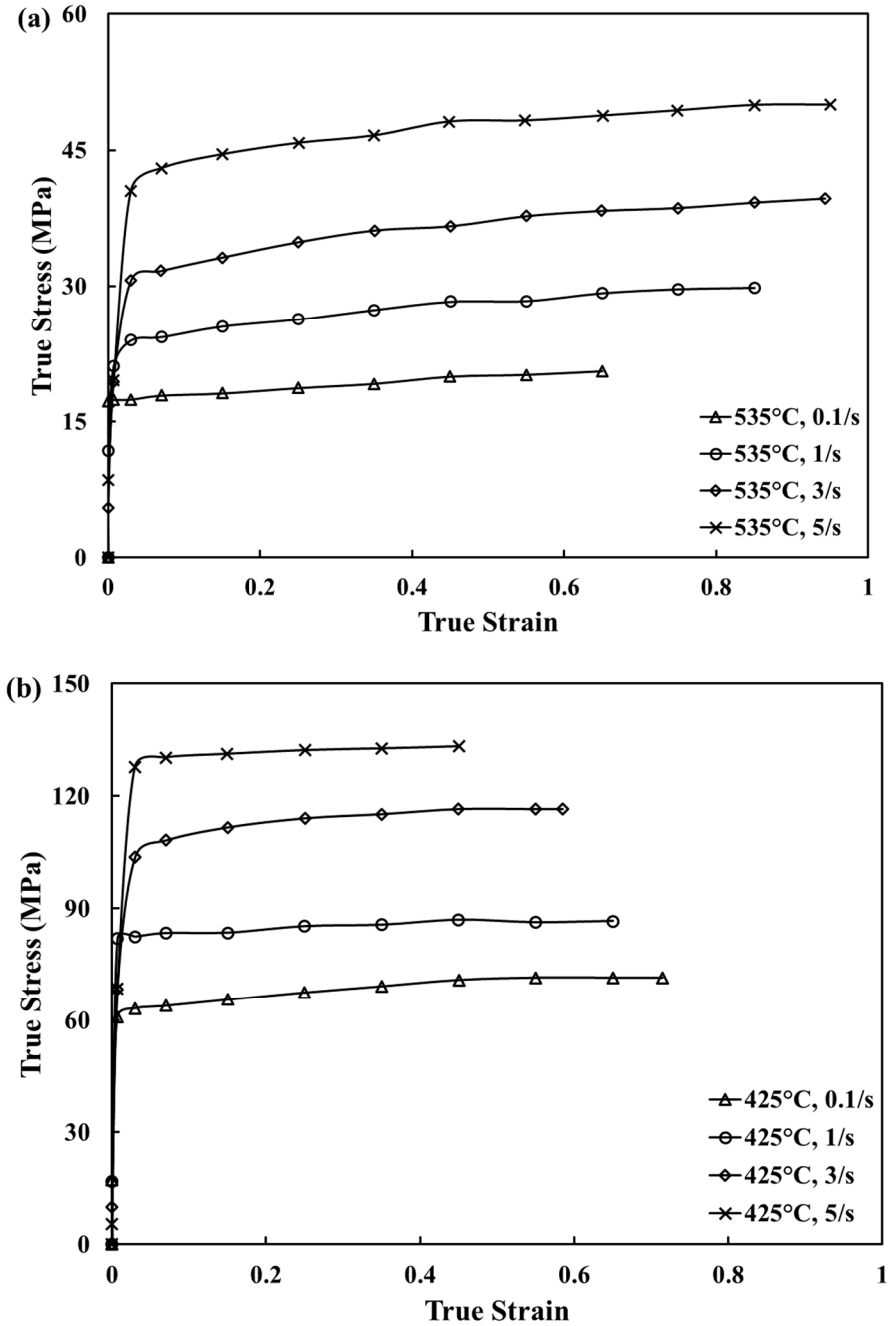

Figure 4.4 Flow stress-strain curve of (a) AA6082 and (b) AA7075 at different strain rates.

4.2 Post-PBC hardness evolution of the AA6082 and AA7075 under different forming conditions

Apart from elevated temperature deformation behaviour, post-PBC strength behaviour was also affected by the forming process parameters. The performance of post-PBC hardness was evaluated with various effects including pre-treatment time, heating rate, soaking time, forming temperature and quenching rate. All the results have been illustrated on the following five sub-chapters with two graphs presented in each figure, in which (a) represents the results of AA6082 and (b) represents the results of AA7075. Each test specimen was measured with the hardness at three different stages and repeated 5 times for each test, where the 'Triangle', 'Diamond' and 'Dot' symbols show the hardness measurement after pre-treatment, heating and quenching and paint bake cycle, respectively. In addition, the value of measured post-PBC hardness was also compared with the as-received hardness of the material which is shown on the sub-axis as a percentage. For reference, the hardness value of the as-received material was approximately 120 HV and 180 HV for AA6082 and AA7075, respectively.

4.2.1 Effect of pre-treatment time on post-PBC hardness of the AA6082 and AA7075

Figure 4.5 shows the change of post-PBC hardness of the AA6082 and AA7075 as a function of pre-treatment time, where an increasing trend was found in both figures. Error bar shows the highest and lowest post-PBC hardness which were measured from 5 samples for each test condition. It is clear that the pre-treatment temperature and time plays a significant role in the post-PBC hardness of AA6082 and AA7075. In Figure 4.5 (a), the pre-treatment was conducted at 180 °C and soaked for a time ranging between 0 to 150 minutes. The post-PBC hardness increased dramatically within the first 45 minutes from 85 to 115 HV. After this point, the post-PBC hardness increased much more slowly and reached the peak hardness of 120 HV at 1 hour pre-treatment time, which is 100 % compared with the as-received hardness. The post-PBC hardness was in a steady-state at peak hardness, but reduced after 150 minutes due to the effect of over ageing during the pre-ageing process. In Figure 4.5 (b), the pre-treatment was conducted at 120 °C, the similar trend of increasing post-PBC hardness was also observed for the test of AA7075. The sharp growth of post-PBC hardness from 123 to 174 HV occurred within the first 75 minutes, and then slightly increased to reach a peak hardness value of 185

HV within 2 hours, which is 103 % compare with the as-received material. There was an approximately 4 % decline on the post-PBC hardness at the time of 150 minutes compared with the peak hardness, which is an indication of the start of over ageing on the test material.

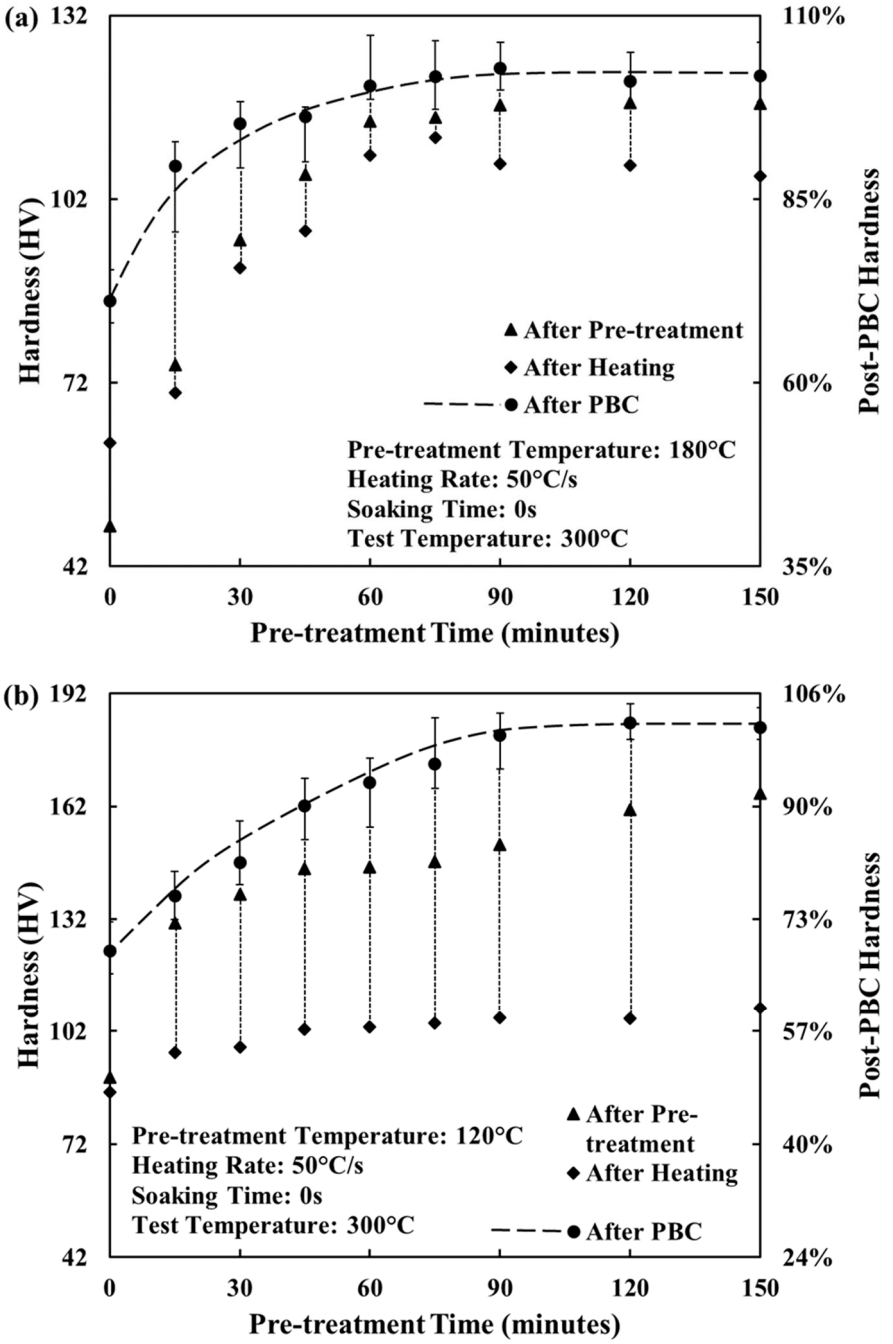

Figure 4.5 Evolution of the post-PBC hardness at different pre-treatment time without deformation for (a) AA6082 and (b) AA7075.

Prior to each pre-treatment, all the experimental samples were solution heat-treated and immediately quenched to room temperature with an accurate control of the SHT temperature and time, which enables the formation of the homogeneous supersaturated solid solution

(SSSS). At this point, artificial ageing was involved to accelerate the generation of a large amount of fine precipitates. Hence, the hardness of the specimen increased with time due to the high density of precipitates and high shear stress required to move the dislocations. Therefore, less dislocation motion lead to higher hardness. On the other hand, the fine distribution of precipitates changed into a coarse distribution when over ageing occurred, which led to a low precipitate density and the internal particle spacing was increased. Therefore, the hardness of the specimens decreased during over ageing due to the low shear stress to move the dislocations. According to the results, the suggested pre-treat time is 60 and 70 minutes for AA6082 and AA7075, respectively.

4.2.2 Effect of heating rate on post-PBC hardness for AA6082 and AA7075

Figure 4.6 shows the change of post-PBC hardness of the AA6082 and AA7075 as a function of heating rate, where a dramatic increasing trend was found in both figures. Error bar shows the highest and lowest post-PBC hardness which were measured from 5 samples for each test condition. It is clear that the heating rate plays a significant role in the post-PBC hardness of the AA6082 and AA7075 during the FAST process. In addition, the test was conducted by heating the material to the same target temperature of 300 °C at a range of heating rates from 1 to 200 °C/s. In Figure 4.6 (a), it is clear that the slow heating rate (1 °C/s) has a negative effect on the post-PBC hardness, as the hardness value decreased from 115HV after pre-treatment to 104 HV after heating and PBC. On the other hand, the post-PBC hardness rose dramatically with increasing heating rate up to 10 °C/s. Beyond that heating rate, a steady-state post-PBC hardness at the peak was observed, which was approximately 101% compared with the as-received material. Figure 4.6 (b), confirms that the slow heating rate affects the post-PBC hardness. On the other hand, the peak post-PBC hardness was observed when the heating rate reached 50 °C/s and was maintained at a peak value with a fast heating rate.

During the FAST process, the blank was fast heated to a target temperature and formed and quenched at the same time in the cold die. According to the time-temperature transformation diagram of AA6xxx and AA7xxx, the precipitate transformation could be avoided if both quenching and heating rate were at a critical value. The hardness could be maintained as there was minimised or negligible precipitation behaviour. However, the slow heating allows for the formation of a coarse precipitate, which results in fast growth with slow nucleation. Thus, more dislocation motion will lead to lower hardness with a slow heating rate. Therefore, according to the results, the suggested heating rate for both materials in DA-TWBs is 50 °C/s.

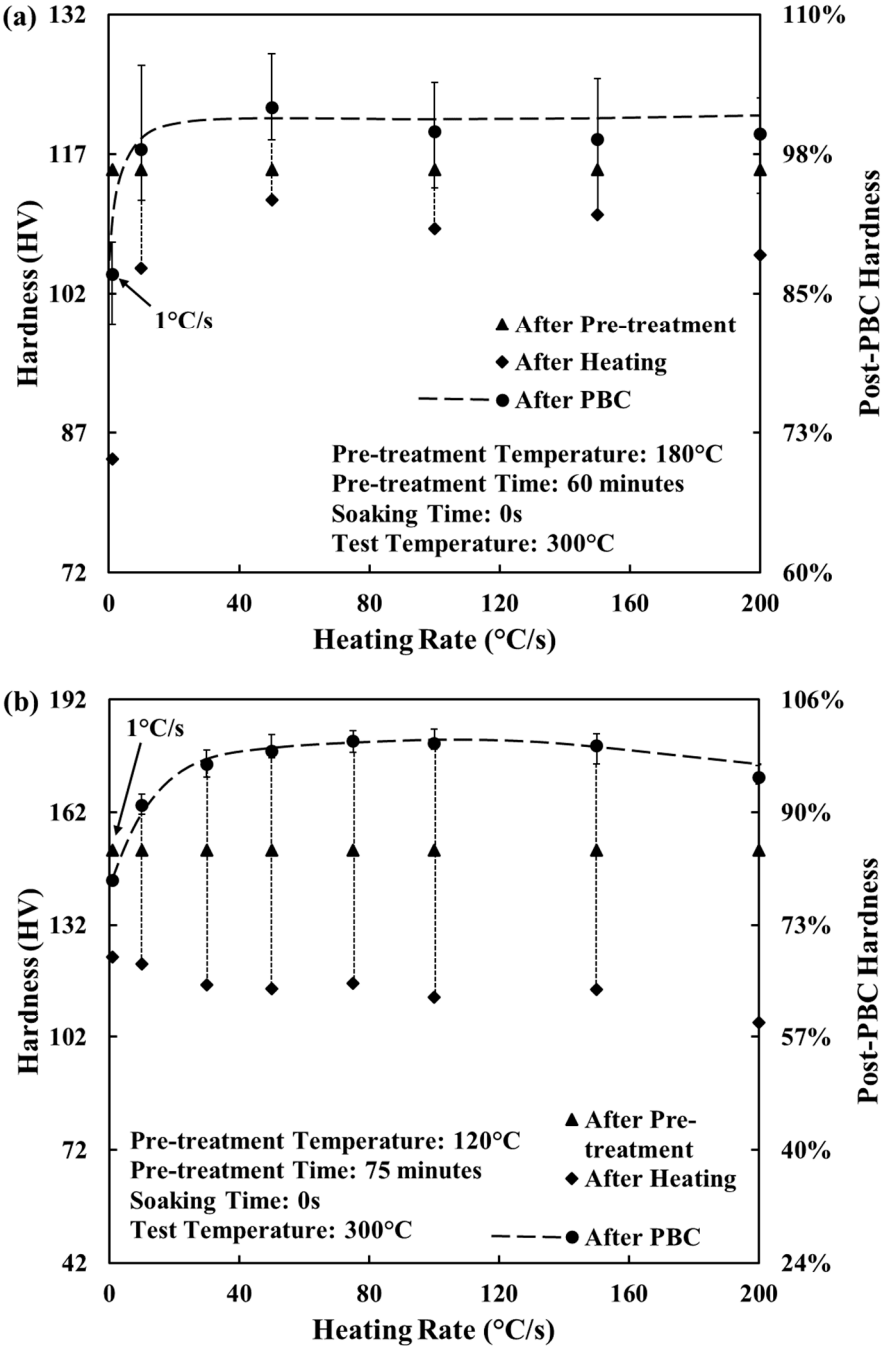

Figure 4.6 Evolution of the post-PBC hardness at different heating rates without deformation for (a) AA6082 and (b) AA7075.

4.2.3 Effect of soaking time on post-PBC hardness of the AA6082 and AA7075

Figure 4.7 shows the change of post-PBC hardness for AA6082 and AA7075 as a function of soaking time, where a linearly decreasing trend was found in both figures. Error bar shows the highest and lowest post-PBC hardness which were measured from 5 samples for each test

condition. It is clear that soaking time plays a significant role in the post-PBC hardness of the AA6082 and AA7075 during the FAST process. In addition, the test was conducted to soak the specimen at the target temperature of 300 °C between 0 and 8 seconds. In Figure 4.7 (a), it is clear to see the post-PBC hardness decreased from the peak value of approximately 99 % to 90 % compared with the as-received material. In addition, the same decreasing trend was also observed in Figure 4.7 (b) with a 10 % drop of post-PBC hardness when soaked for 8 seconds. This observation is expected to continue with the increasing soaking time. By assessing the precipitation behaviour, the longer soaking period at 300 °C led to the generation of metastable precipitates, which is the main barrier to increasing post-PBC hardness through PBC. Hence, the shorter soaking time will lead to fewer or completely avoid coarse precipitates. Therefore, according to the results, the suggested soaking time on the FAST process for these two materials is as short as possible and ideally none at all, i.e. 0 seconds.

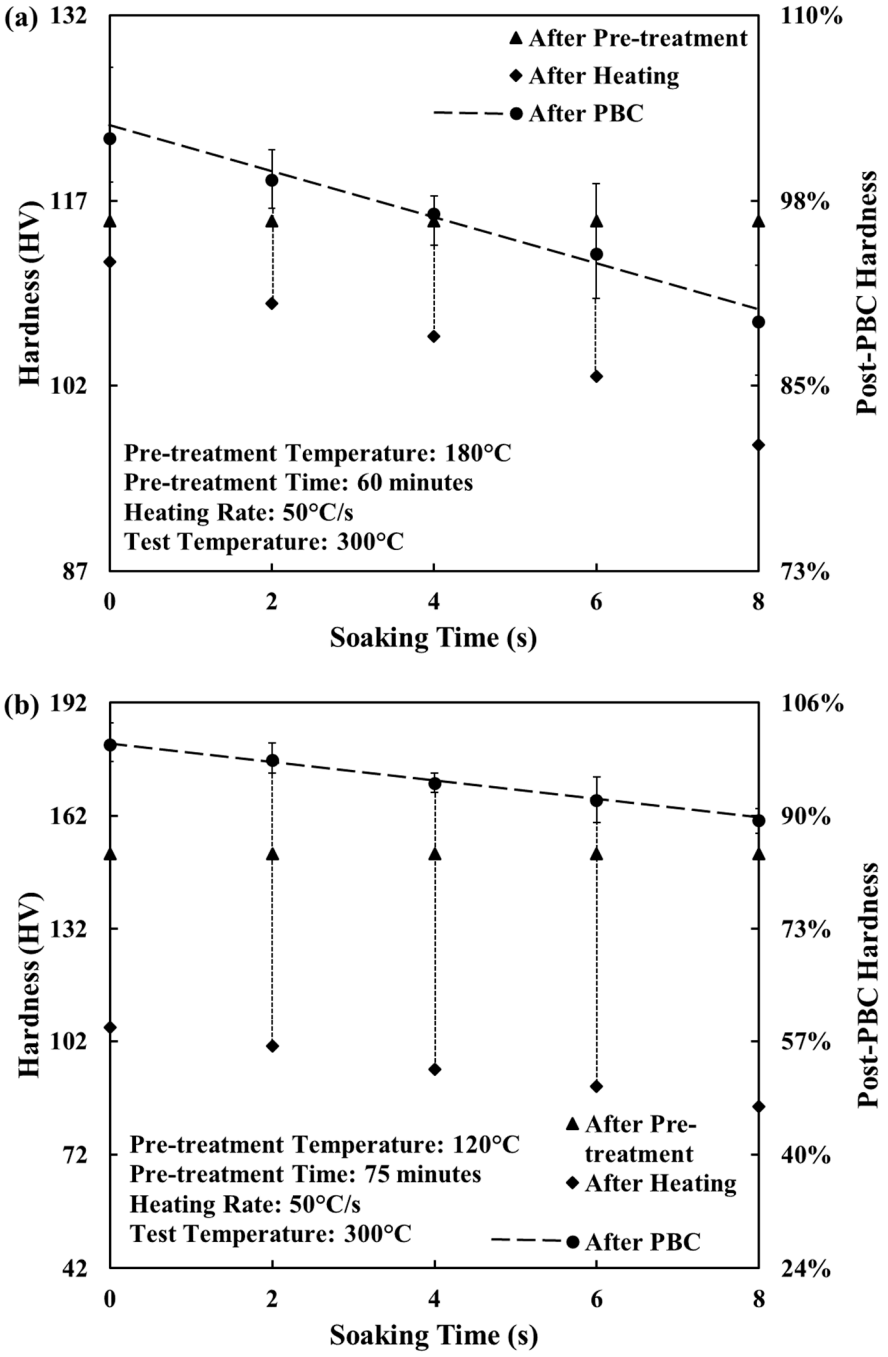

Figure 4.7 Evolution of the post-PBC hardness at different soaking times without deformation for (a) AA6082 and (b) AA7075.

4.2.4 Effect of forming temperature on post-PBC hardness of the AA6082 and AA7075

Figure 4.8 shows the change of post-PBC hardness of the AA6082 and AA7075 as a function of forming temperature, where a similar trend was found in both figures. Error bar shows the highest and lowest post-PBC hardness which were measured from 5 samples for each test

condition. It is clear that forming temperature plays a significant role in the post-PBC hardness of the AA6082 and AA7075 during the FAST process. In addition, the test was conducted to heat specimens to different forming temperatures ranging from room temperature to SHT temperature at a constant heating rate of 50 °C/s without soaking. In Figure 4.8 (a), it is clear to see there is a significant impact on post-PBC hardness as the forming temperature was raised above 300 °C. The post-PBC hardness reduced from 122 to 72 HV which is an approximate 40 % reduction when the forming temperature was increased from 300 to 400 °C. The increasing trend of post-PBC hardness was observed between 400 and 535 °C which reached approximately 83 % of the as-received material. However, 83 % of the post-PBC hardness limits the useful applications of AA6082 and AA7075 on a car, as it was required over 90 % of post-PBC hardness with the force concentration components (Klampfer, 2017). On the other hand, the similar trend was found in Figure 4.8 (b), where the lowest post-PBC hardness occurs at the forming temperature of 400 °C (60 % of hardness for the as-received AA7075). Approximately 20 % recovery of post-PBC hardness was obtained at the forming temperature of 490 °C which is the same as the SHT temperature for AA7075, however, this is still 25 % lower compared with the peak hardness value at 300 °C.

During the FAST forming above 300 °C, the increase of temperature will result in more nucleation of the metastable phase, which leads to a decrease of the post-PBC hardness. In addition, the solubility of the aluminium matrix was enhanced with increasing forming temperature, which allows the precipitates to dissolve into the matrix, hence reducing the post-PBC hardness. However, the precipitates were not fully dissolved into the matrix due to the short soaking time at SHT temperature, which leads to incomplete heat treatment, and thus the post-PBC hardness was not fully recovered. Therefore, a forming temperature of 300 °C is suggested.

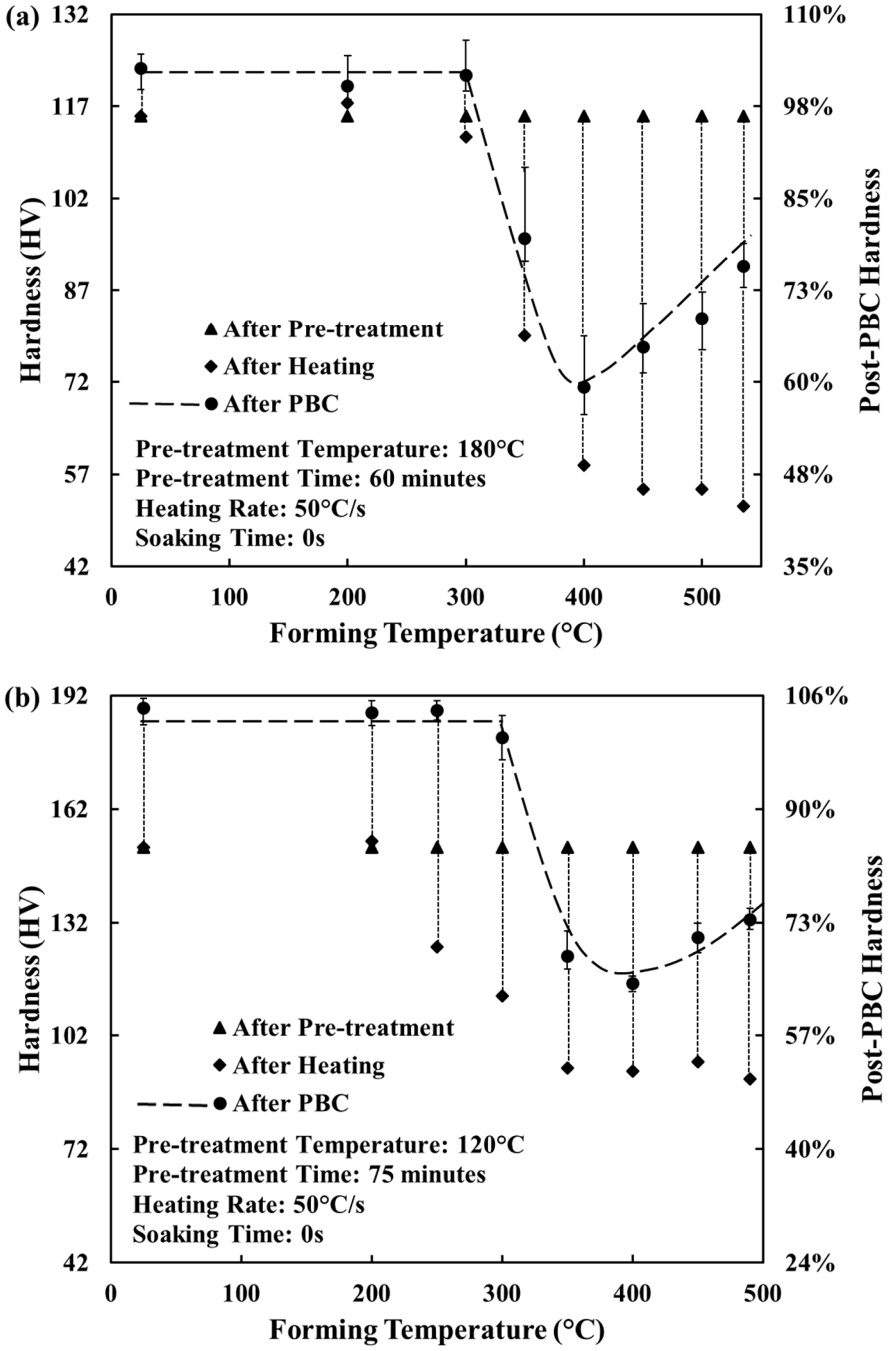

Figure 4.8 Evolution of the post-PBC hardness at different forming temperatures without deformation for (a) AA6082 and (b) AA7075.

4.2.5 Effect of quenching methods on post-PBC hardness of the AA6082 and AA7075

Figure 4.9 shows the change of post-PBC hardness of the AA6082 and AA7075 as a function of quenching methods, the error bar shows the highest and lowest post-PBC hardness which were measured from 5 samples for each test condition. It was found that water quenching

results in an approximately 5 % increase in hardness compared with cold die quenching for both AA6082 and AA7075. The super-fast cooling rate achieved via water quenching minimised or eliminated the precipitation coarsening and the precipitation remained in a slow-growth condition which allows for the growth of fine precipitates. Hence, the post-PBC hardness water quenched specimen exhibited a slightly higher post-PBC hardness than the cold die quenched. Therefore, according to the results, a fast quenching rate is preferred for the FAST process in order to minimise the post-PBC hardness (strength) reduction.

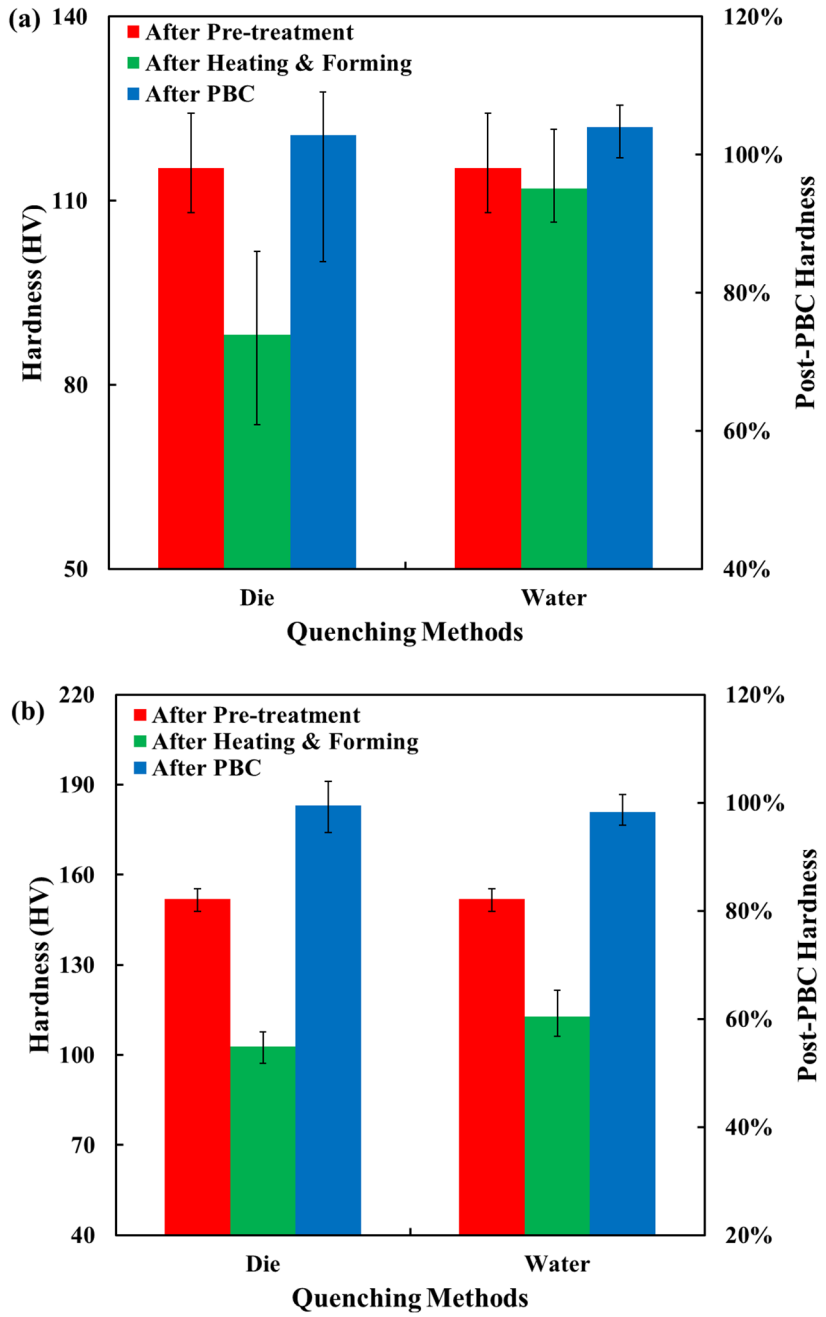

Figure 4.9 Evolution of the post-PBC hardness at different quenching methods without deformation for (a) AA6082 and (b) AA7075.

4.3 Forming tests of U-shaped components of the FAST process

In this research, forming trials for the proposed FAST process were conducted through the dedicated pilot production line "*Uni-Form*". The mechanical properties including post-PBC hardness of formed components under the suggested forming conditions from the previous post-PBC hardness study were presented. In addition, the effect of forming temperature and forming speed on springback and post-PBC hardness of formed components were also investigated.

4.3.1 Mechanical properties of formed components

The proposed FAST process was validated by producing U-shaped components from 2 mm aluminium alloy (AA6082 and AA7075) blanks at forming temperatures between 300 °C and SHT temperature at forming speeds ranging from 75 to 350 mm/s. Figure 4.10 shows a U-shaped component that was successfully formed under the suggested forming conditions at 300 °C with a forming speed of 250 mm/s. It is clear that there were no cracking or necking regions in the formed component.

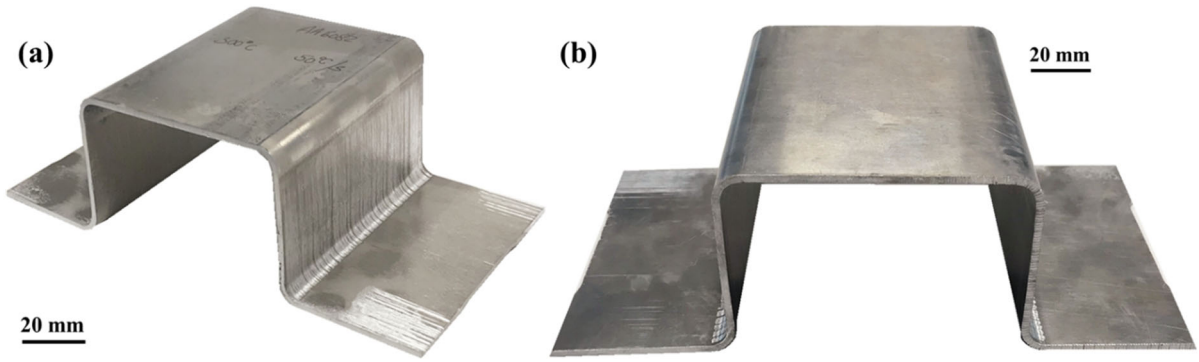

Figure 4.10 FAST forming of (a) AA6082 and (b) AA7075 U-shaped component.

Figure 4.11 shows the post-PBC hardness evolution of formed parts at 8 different test locations from both AA6082 and AA7075. It is clear to see that the hardness was distributed evenly along the cross-section of the U-shaped parts, with the post-PBC hardness value of approximately 118 and 178HV for AA6082 and AA7075, respectively. By comparing with the hardness of as-received materials, the FAST formed U-shaped component under the suggested forming window can achieve a 98 % hardness recovery. In addition, this result is consistent with the degradation test results shown in the previous section 4.2.

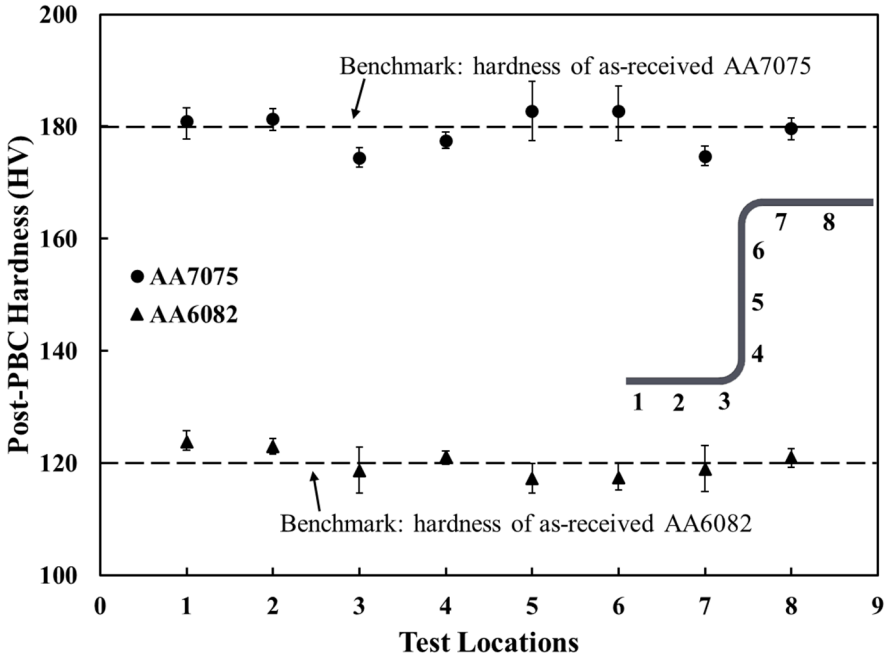

Figure 4.11 Distribution of post-PBC hardness on different locations of the U-Shaped component formed at 300°C for AA6082 and AA7075, respectively.

Dog-bone shaped specimens were waterjet cut from the top surface on the formed U-shaped components and tensile tests were performed at room temperature to examine the mechanical properties. Figure 4.12 illustrates the effect of forming temperature on the flow behaviour of the AA6082 and AA7075 subject to a tensile force at a constant strain rate of 0.001 s^{-1}. It is clear that the temperature has a negative correlation to flow stress, where flow stress decreased with increasing forming temperature. However, the positive relation between forming temperature and failure strain was found. In Figure 4.12 (a), the ductility of the AA6082 which was formed at 300 °C indicated that strain to failure improves by approximately 14 % compared to as-received material. The reason for that improvement is because of the more active precipitation of coarser precipitates at elevated temperature, and hence the material becomes ductile. In Figure 4.12 (b), the similar trend of decreasing flow stress with increasing forming temperature was observed. The ductility of AA7075 which was formed at 300 °C shows there was an improvement of approximately 10 %, and was further improved to 20 % when formed at 450 °C. However, due to the low melting eutectics phases Cu and Mg, the failure strain decreased when the temperature approached SHT temperature, with a reduction of 12 %.

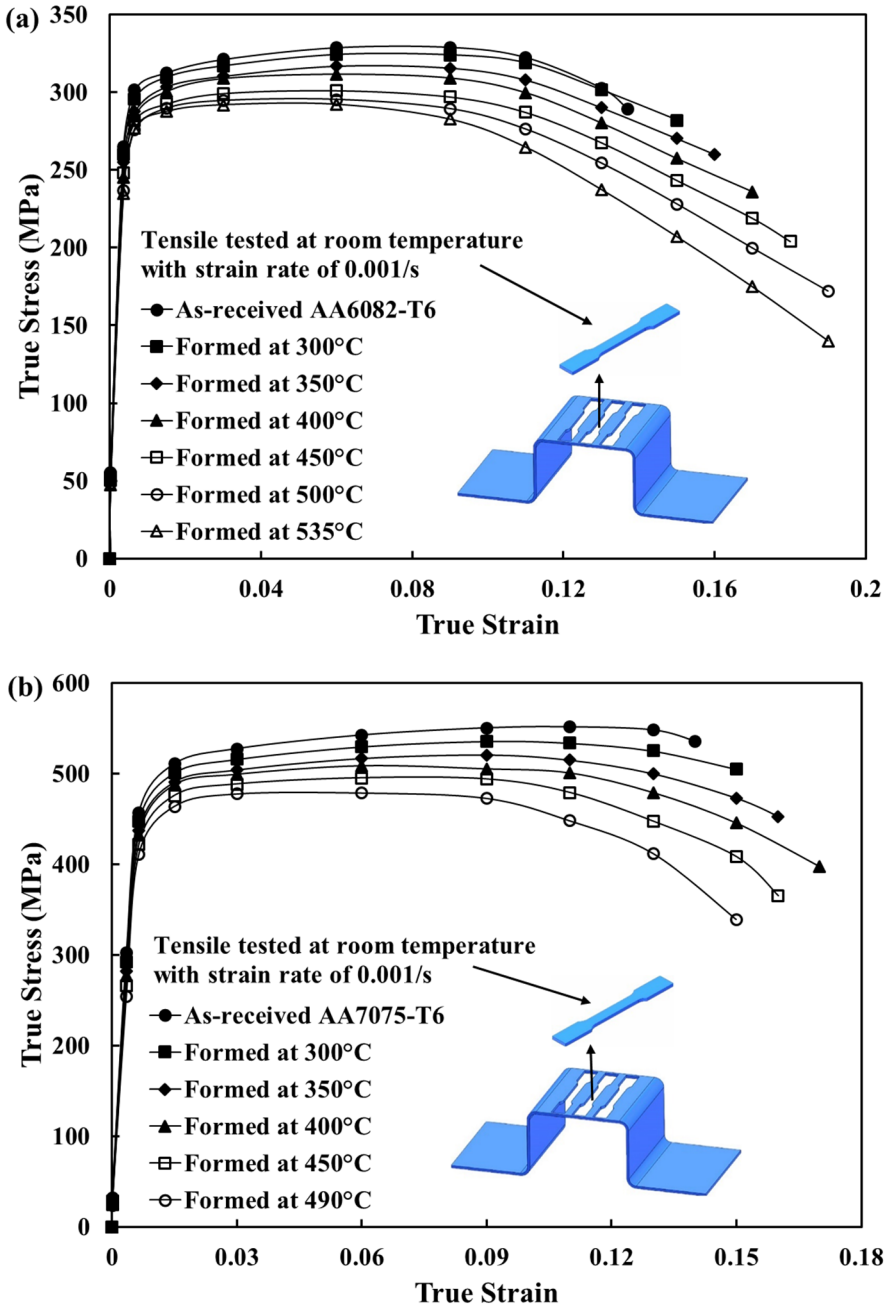

Figure 4.12 Flow stress-strain curves of post-PBC material formed at various temperatures for (a) AA6082 and (b) AA7075.

4.3.2 Springback and post-PBC hardness analysis of U-Shaped components

4.3.2.1 Effect of forming temperature

Figure 4.13 illustrates the effect of forming temperature on post-PBC hardness and springback angle for AA6082 and AA7075 U-shaped components formed by using FAST and cold stamping (formed at room temperature). Error bar shows the highest and lowest post-PBC hardness which were measured from 5 samples for each test condition. According to the

forming tests conducted at room temperature, the U-shaped part was fractured on both materials, which confirms the high strength aluminium alloys is not suitable for cold stamping. In Figure 4.13 (a), a similar trend of the post-PBC hardness was found which was shown in the previous section. It is clear that there is a significant impact on post-PBC hardness as the forming temperature is raised above 300 °C/s. The post-PBC hardness decreased from 123 to 83 HV, or approximately 32 %, when the forming temperature increased from 300 to 500 °C. The increasing trend of post-PBC hardness was observed between 500 and 535 °C which reaching approximately 76 % of the as-received material. The reason for the sudden and rapid drop is due to the lack of hardening precipitates in the matrix. Moreover, the higher the forming temperature, the larger precipitates and clusters are dissolved and hence the greater loss in hardness. In terms of springback analysis, a reduction in springback angle is expected. This is because the flow stress is decreased with increasing forming temperature which results in decreased elastic deformation, and hence a reduction in springback effect. It is clear to see, the springback behaviour is reduced significantly and eliminated at forming temperatures above 450 °C.

In Figure 4.13 (b), a similar trend was found compared with the results of AA6082, where the lowest post-PBC hardness of 139 HV occurs at a forming temperature of 400 °C. A 10 % recovery of post-PBC hardness was obtain at the forming temperature of 490 °C which is the same as the SHT temperature for AA7075. In terms of springback analysis, the AA7075 U-shaped specimens exhibit a similar decreasing trend with increasing forming temperature, which is contributed with a decrease in flow stress at elevated temperatures resulting in decreased plastic deformation and residual stress. It is clear that the extent of springback decreased significantly as the temperature increased from 200 to 300 °C and was subsequently followed by a linearly drop when the temperature was greater than 300 °C.

Therefore, after evaluating the experimental results for both post-PBC hardness and springback angle, it can be deduced that the FAST process for AA6082 and AA7075 is an effective method to improve post-PBC hardness and minimise the effect of springback. Hence, the optimal forming temperature of 300 °C is suggested for the U-shaped forming of DA-TWBs, which was an adequate compromise between post-PBC hardness and springback.

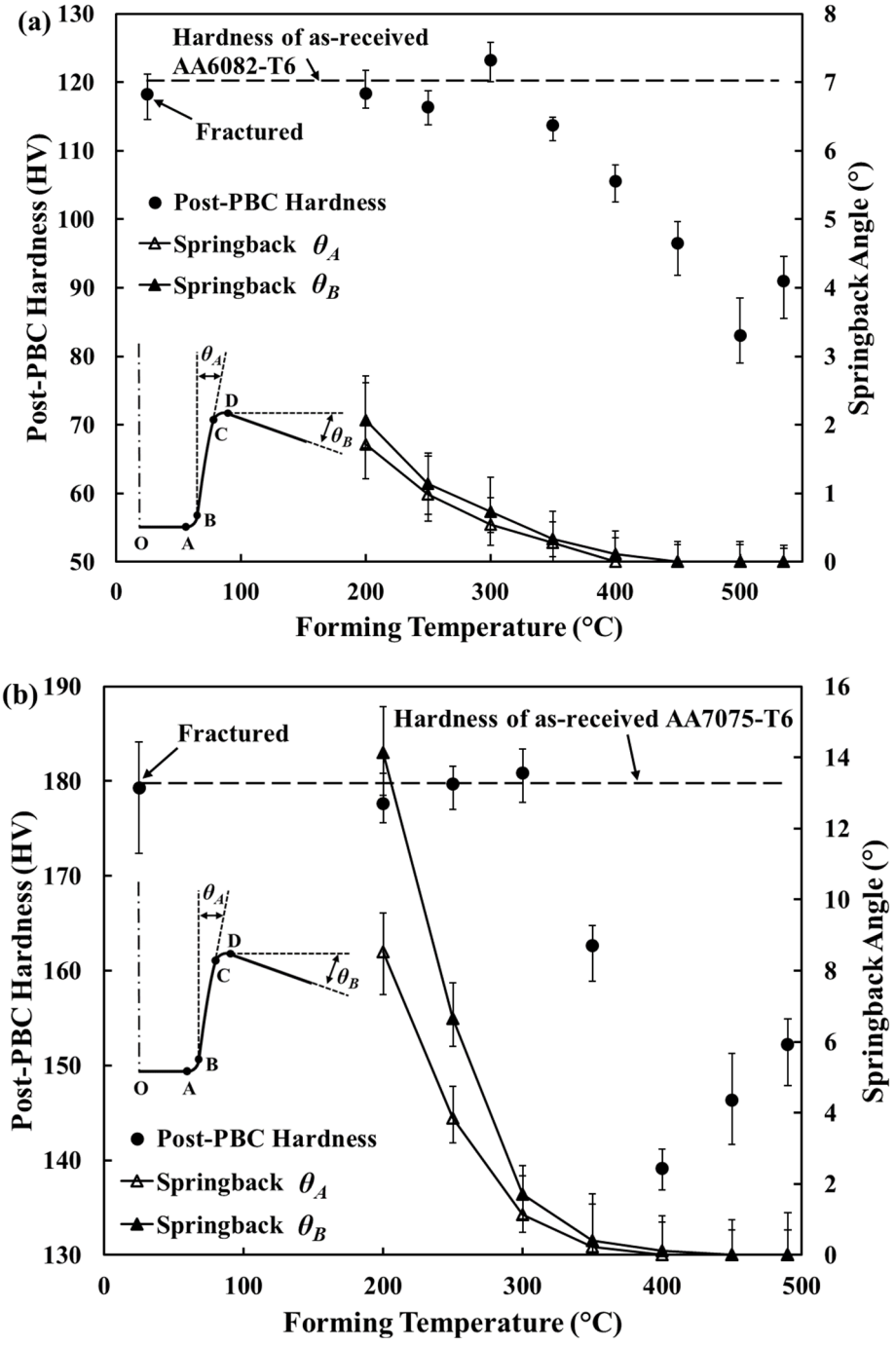

Figure 4.13 Evolution of springback angle and post-PBC hardness of U-shaped component formed at various forming temperatures for (a) AA6082 and (b) AA7075.

4.3.2.2 Effect of forming speed

Figure 4.14 illustrates the effect of forming speed (stamping speed) on post-PBC hardness and springback angle for AA6082 and AA7075 U-shaped components formed by using the FAST process. Error bar shows the highest and lowest post-PBC hardness which were measured from 5 samples for each test condition. Forming speed is directly proportional to the strain rate

experienced by the blank material. Comparing the post-PBC hardness between AA6082 and AA7075 which were formed under different forming speeds, there is no observable effect in the AA6082. The main reason for this is proposed to be the relative low time-sensitivity phase of AA6082 which are only affected at long soaking time (minutes) compared to the small time-scale (seconds) of FAST. In contrast to AA6082, an almost full recovery of post-PBC hardness of 99 % compared with the as-received AA7075 was only observed at forming speeds greater than 200 mm/s. On the other hand, slow forming speeds result in an increased amount of time at the elevated forming temperature as the die needs to travel from its resting position to contacting the blank and starting the cooling process. Slow forming speed leads to lower cooling rate, and slow nucleation and fast growth of coarse precipitates occurs, hence the decrease of hardness.

In terms of springback analysis, θ_A and θ_B were reduced below 0.5 ° at forming speeds greater than 250 mm/s on the U-shaped component of AA6082. Springback in AA7075 shows a similar decreasing trend with increasing forming speed as observed in AA6082, where it is almost negligible at forming speeds of 350 mm/s. Although AA7075 experiences greater springback at lower forming speeds, when comparing to the absolute magnitude of springback reduction, AA7075 again shows an overall significantly greater reduction than AA6082. AA6082 and AA7075 exhibit viscoelastic behaviour at FAST conditions, which results in increased flow stress with increased strain rate and hence an increase in springback is expected due to the increased elastic deformation. This trend has been proven for forming components at low and medium forming speeds (0.5-10 mm/s) (Kim and Koç, 2008). However, decreased springback is an indication of decreased residual stresses and elastic deformation. Even though flow stress is increased, the higher forming speeds also result in greater strain rate hardening. This combined with using room temperature dies (colder than the forming temperature), results in fast cooling of the blank towards the end stages of forming, introducing an increased yielding tension in the blank. Increased tension applied to the blank results in the reduction in bending moment stresses (reduces the stress gradient) and therefore a subsequent observed reduction in springback. These findings are consistent with the result reported by Wang et al (2017). Therefore, the optimal forming speed of 250 mm/s can be suggested for the U-shaped forming of DA-TWBs.

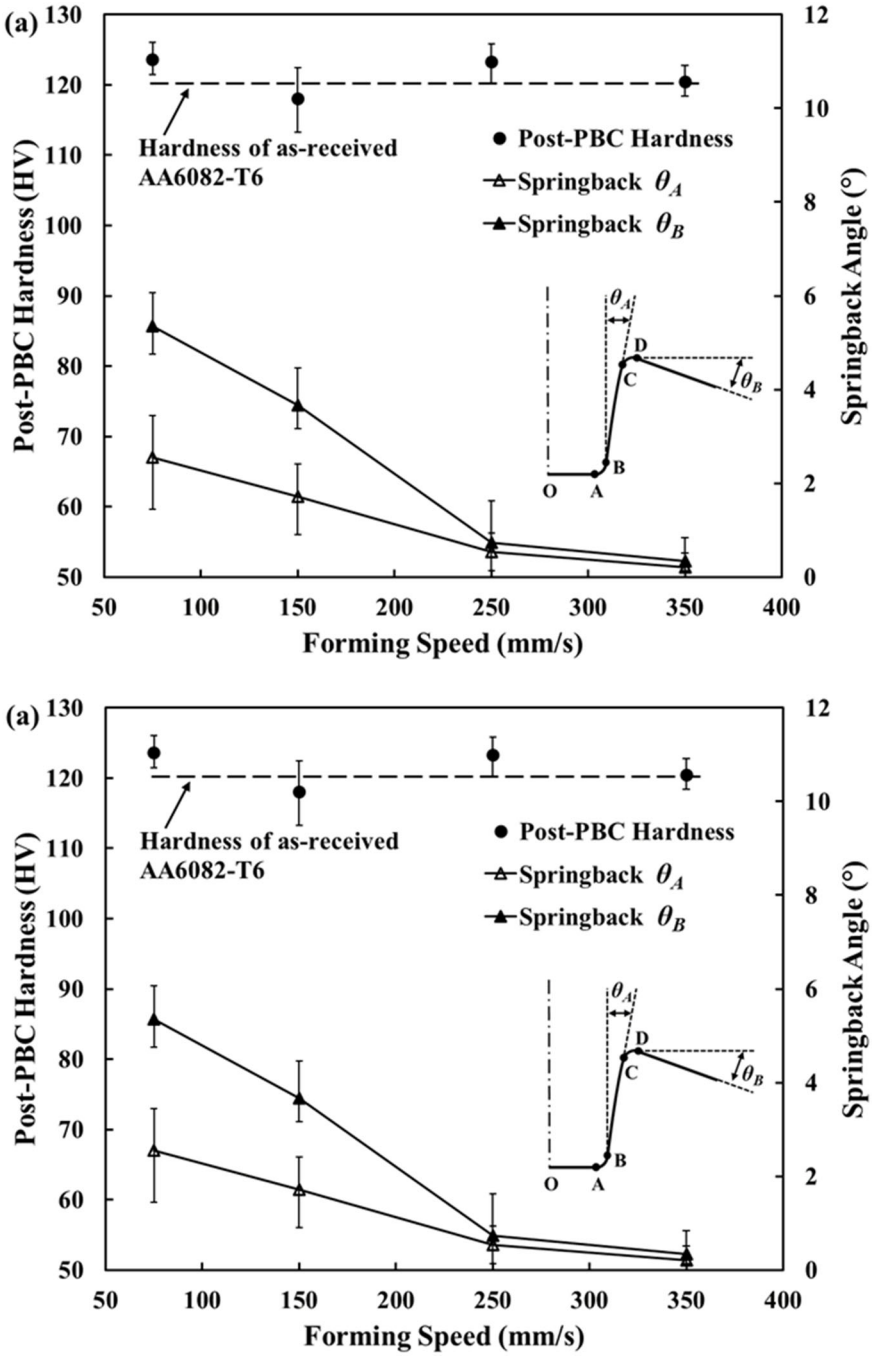

Figure 4.14 Evolution of springback angle of U-shaped component formed at various forming speeds for (a) AA6082 and (b) AA7075.

4.4 Optimal processing window of U-shaped components formed under FAST process

A series of experiments were conducted to investigate the feasibility of the proposed FAST process, including uniaxial tensile testing to investigate the thermal-mechanical properties of

materials, and post-from hardness to evaluate the strength degradation behaviour. U-shaped forming tests were conducted to identify whether the FAST process could minimise the springback effect. Based on these experimental results, the most significant process variables in FAST are the time for material pre-treatment, heating rates, soaking time, forming temperature, forming speed and quenching rate.

Figure 4.15 shows the optimised FAST process to form U-shaped component made with DA-TWBs including pre-treatment and standard paint bake processes. Two base materials AA6082 and AA7075 were pre-aged at the most common artificial ageing temperature and soaked for 60 and 75 minutes for AA6082 and AA7075 respectively. At the beginning of the process, the 'Tx' temper of the material was formed after the pre-treatment process. Friction stir welding was applied to weld the two Tx materials into DA-TWBs. During the forming process, the specimen was formed at the suggested temperature of 300 °C at a heating rate of 50 °C/s with no soaking time, and the forming speed of 250 mm/s, which were proven to provide superior strength-ductility-springback combined behaviour. The fast heating rate and forming speed is preferred for FAST as it is not only beneficial for post-PBC hardness and ductility but also increases the production rate with low cycle times. Therefore, the optimal processing window for FAST of the AA6082 and AA7075 materials for DA-TWBs is summarised in Table 4.2.

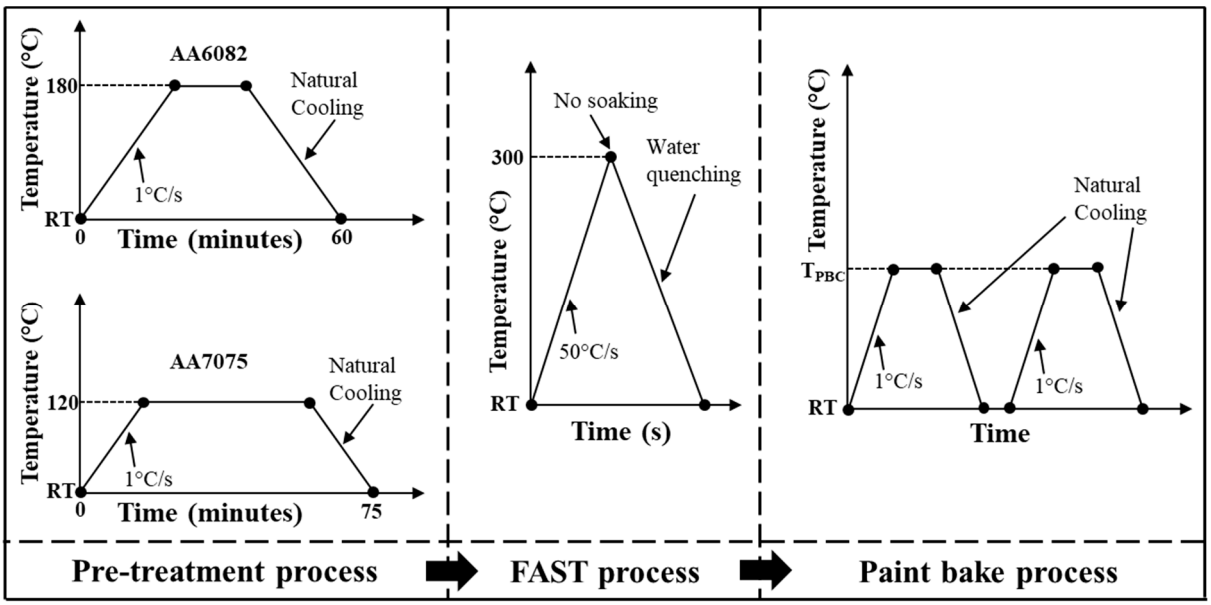

Figure 4.15 Schematic diagram of optimised FAST processes to form the DA-TWBs.

Table 4.2 Optimal processing window of DA-TWBs for the FAST process.

Processing parameters / Material	Pre-treatment temperature	Pre-treatment time	Heating rate	Soaking time	Forming temperature	Forming Speed
AA6082	180 °C	60 minutes	≥ 50 °C/s	No	250 ~ 350 °C & ≥ 450 °C	≥ 250 mm/s
AA7075	120 °C	75 minutes				

4.5 Implementation of the optimised FAST process to form U-Shaped components made from DA-TWBs

In this section, FAST is proposed for manufacturing the U-shaped component by using DA-TWBs. Conventionally, automotive manufacturers form the part with individual materials that are subsequently welded together which is time-consuming. FAST of DA-TWBs aims to reduce the processing time by welding the two base materials together then forming in a single process, which not only enhances the strength of the components but also improves the production rate. Therefore, a demonstration forming trial of FAST by using DA-TWBs was performed with the optimal processing window, which was developed through the experimental work. The overall mechanical properties and quality of the formed component were evaluated by investigating the springback angle, post-PBC hardness and thickness distribution. In addition, the detailed FE-simulation of FAST forming of a DA-TWBs U-shaped part is presented in the Appendix.

4.5.1 Material and forming test preparation of DA-TWBs

Two dissimilar aluminium alloys, AA6082 and AA7075 with a thickness of 2 mm supplied by Smiths Metal Centres Limited, were pre-treated and friction stir welded by The Welding Institute Limited as raw blanks to form U-shaped panel components under the optimal FAST forming conditions. Figure 4.16 (b) shows the specimen design of the DA-TWBs for a U-

shaped component, with a length of 240 mm and width of 84 mm. The blank was water-jet cut from the original friction stir welded blank as shown in Figure 4.16 (a).

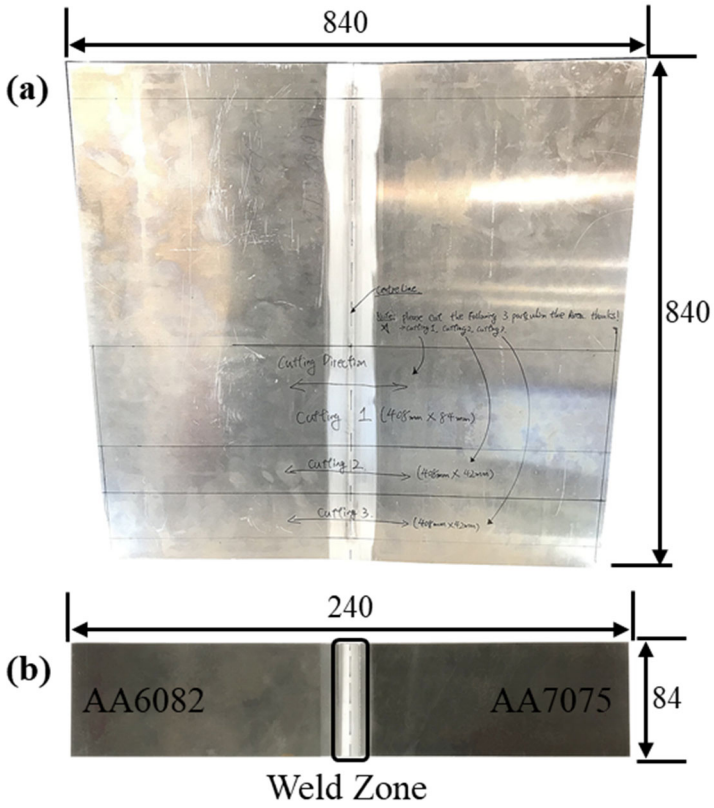

Figure 4.16 Material preparation of DA-TWBs (a) original dissimilar alloy tailor welded blanks and (b) design of blank for U-shaped forming (dimensions are in mm).

In order to validate the feasibility of the proposed FAST process for U-Shaped DA-TWBs, forming tests were performed through the dedicated pilot production line *"Uni-Form"*, where the DA-TWBs were placed in between the die and punch. The automated conveyor moved the specimen into the forming station, and the powerful contact heater was then closed to heat the blank to target forming temperature of 300 °C at a designed heating rate of 50 °C/s. Once heating was completed, the hot blank was then immediately transferred back to the forming station. In the meantime, the stroke of the hydraulic press machine was activated and provided a forming speed of 250 mm/s to form and quench the hot DA-TWBs. Finally, the formed component was heated at the proprietary paint bake cycles which were provided by the automotive OEM sponsor, which are not presented in this thesis due to a confidentiality agreement. The detailed optimised FAST processing parameters are shown in Table 4.3, and Figure 4.17 illustrates the schematic diagram for initial and post-form stages.

Table 4.3 Optimised FAST processing window for U-shaped of DA-TWBs.

Processing Parameters	Heating Rate	Forming Temperature	Forming Speed	Quenching Source	Total Cycle Time
Values	50 °C/s	300 °C	250 mm/s	Cold Die	12.5 Spm

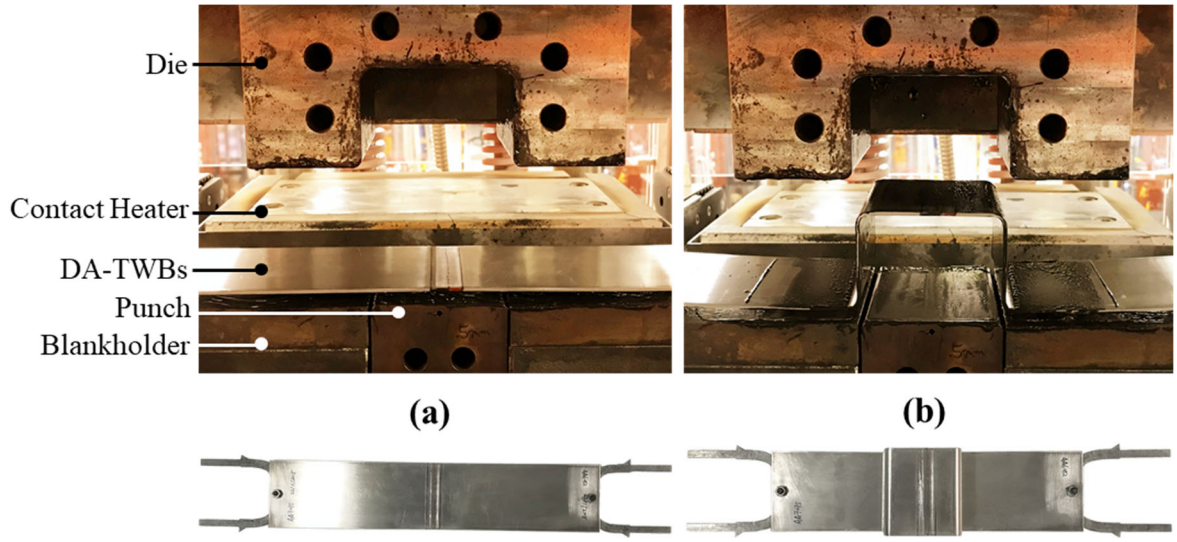

Figure 4.17 Schematic diagram of forming test (a) initial stage and (b) post-formed stage.

4.5.2 Post-PBC properties evaluation of U-shaped DA-TWBs

In this study, forming trials of optimised forming process parameters were successfully performed via the "UniForm" platform. A U-shaped DA-TWBs with good surface quality was formed at 300 °C as shown in Figure 4.18. The measurement of the springback angle indicated that good forming accuracy was achieved as all the springback angles were less than 1.8°, which is shown in Figure 4.18 (c). However, it is clear that the weld zone was a shift towards the AA6082 side, where the difference of failure strain between the two materials can explain the observation. As AA7075 has a greater ductility than AA6082 at a temperature of 300 °C according to the previous studies, more AA7075 material can be drawn into the tool.

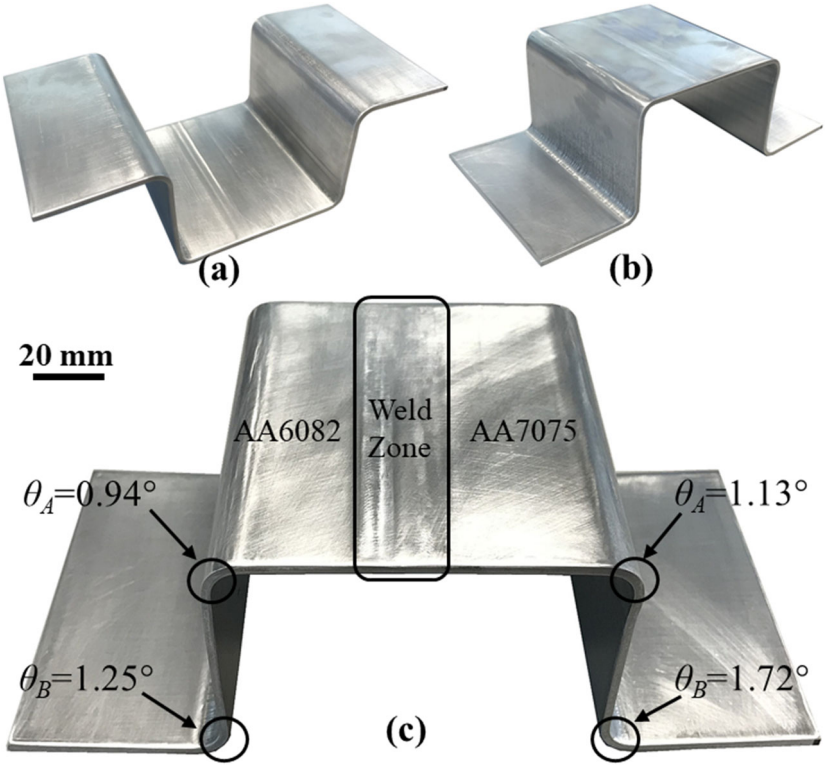

Figure 4.18 Schematic diagram of formed component (a) isometric view (b) reverse view and (c) front view with springback angles.

The post-PBC hardness of U-shaped DA-TWBs was measured along the cross-section by using the hardness tester under the load of HV5. Figure 4.19 shows the post-PBC hardness was evenly distributed and with a clear identification of the regions of AA6082, weld zone and AA7075. By comparing with the hardness of as-received material, the post-PBC hardness recovery that can be achieved is approximately 98 % and 97 % for the AA6082 and AA7075 materials, respectively. Figure 4.20 illustrates the thickness distribution along the cross-section of the formed part, and good achievement was made by using the FAST process with only 4% reduction on the sidewall of the U-shaped part, where the most deformation and thinning occurred. Therefore, a U-shaped component made with DA-TWBs was successfully formed by using the proposed forming process to the required post-PBC hardness and springback angles. In addition, the successful implementation may lead to a game change in the forming of DA-TWBs, which offers the potential to not only increase the production rate but also increase energy savings compared with conventional forming techniques and processes.

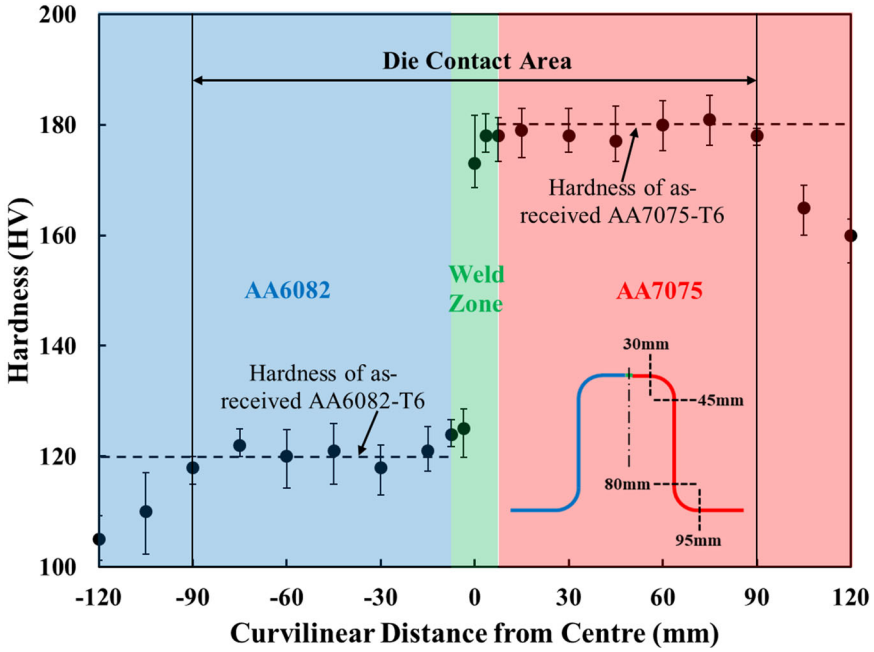

Figure 4.19 Post-PBC hardness distribution of U-shaped component of DA-TWBs.

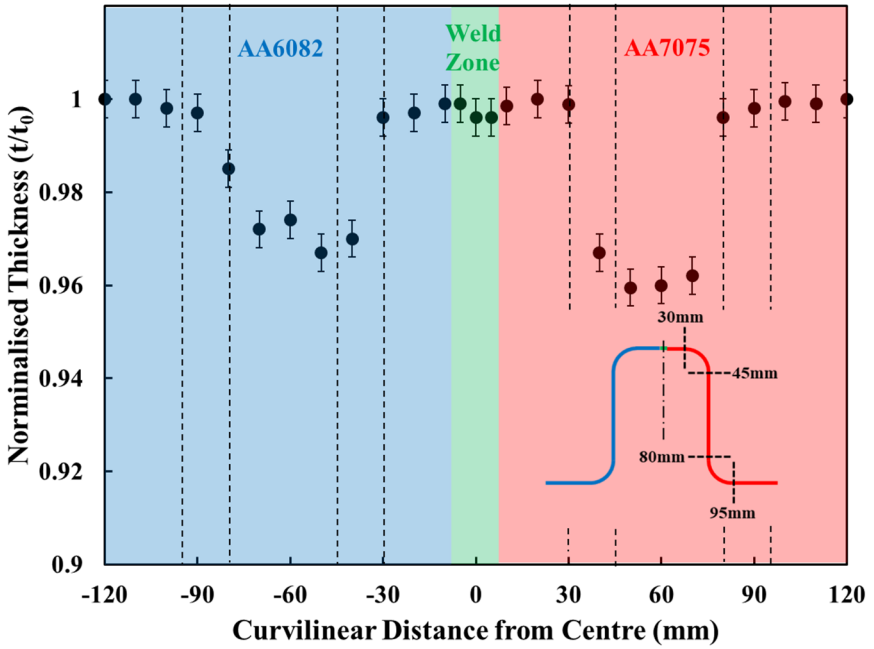

Figure 4.20 Thickness distribution of U-shaped component formed of DA-TWBs.

4.6 Summary

In this chapter, the flow behaviour and ductility (failure strain) of the AA6082 and AA7075 have been investigated by uniaxial tensile testing under different forming temperatures and strain rates. In AA6082, the ductility was improved as the temperature increased from 300 to 535 °C. Moreover, the failure strain increased from 0.7 to 0.95 as the strain rate increased from

0.1 to 5 s^{-1}. In AA7075, the ductility increased with temperature rising until reaching 425 °C, and then a decreasing trend was found at a temperature above 425 °C. In addition, the failure strain decreased from 0.7 to 0.45 when strain rate increased from 0.1 to 5 s^{-1}.

The effect of pre-treatment time, heating rate, soaking time, forming temperature and quenching source on the post-PBC hardness of the AA6082 and AA7075 were investigated. A high heating rate above 50 °C/s was suggested in order to avoid precipitation transformation and hence reduce the amount of coarse precipitates. No soaking action was suggested in the FAST process as the generation of metastable precipitates occurred with soaking, which leads to reduced post-PBC hardness. A forming temperature of 300 °C was suggested as higher temperatures will cause unrecoverable post-PBC hardness. Finally, there was a 5 % difference of post-PBC hardness for the specimen between die and water quenched. Therefore, a fast quenching rate was suggested to minimise or eliminate the precipitation coarsening.

U-shaped forming tests under different FAST conditions were successfully conducted through the "UniForm" platform, including different forming temperatures and forming speeds. A reduction of springback from 2 ° and 14 ° to 0.6 ° and 2 ° with increasing forming temperature can be confirmed in AA6082 and AA7075, respectively. This was due to a decrease in flow stress and hence reduced plastic deformation. The springback study also shows that by using forming speeds greater than 250mm/s, springback can be reduced to below 0.73 ° in AA6082 and 1.72 ° in AA7075, which is due to increased flow stress with increased strain rate and hence an increase in springback.

The optimal processing window for FAST of the AA6082, AA7075 and DA-TWBs was suggested to be a forming range of 250 – 350 °C with a heating rate greater than 50 °C/s and no required soaking time, which can provide the best combination of strength, ductility and springback.

A novel FAST processing route has been successfully implemented for forming of U-Shaped components by using DA-WTBs. Springback angles were lower than 2 ° and post-PBC hardness reached 97 % of the as-received hardness, which validated the feasibility of using the FAST process. In addition, the FAST has enabled a significant reduction of total cycle time from hours to 10 seconds, which further improved the production rate to 12.5 spm.

Chapter 5. Development of a general IHTC model to characterise the critical processing parameters in FAST processes

In this chapter, a general aluminium alloy-independent model with a single set of calibration constants was developed to enable the prediction of IHTC evolutions as a function of critical parameters including contact pressure, surface roughness, initial blank temperature, initial blank thickness, tool material, coating material and lubricant. Subsequently, the predicted IHTC evolutions for 6082 and 7075 aluminium alloys were applied to simulate the material temperature evolutions during FAST forming processes, which were then integrated with the respective CCP diagrams to identify the critical processing parameters in order to obtain the desired post-PBC strength of the aluminium alloys. Dissimilar alloy panel components were formed under the FAST forming conditions with the measurement of the post-PBC hardness to verify the developed IHTC model, the predicted IHTC evolution and the determined critical processing parameters. The structure of this chapter is shown in Figure 5.1.

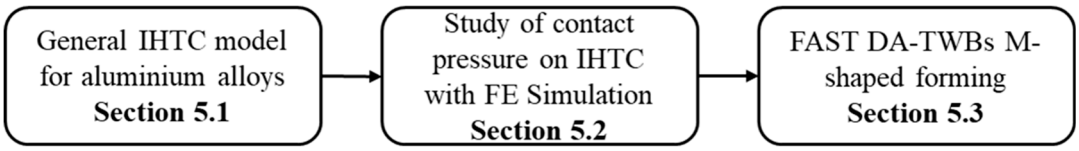

Figure 5.1 Schematic diagram of the major sections addressed in Chapter 5.

The test facility developed and performed in Chapter 5 lead to the publication of patent: "Cai, Z., Liu, X., Dhawan, S., Fakir, O. El., Lin, J., Wang, L., 2019. A Compact Automatic Simulating Facility for Non-Isothermal Forming Processes. Patent application number: CN201911035650.9."

Chapter 5 is based on the peer reviewed publication "Liu, X., Cai, Z., Zheng, Y., Fakir, O. EL., Wang, L., 2020. Development of a general interfacial heat transfer coefficient model to characterise the critical processing parameters in hot and warm aluminium stamping processes. Applied Thermal Engineering, (in press):115619-115645."

5.1 A general IHTC model for aluminium alloy

A general interfacial heat transfer coefficient model was developed to predict the IHTC evolutions for different aluminium alloys as a function of contact pressure, initial blank temperature, initial blank thickness, surface roughness, tool material, lubricant material and coating material, which are the most important factors influencing the IHTC. Based on previous research, the heat transfer between two contacting solids in a hot/warm stamping process mainly depends on four mediums, namely air, metallic solid, lubricant and tool coating. Therefore, the general IHTC model was developed as a sum of the dominant heat transfer mechanisms as a result of these four mediums, as shown in Equation (5.1.1):

$$h = h_a + h_s + h_l + h_c \tag{5.1.1}$$

where h is the overall IHTC, h_a is the air-contact IHTC, h_s is the solid-contact IHTC, h_l is the lubricant-contact IHTC, and h_c is the coating-contact IHTC. Due to the asperities on two contacting surfaces, a large amount of vacancies exist at the interface when a blank contacts the forming tools. Consequently, the heat transfer across the air gap becomes the dominant mechanism when a contact pressure, lubricant or tool coating is not applied between the blank and forming tools. However, this is negligible compared to the amount of heat transfer generated by the application of contact pressure, lubricant and tool coating. Therefore, the air-contact IHTC h_a is assumed as a constant value, determined by previous experimental results at a contact pressure of 0 MPa under dry and uncoated conditions.

When a contact pressure is applied between the blank and forming tools, the heat transfer between the two metallic solids dominates. The factors influencing the interfacial conditions, e.g. initial blank temperature, tool material, surface roughness and contact pressure, also affect the solid-contact IHTC h_s, which is characterised as Equation (5.1.2):

$$h_s = \alpha \frac{K_{st}}{R_{st}} N_p L \tag{5.1.2}$$

where α is the temperature dependent thermal diffusivity of the blank, L is a blank thickness dependent parameter, K_{st} is the harmonic mean thermal conductivity of the interface between the blank and forming tools, R_{st} is the interfacial surface roughness, and N_P is a contact pressure dependent parameter. It has been proven that the positive linear effect of initial blank

temperature on the IHTC is composed of two mechanisms, i.e. the effects of thermal properties and material strength of the aluminium alloy (Liu et al., 2019a). The IHTC increases with increasing thermal properties of the blank due to its improved heat transfer capability at a higher initial blank temperature. The positive effect of thermal properties of the blank on the IHTC was identified by the temperature dependent thermal diffusivity α (Salazar, 2003), as shown in Equation (5.1.3):

$$\alpha = B(T)\frac{k_s(T)}{\rho(T)c_p(T)} \tag{5.1.3}$$

where $B(T)$ is a temperature dependent parameter and modelled by Equation (5.1.4) using the Arrhenius equation (Mohamed et al., 2012). $k_s(T)$, $\rho(T)$ and $c_p(T)$ are the thermal conductivity, density and specific heat capacity of the aluminium alloy at the target initial blank temperature respectively.

$$B(T) = b_0 \exp\left(\frac{Q_b}{RT}\right) \tag{5.1.4}$$

where R is the molar gas constant, T is the absolute temperature in Kelvin, b_0 and Q_b are model constants. Therefore, the temperature dependent thermal diffusivity α is able to accurately describe the comprehensive material thermal properties for characterising the rate of heat transfer under different initial blank temperature conditions. The effect of material strength of the aluminium blank on the IHTC was integrated into the contact pressure dependent parameter N_P, as shown in Equation (5.1.5):

$$N_p = 1 - \exp\left(-\lambda f \frac{P}{\sigma_U}\right) \tag{5.1.5}$$

where λ is a model constant, f is a tempering correction factor, P is the contact pressure between the blank and forming tools, and σ_U is the temperature dependent ultimate strength of the blank. Due to the asperities on the contacting surfaces, the real contact area between the blank and forming tools is much less than the apparent contact area. When an aluminium blank is heated to elevated temperatures, its strength is much lower than that of the steel tools at room temperature. Consequently, the asperities on the blank contact surface are deformed by the forming tools at a defined contact pressure during compression, leading to a larger real contact area and thus IHTC value. When the contact pressure reaches its convergent value, the real contact area approaches the apparent contact area and reaches its peak value, leading to a

plateau of the IHTC. It was found that the ratio of the real contact area to the apparent contact area is equivalent to the ratio of the contact pressure to the ultimate strength of the aluminium blank (Merrill L. Minces., 1966). Meanwhile, a logarithmic increasing trend of the real contact area as a function of contact pressure was identified (Buchner et al., 2009). Therefore, the contact pressure dependent parameter N_P and thus the solid-contact IHTC h_s logarithmically increase with increasing ratio of the contact pressure P to the ultimate strength of the aluminium blank σ_U .

As mentioned before, the material strength of the aluminium blank is an additional functional mechanism on the effect of initial blank temperature on the IHTC, and it decreases with increasing initial blank temperature. As a result, an increased number of asperities on the blank contact surface are deformed at a higher initial blank temperature, leading to a larger real contact area and thus IHTC value. Hence, the material strength of the blank negatively influences the IHTC, and its temperature dependence is modelled as Equation (5.1.6) using the Arrhenius equation (Li et al., 2013).

$$\sigma_U = \sigma_0 \exp\left(\frac{Q_\sigma}{RT}\right) \tag{5.1.6}$$

where σ_0 and Q_σ are model constants, determined through the uniaxial tensile tests at elevated temperatures. The ultimate strength of the material greatly depends on tempering. The tempering correction factor f is therefore applied to enable the contact pressure dependent parameter N_P to predict the deformation mechanism on different tempered alloys, as shown in Equation (5.1.7), where $\sigma_U(Tx)$ and $\sigma_U(T6)$ are the ultimate strength of the aluminium alloy under the present tempering conditions and the T6 conditions respectively.

$$f = \frac{\sigma_U(Tx)}{\sigma_U(T6)} \tag{5.1.7}$$

The amount of heat transfer increases with increasing thermal conductivities of the two contacting solids, leading to larger IHTC values. The harmonic thermal conductivity of the interface between the blank and forming tools K_{st} was therefore applied to describe the capability of the interface to conduct heat, as shown in Equation (5.1.8):

$$K_{st} = \frac{2}{k_s^{-1} + k_t^{-1}} \tag{5.1.8}$$

where k_s and k_t are the thermal conductivities of the aluminium blank (specimen) and forming tools at their initial (forming) temperatures. In contrast, the IHTC decreases with increasing surface roughness of the blank and forming tools due to the decreasing real contact area. The negative effect of surface roughness on the IHTC is modelled as Equation (5.1.9):

$$R_{st} = sin\theta\sqrt{R_s^2 + R_t^2} \tag{5.1.9}$$

where R_s and R_t are the initial surface roughness of the contact surfaces of the aluminium blank (specimen) and forming tools respectively. The root mean square value could describe the roughness condition at the interface. Additionally, θ is the initial deformation angle of the blank contact profile, and thus $\sin\theta$ is the mean modulus of the slope of the blank contact profile (Cooper et al., 1969). The deformation of the blank by the forming tools has two forms. When R_s is smaller than R_t, the forming tools coarsen the surface profile of the blank to increasingly mesh the contacting surfaces, thus leading to a larger real contact area; when R_s is larger than R_t, the forming tools smoothen the surface profile of the blank, resulting in a similar consequence, i.e. a larger real contact area. However, the initial deformation angle θ is different under these two forms, which is assumed as 20° when R_s is smaller than R_t, and 70° when R_s is larger than R_t. Therefore, the interfacial surface roughness R_{st} represents the initial roughness and deformation conditions at the interface.

In the hot and warm stamping industry, blanks with different thicknesses are applied to satisfy the desired requirements. Although the interfacial conditions are independent of the blank thickness, more internal thermal energy is stored in a thicker blank, which could compensate for the heat loss at the interface. Therefore, an engineering IHTC able to define the effect of blank thickness can be used in the FE simulation to accurately predict the temperature field, while the true IHTC is not changed. The blank thickness parameter L is able to describe its positive effect on the IHTC and modelled as Equation (5.1.10), where l is the blank thickness, m and n are model constants.

$$L = m \cdot \ln(l) + n \tag{5.1.10}$$

Lubricants are widely applied in hot and warm stamping processes to increase the drawability of the blank material and simultaneously decrease the wear of the forming tools. Due to its importance, the lubricant-contact IHTC h_l is developed as Equation (5.1.11):

$$h_1 = \omega \frac{K_{slt}}{R_{st}} N_\delta \tag{5.1.11}$$

where ω is a model constant, K_{slt} is the harmonic mean thermal conductivity of the interface between the blank, forming tools and lubricant, and N_δ is a lubricant layer thickness dependent parameter.

$$K_{slt} = \frac{3}{k_s^{-1} + k_l^{-1} + k_t^{-1}} \tag{5.1.12}$$

where k_l is the thermal conductivity of the lubricant. When a lubricant is applied onto the contact surfaces, the vacancies between the blank and forming tools are filled by the lubricant, instead of air. Consequently, the heat transfer mediums are the two contacting solids and the lubricant. Therefore, the equivalent thermal conductivity of the blank, forming tools and lubricant K_{slt} is more accurate to define the capability of the interface to conduct heat under the lubricated conditions. Meanwhile, the surface roughness conditions at the interface are not changed by the application of the lubricant, and thus the interfacial surface roughness R_{st} is maintained.

It was found that the IHTC increases with increasing lubricant layer thickness, as a result of more vacancies at the interface being filled by the lubricant and thus a larger amount of heat transfer occurring. However, when the lubricant layer thickness reaches a convergent value, the vacancies are fully filled, and the excessive lubricant is squeezed out of the interface. Consequently, the increasing lubricant layer thickness does not affect the IHTC any longer. Therefore, the lubricant layer thickness dependent parameter N_δ and thus the lubricant-contact IHTC h_l have a logarithmically increasing relationship with the lubricant layer thickness δ_l, as shown in Equation (5.1.13), where γ is a model parameter.

$$N_\delta = 1 - \exp(-\gamma \delta_l) \tag{5.1.13}$$

Due to the excellent oxidation, corrosion and wear resistance, tool coatings have been widely applied in the hot and warm aluminium stamping processes. As opposed to lubricants being an independent heat transfer medium between the blank and forming tools, tool coatings are stably deposited onto the contact surfaces of the forming tools as another medium. Therefore, the heat

transfer mechanism on the lubricant-contact IHTC h_l is different from that on the coating-contact IHTC h_c, which is modelled as Equation (5.1.14):

$$h_c = \beta \frac{k_s}{A} tan\theta \cdot \ln\left(\frac{k_c}{k_l}\right) \delta_c \cdot N_p \tag{5.1.14}$$

where β is a model parameter, k_c is the thermal conductivity of the tool coating, δ_c is the tool coating layer thickness, and A is the apparent contact area between the blank and forming tools. Because the heat transfers from the hot blank to the cold coated tools through the contact area, the coating-contact IHTC h_c is determined by three terms. The first term of $k_s \tan\theta / A$ represents the thermal energy at the high potential (hot blank) to conduct heat, the second term of $\ln(k_c / k_l)\delta_c$ represents the thermal energy at the low potential (cold coated tools) to transfer heat, and the third term N_P determines the pressure dependent driving force from the high to low potential. Furthermore, the second term of $\ln(k_c / k_l)\delta_c$ describes the thermal performance of the tool coating and the integrated effects of coated tools on the IHTC. A positive term value indicates that a tool coating with a thermal conductivity higher than that of the substrate is applied and thus the heat transfer is enhanced, contributing to a larger IHTC value; while a negative term value indicates that a tool coating with a thermal conductivity lower than that of the substrate is applied and thus the heat transfer is reduced, contributing to a smaller IHTC value. The effect of tool coating on the IHTC, either positive or negative, increases with increasing absolute value of this term. Therefore, the term of $\ln(k_c / k_l)\delta_c$ indicates that the thermal conductivity and layer thickness of the tool coating determine its effect on the IHTC.

Table 5.1 The IHTC model constants.

Parameter	b_0 (s/m^2)	Q_b (J/mol)	R (J/molK)	λ (-)	m (-)
Value	1.69	-1730	8.314	5	0.64
Parameter	n (-)	ω (-)	γ (m^{-1})	β (-)	A (m^2)
Value	0.56	4.2e-5	1.5e5	8.3e3	5e-4

Therefore, Equations. (5.1.1-5.1.14) comprise the general model to predict IHTC evolutions for different aluminium alloys as a function of contact pressure, initial blank temperature, initial blank thickness, tool material, surface roughness, lubricant and tool coating. Except for the parameters requiring experimental measurements, e.g. surface roughness, ultimate strength,

thermal conductivity and lubricant/coating layer thickness, the remaining model constants are independent of aluminium alloy grade, as shown in Table 5.1, which significantly simplifies the model and enhances its flexibility for a wide range of aluminium alloys. Figure 5.2 shows the experimental IHTC results under different conditions determined from the literature (Liu et al., 2019a, Liu et al., 2019b, Liu et al., 2018b, Liu et al., 2017c) and the predicted IHTC evolutions obtained from the developed model using the actual measured parameters from those works. Error bar shows the highest and lowest post-PBC hardness which were measured from 5 samples for each test condition. The close agreement between the experimental and predicted IHTC results demonstrate the accuracy of the developed model. In order to be compatible with commercial FE software, the IHTC evolutions were always assigned as a function of contact pressure.

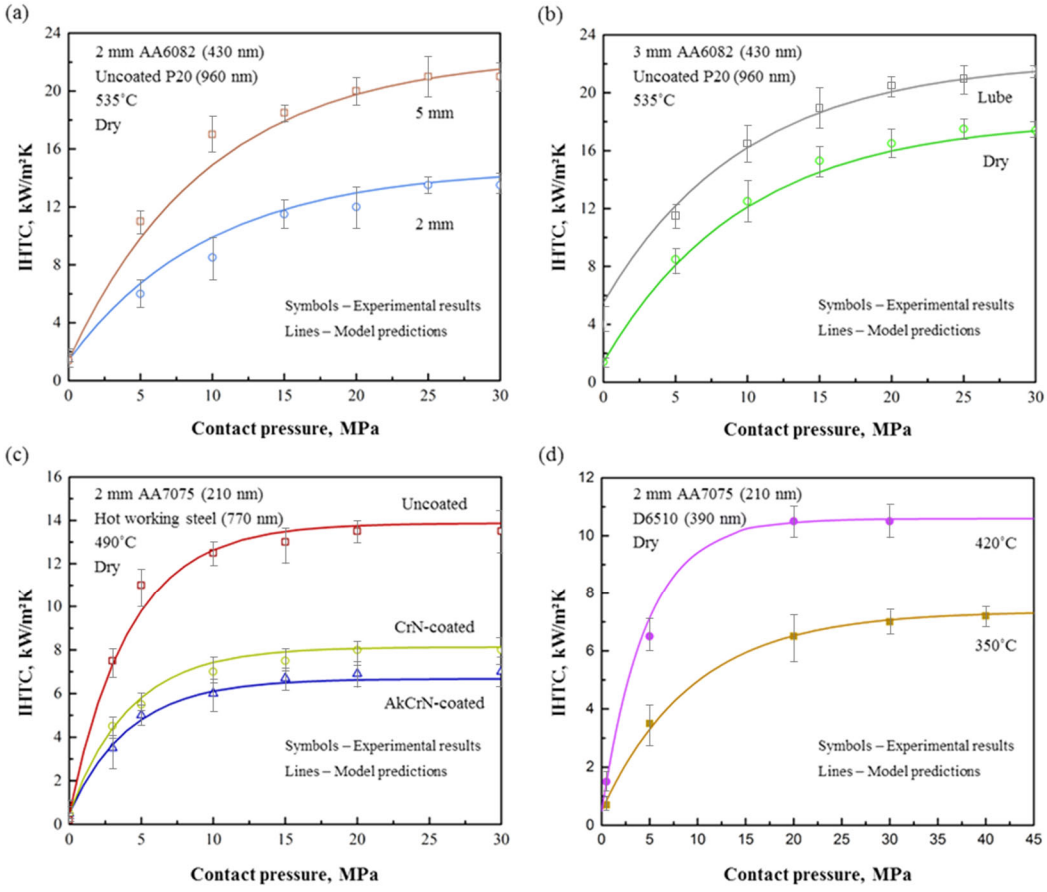

Figure 5.2 The comparisons between the experimental and predicted IHTC results for (a) AA6082 with 2 and 5 mm thicknesses under dry conditions at 535 ˚C when using uncoated P20 tools; (b) AA6082 with 3 mm thickness under lubricated and dry conditions at 535 ˚C when using uncoated P20 tools; (c) AA7075 with 2 mm thickness under dry conditions at 490 ˚C when using uncoated, CrN and AlCrN-coated tools; and (d) AA7075 with 2 mm thickness under dry conditions at 420 ˚C and 350 ˚C when using WC-coated tools.

Figure 5.3 shows the IHTC evolutions as a function of other influential factors, e.g. initial blank temperature, initial blank thickness and thermal conductivities of tool and coating, to highlight their individual effects on the IHTC.

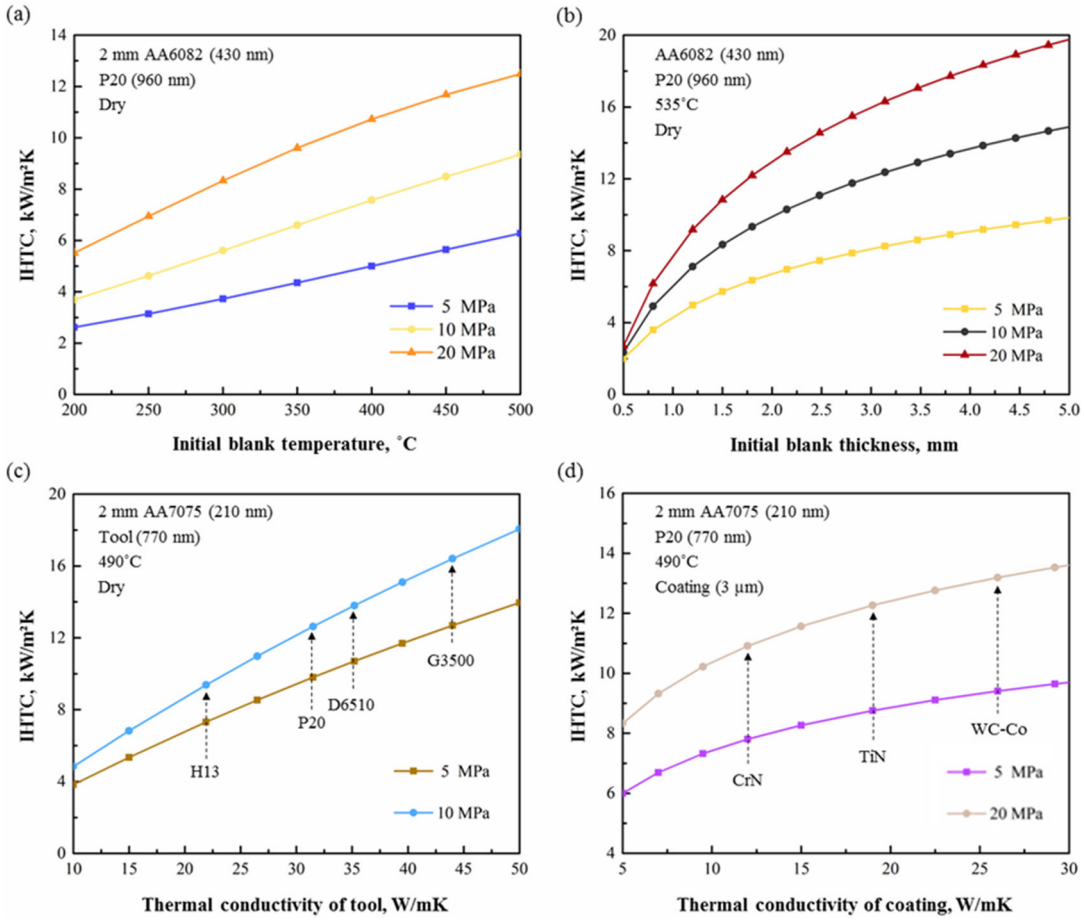

Figure 5.3 The predicted IHTC evolutions as a function of (a) initial blank temperature; (b) initial blank thickness; (c) thermal conductivity of tool; and (d) thermal conductivity of coating.

5.2 Critical processing parameters in FAST processes

As mentioned previously, the IHTC evolution predicted by the developed model can be implemented in FE simulations of hot and warm stamping processes to simulate the temperature evolutions of aluminium alloys, which are then compared with the CCP diagrams to identify whether the critical cooling rate and IHTC have been achieved. Therefore, the critical processing parameters can be optimised to meet the desired requirements through the integration of the FE simulations with the CCP diagrams. The present research identified the critical contact pressure for AA6082 and AA7075 under the FAST forming conditions as one

of the most important processing parameters. The same method can be applied to determine additional other processing parameters via the *Smart Forming*® platform, such as appropriate forming temperature and soaking time (Smart Forming, 2020).

5.2.1 FE simulation setup to identify the critical contact pressure

In order to identify the critical contact pressure in FAST forming of aluminium alloys, a FE model was created in PAM-STAMP software to simulate the heat transfer between a hot aluminium blank and cold tools, and subsequently obtain their temperature evolutions. This model was composed of seven components; an aluminium blank, two symmetrical blankholders, two symmetrical screws, and a symmetrical punch and die pair, which were made from P20 tool steel, as shown in Figure 5.4 (a). Quadrangle thermal shell elements with a size of 1 × 1 mm^2 were used for the blank, while the same elements with a size of 2 × 2 mm^2 were used for all other components. The heating process was not simulated, and thus the initial temperatures for the aluminium blank and other components were assigned as the target heating temperature and room temperature respectively. In addition, all six degrees of freedom for the aluminium blank were defined as free, those for the die were restricted, and only freedom in the z-direction was free for the punch, blankholders and screws.

A ‘hot forming validation double action’ strategy was applied in the FE simulation, in which the aluminium blank was first freely located onto the two blankholders and then fixed by the two screws. Subsequently, the punch rapidly moved towards the blank along the moving direction (z-direction) and compressed against the die at a pre-defined contact pressure. The temperature evolutions of the blank during compression of 5 seconds were measured and exported. In order to identify the critical contact pressure, the IHTC evolution as a function of contact pressure with the restriction of other processing parameters, e.g. heating temperature (initial blank temperature), soaking time and tool materials, was implemented in the FE simulation. Therefore, the heat transfer between the hot aluminium blank and cold forming tools occurred at the IHTC value corresponding to the pre-defined contact pressure. In the present research, when a P20 steel was used for the forming tools, the IHTC evolutions for 6082 and 7075 aluminium alloys as a function of contact pressure under the FAST forming conditions were predicted by the developed general IHTC model and then implemented in the FE simulations, as shown in Figure 5.4 (b).

The developed FE model enables the symmetrical heat transfer between the hot blank and cold tools as well as the homogeneous distribution of the contact pressure on the contact area of the

aluminium blank. In addition to the contact pressure, other processing parameters were also assigned in the FE model to describe their effects on the temperature evolutions of the blank and further determine their critical values.

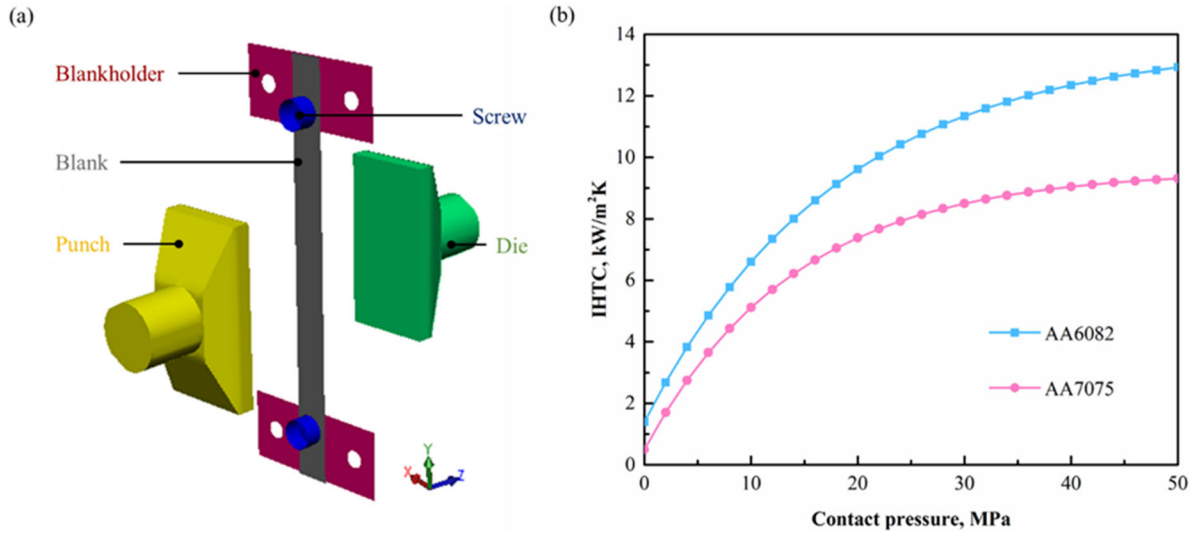

Figure 5.4 (a) The FE model in PAM-STAMP to determine the critical processing parameters; (b) The predicted IHTC evolutions for AA6082 and AA7075 as a function of contact pressure under the FAST forming conditions.

5.2.2 Integration of the FE simulated results with the CCP diagrams

After the FE simulations, the temperature evolutions of all elements on the aluminium blank were exported and then compared with the CCP diagrams for AA6082 and AA7075, which were characterised in the studies of (Milkereit et al., 2018, Milkereit et al., 2012). A filter was then applied to distinguish 'safe' elements from the entire aluminium blank. The elements, of which the temperature evolutions did not intersect the CCP diagram, and thus the post-PBC strength could be fully retained, were defined as 'safe' elements and shown as green colour; otherwise, they were defined as 'fail' elements and shown as red colour. It has been proven that the IHTC and cooling rate of the aluminium alloy increase with increasing contact pressure, consequently leading to the increased number of 'safe' elements. Regarding the contact area on the AA6082 blank, all elements were 'safe' when the contact pressure was larger than 18 MPa, as shown in Figure 5.5 (a). This indicated that the critical contact pressure for AA6082 is 18 MPa under the FAST forming conditions.

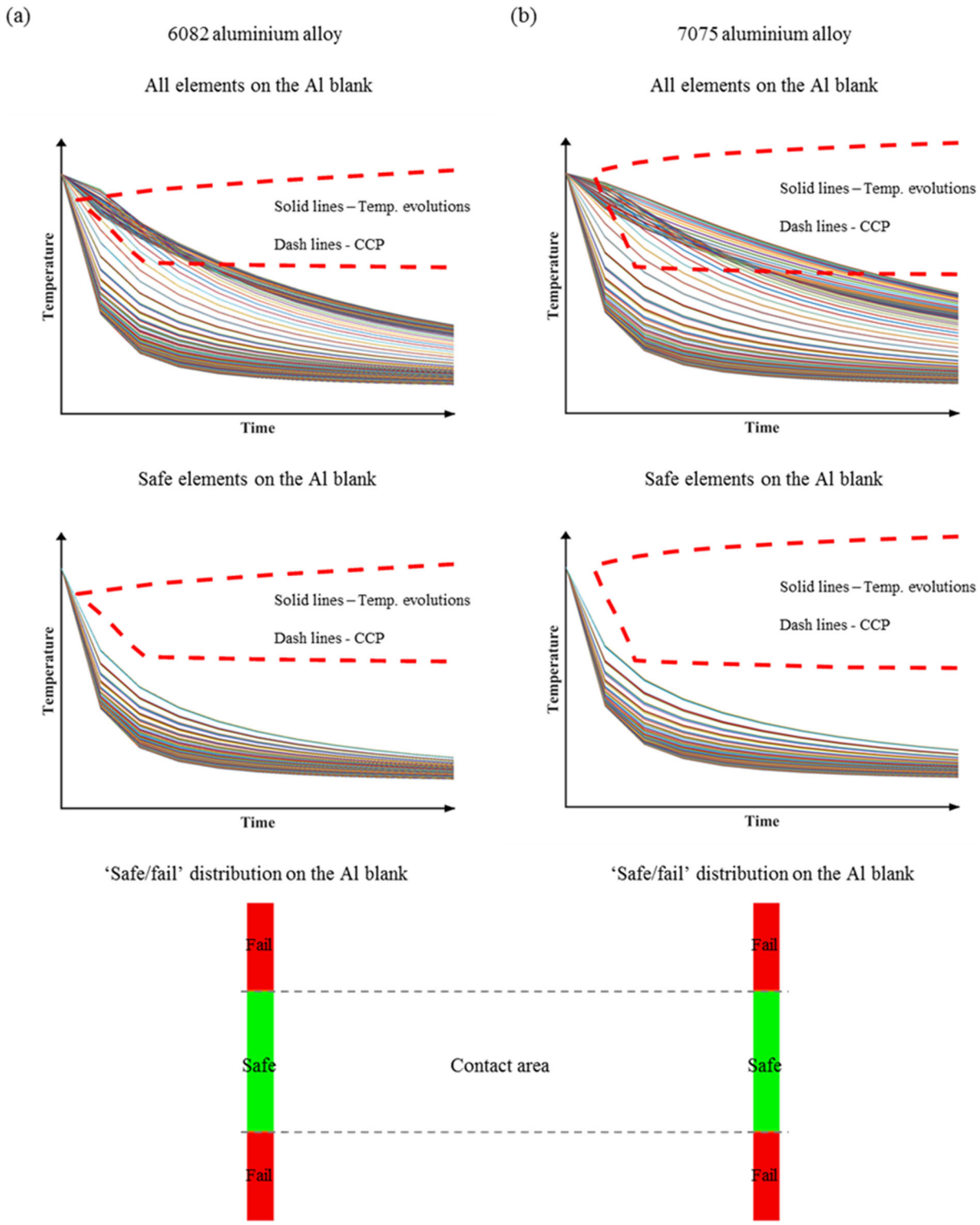

Figure 5.5 The temperature evolutions of all elements, the temperature evolutions of the 'safe' elements, after filtering, and the distributions of 'safe' and 'fail' elements on (a) the AA6082 blank at the critical contact pressure of 18 MPa; and (b) the AA7075 blank at the critical contact pressure of 28 MPa.

Similarly, different contact pressures were applied in the FE simulation to identify the critical value for AA7075. The number of 'safe' elements also increases with increasing contact pressure. Until the achievement of the contact pressure of 28 MPa, all elements on the contact area of the aluminium blank were 'safe', as shown in Figure 5.5 (b). This indicated that the critical contact pressure for AA7075 is 28 MPa under the same conditions, which is larger than that for AA6082. The identification of the critical contact pressures for different aluminium alloys is of great importance to not only ensure that the post-PBC strength of the materials can be fully retained but also prevent the application of excessive contact pressure, leading to increased energy consumption. It should be noted that the critical contact pressure would change under different forming processes. Under some specific conditions, the critical cooling rate and post-PBC strength of aluminium alloys may not be reached, whatever the contact pressure applied, which could be solved by applying lubricants and tools with higher thermal conductivities. Therefore, the critical processing parameters are characterised according to the applied forming processing windows.

5.3 Experimental validation of the critical contact pressures of M-shaped components under the FAST forming conditions

5.3.1 FAST forming of DA-TWBs panel components

Two dissimilar aluminium alloys, AA6082 and AA7075 supplied by Smiths Metal Centres Limited, were friction stir welded by The Welding Institute Limited as raw blanks to form M-shaped panel components under the FAST forming conditions, and their post-PBC hardness was subsequently measured to validate the determined critical contact pressures for both aluminium alloys simultaneously. A dissimilar alloy blank with a size of $90 \times 10 \times 2$ mm^3 was used in each test. The overall design of the non-isothermal M-shape forming simulator and the schematic diagram of the forming facility which intergated within the Gleeble 3800 can be found in Figure 5.6 and 5.7.

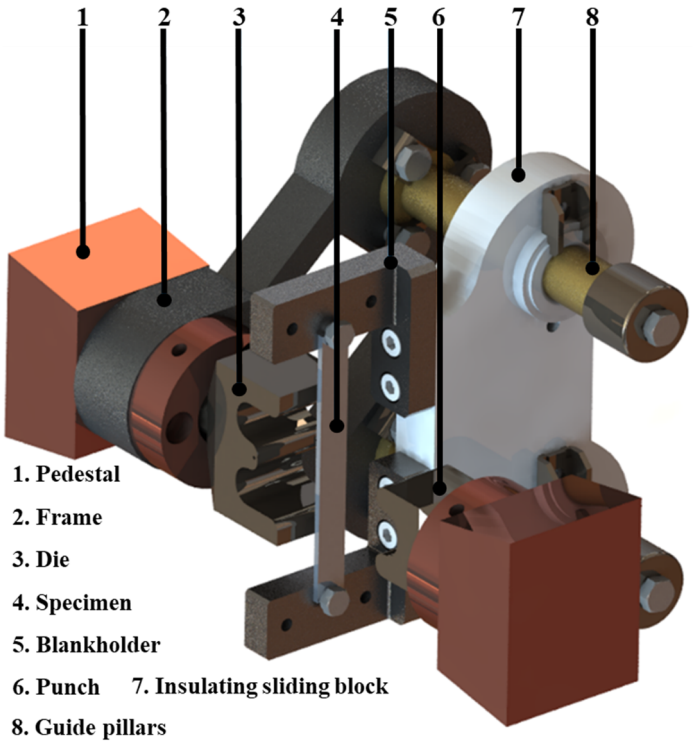

Figure 5.6 Overall design of the M-shape forming rig.

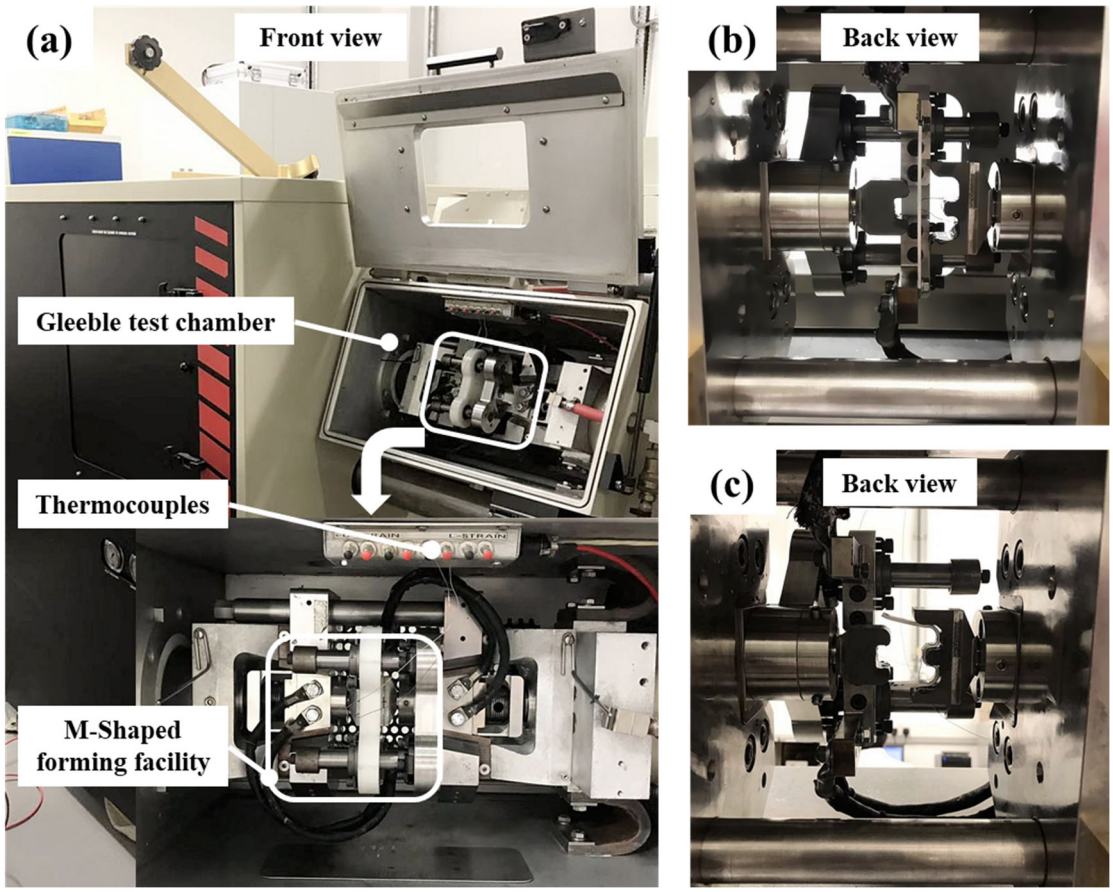

Figure 5.7 Schematic diagram of the M-shaped forming facility (a) set up within Gleeble 3800 (b) before forming and (c) after forming.

A cold forming process at room temperature was first conducted, and the component was severely fractured, as shown in Figure 5.8 (a). In order to increase the formability whilst maintaining the post-PBC strength of the material, the dissimilar aluminium alloy was deformed under FAST forming conditions. A blank was rapidly heated to the target temperature. Subsequently, the cold punch was activated to move along the guide pillars towards the cold die and deformed the blank into an M-shaped component, as shown in Figure 5.8 (b), followed by quenching of the component to room temperature at three different contact pressures of 10, 18 and 28 MPa. Meanwhile, the other processing parameters were identical to those used in the previous FE simulations. After artificial ageing, the post-PBC hardness of the components formed at three different contact pressures was measured by a Zwick ZHU hardness tester.

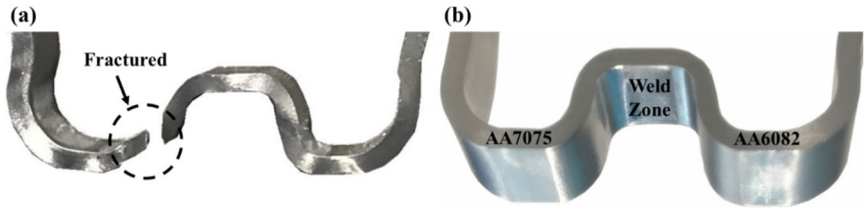

Figure 5.8 M-shaped component (a) formed at room temperature and (b) formed under the FAST forming conditions.

As shown in Figure 5.9, the hardness values of the as-received AA7075 and AA6082 were 181 and 121 HV respectively. Error bar shows the highest and lowest post-PBC hardness which were measured from 5 samples for each test condition. Due to the penetration of the dissimilar aluminium alloys in the welding zone, a decreasing trend of the hardness from 181 to 121 HV was observed. The post PBC hardness of the formed components was required to achieve at least 95 % of the as-received values. When the contact pressure was 10 MPa, the post-PBC hardness of the AA7075 was approximately 164 HV, which was 9.4 % lower than that of the as-received material, while the post-PBC hardness of the AA6082 was approximately 103 HV with a 14.9 % loss in its as-received value. This was due to the critical contact pressures for both AA6082 and AA7075 not being reached. When the contact pressure was 18 MPa, the critical contact pressure for the AA6082 was reached only. As a result, the post-PBC hardness of the AA6082 reached 97 % of its as-received hardness, while that of the AA7075 did not yet meet the requirement. When the contact pressure was 28 MPa, the post-PBC hardness of both AA6082 and AA7075 were fully retained, reaching 120 and 179 HV respectively. The

experimental observations agreed well with the previous deduction, i.e. the post-PBC hardness/strength can be fully retained only when the critical contact pressure is achieved.

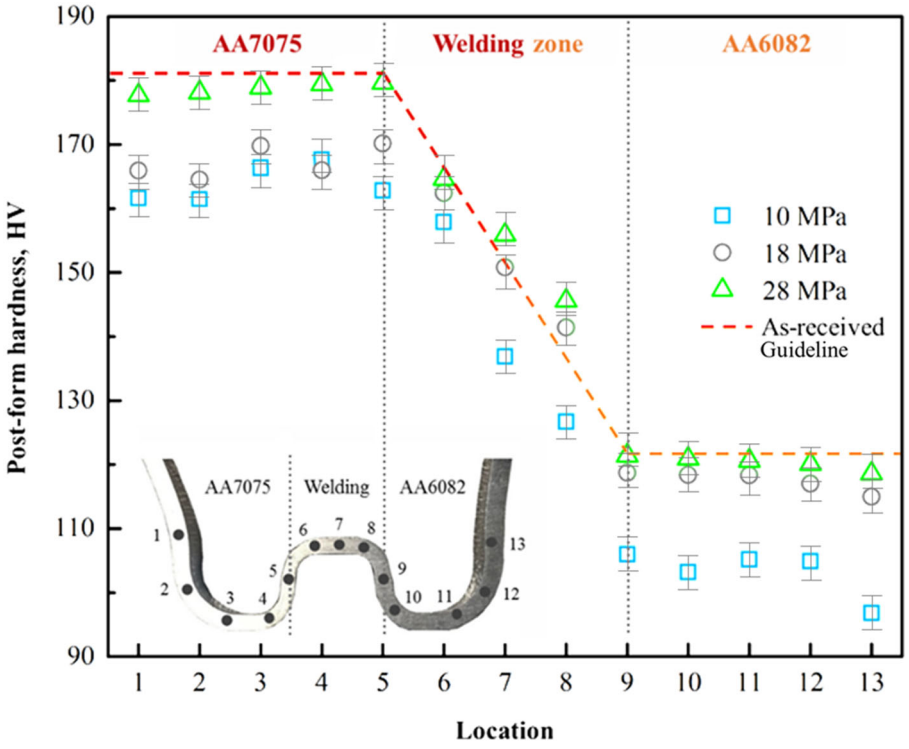

Figure 5.9 The hardness distributions at various contact pressures.

5.3.2 FE simulation of FAST forming of DA-TWBs panel components

Meanwhile, the FE simulation of the dissimilar alloy forming was performed in PAMSTAMP to predict the 'safe/fail' distributions on the formed component under different contact pressure conditions. The FE model was composed of three components, including a blank made from dissimilar aluminium alloys and a punch and die made from P20 tool steel, of which geometries were identical to those used in the experiments, as shown in Figure 5.10. Similar to the previous FE simulation identifying the processing parameters, the same quadrangle thermal shell elements with sizes of 1 × 1 mm^2 and 2 × 2 mm^2 were used for the blank and forming tools respectively. Additionally, the definition of degrees of freedom for all components and the simulation strategy were identical to the previous simulations, i.e. the hot blank was freely located onto the cold die, and the cold punch immediately moved along the z-direction to deform the blank into an M-shaped component, followed by quenching at different contact pressures of 10, 18 and 28 MPa. As a result of the IHTC evolutions being assigned, the heat transfer between the hot blank and cold forming tools occurred. Subsequently the temperature evolutions of the blank were exported and then compared with the CCP diagrams.

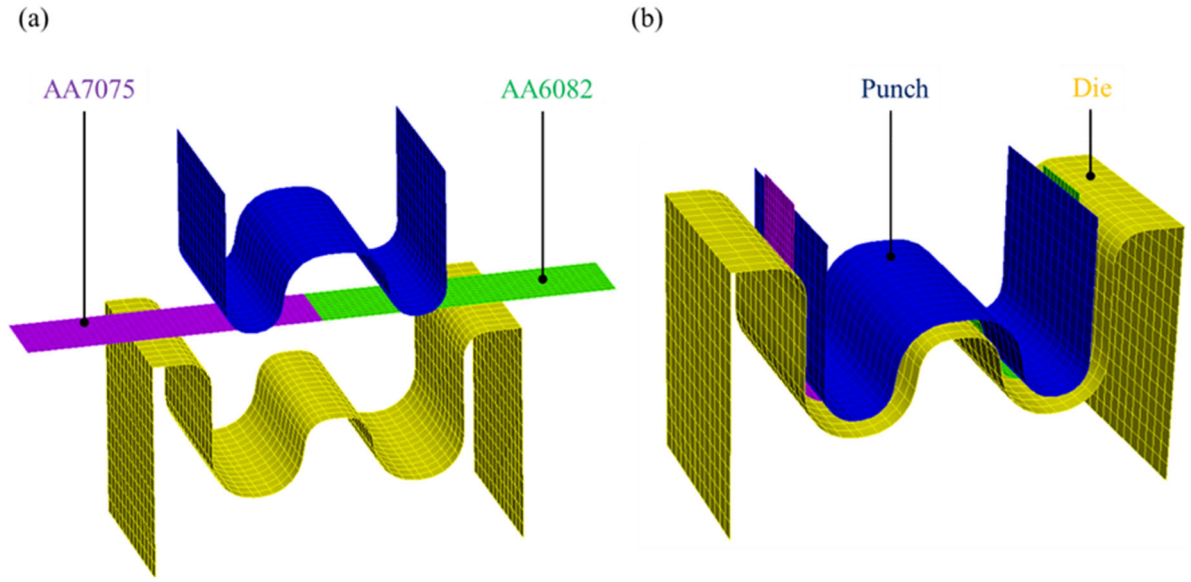

Figure 5.10 The FE model of a M-shape forming process under (a) loading; and (b) unloading conditions.

After the filtering process, the 'safe/fail' distributions on the M-shaped component under different contact pressure conditions were shown as Figure 5.11. Similarly, the 'safe' elements were shown as green colour, while the 'fail' elements were shown as red colour. Meanwhile, the shades of red colour represent the level of 'fail'. Due to the insufficient contact on the side vertical walls of the blank, its post-PBC strength was not able to achieve a high value under the applied forming conditions. Coincident with the experimental results, the entire blank failed to achieve a high post-PBC strength when the contact pressure was 10 MPa, while only the AA6082 part was 'safe' when the contact pressure increased to 18 MPa. Apart from the vertical walls, the rest of the blank was 'safe' to fully retain the post-PBC strength when the contact pressure increased to 28 MPa. Both the experimental and simulated results proved that the identified critical contact pressures of 18 and 28 MPa for the AA6082 and AA7075 respectively were accurate under the FAST forming conditions. Therefore, the developed method could enable the accurate identification of processing parameters under different forming conditions. Furthermore, FE simulation of forming processes can be first conducted to reduce the experimental efforts required to optimise the tool design and avoid the insufficient contact in particular regions, e.g. vertical walls and sharp corners, thus ensuring that the critical cooling rate and high post-PBC strength can be achieved after a proper PBC process.

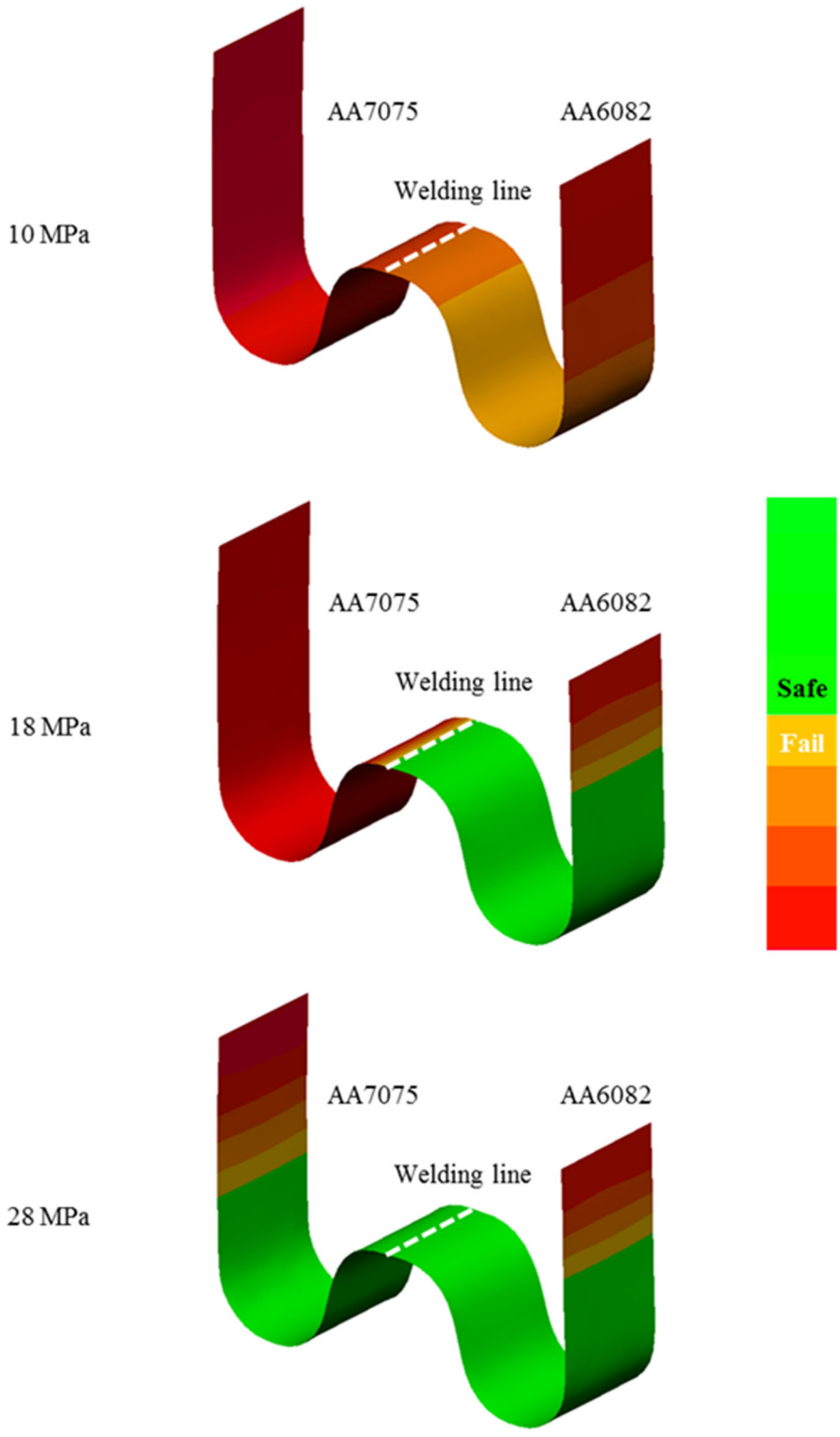

Figure 5.11 The ‘safe/fail’ distributions on the M-shaped component from dissimilar aluminium alloys at different contact pressures of 10, 18 and 28 MPa.

5.4 Summary

The present chapter utilised the developed general IHTC model and the predicted temperature evolutions of the aluminium alloys to identify the critical contact pressures in FAST forming processes for aluminium alloys. This efficient method is applicable to different forming technologies, dramatically saving experimental efforts. The detailed findings of this chapter are:

(1) A general aluminium alloy independent model was developed to predict the IHTC evolution as a function of contact pressure, surface roughness, initial blank temperature, initial blank thickness, tool material, coating material and lubricant material, using one set of fixed model constants.

(2) Through the integration of the temperature evolutions with CCP diagrams, the critical contact pressures of 18 MPa for the AA6082 and 28 MPa for the 7075 aluminium alloy under the FAST forming conditions were identified.

(3) Dissimilar AA6082 and AA7075 were friction stir welded as raw blanks to form M-shaped panel components at three contact pressures of 10, 18 and 28 MPa under the FAST forming conditions. The post-PBC hardness of the formed components was fully retained only when the critical contact pressure was reached, achieving approximately 97 % of the as-received hardness.

(4) The FE simulation of FAST forming of the dissimilar alloys was conducted to predict whether the post-PBC strength of components was reached at different contact pressures, validating the accuracy of the developed general IHTC model and the feasibility of the applied method to identify the processing parameters for aluminium alloys under different FAST conditions.

Chapter 6. Implementation of cloud finite element analysis (FEA) for FAST using the Smart Forming platform

In this chapter, a software agnostic platform, *Smart Forming*, was developed to provide cloud FEA of warm and hot stamping process as well as solutions for specific demands by operating model-driven functional modules, which could be classified into three main categories, namely pre-FE modelling, cloud FE simulation and post-FE evaluation. After providing the process window and materials involved in a desired warm and hot stamping process, the functional modules of pre-FE modelling were operated to generate the material properties and boundary conditions, which could be implemented in either local or cloud FE simulation. After providing the simulated results, the functional modules of post-FE evaluation were operated to generate the advanced evaluation criteria of the formed component, such as formability, quenching efficiency and post-PBC strength. In order to demonstrate the functionality and accuracy of the developed platform, cloud FEA of a FAST process was performed to replicate AA6082 component and was subsequently experimentally verified. The structure of this chapter is shown in Figure 6.1.

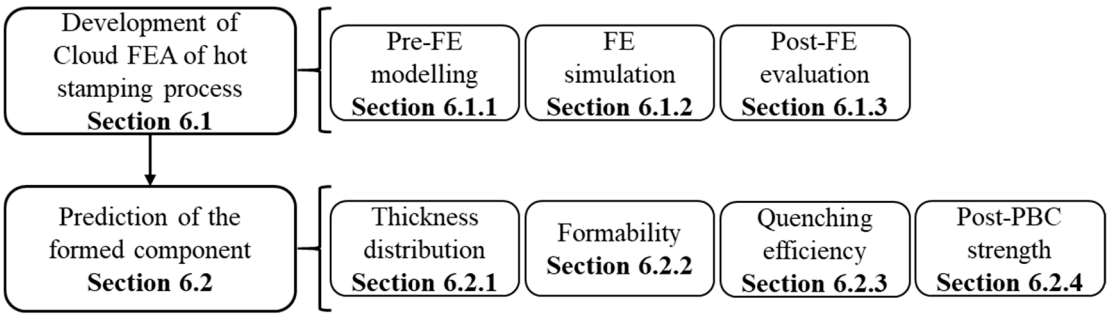

Figure 6.1 Schematic diagram of the sections covered in Chapter 6.

The work performed in Chapter 6 lead to the publication of the patent: "Cai, Z., Fakir, O. EL., Dhawan, S., Zhang, Q., Sun, Y., Luan, X., Wu, G., Wang, L., 2019. A data guided approach to manufacturing light-weight components. Patent application number: CN201910786108.0"

Chapter 6 is based on the paper publication "Cai, Z., Lim, Y. C., Dhawan. S., Liu, J., Politis, D. J., Wu, G., Wang, L., Liu, X., 2020. Cloud FEA of hot stamping processes using a software agnostic platform. The International Journal of Advanced Manufacturing Technology. (Under Review)"

6.1 Cloud FEA of hot stamping process

The flow chart of the cloud FEA hot stamping process in the Smart Forming platform is shown in Figure 6.2.

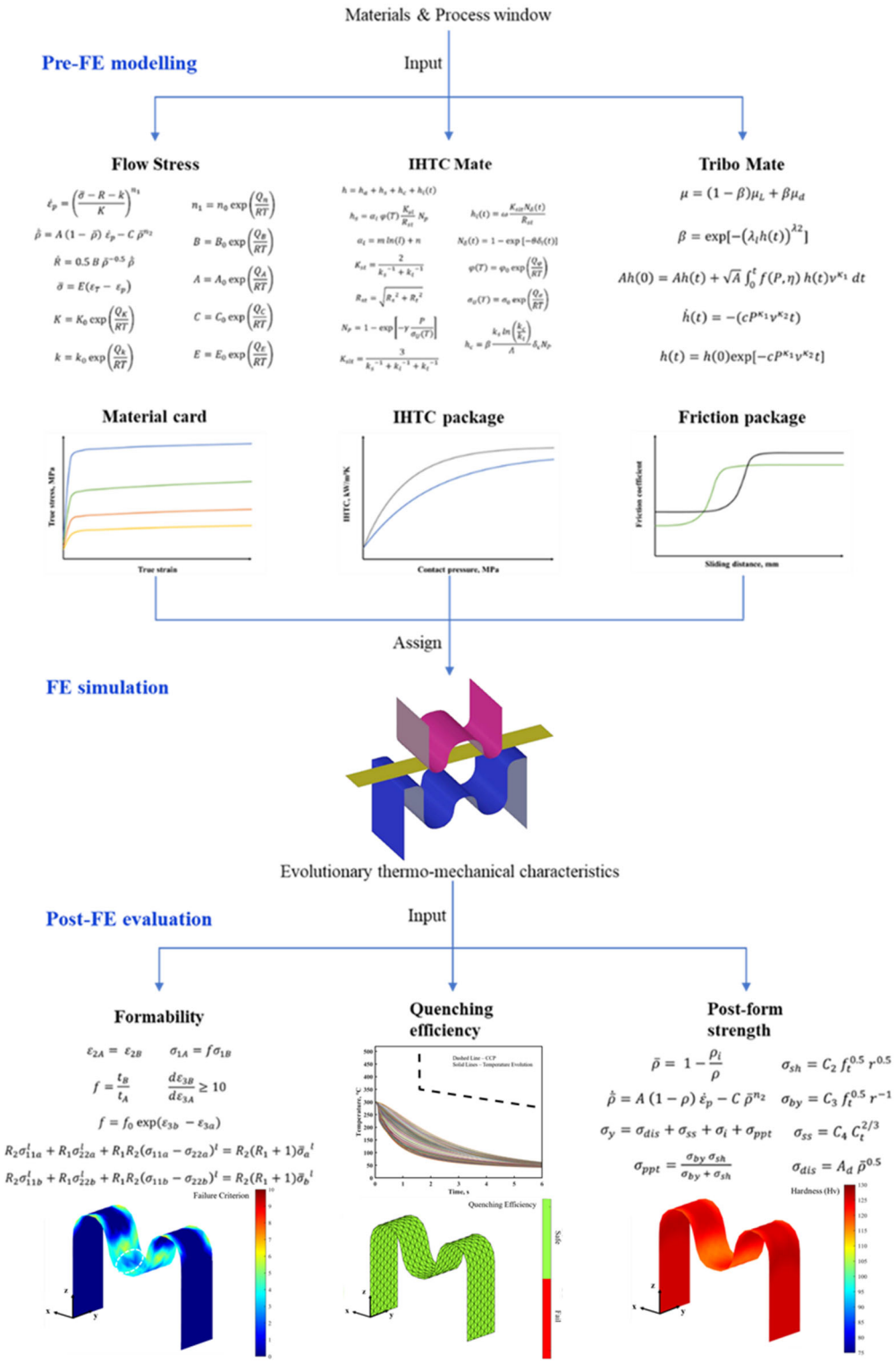

Figure 6.2 Flow chart of cloud FEA of a FAST process.

6.1.1 Pre-FE modelling

The model-driven functional modules prior to running the FE model were operated to account for the desired process parameters and materials used. In the FAST forming process, an AA6082 blank was heated to 300 °C at a fast heating rate of 50 °C/s. By avoiding soaking or pronounced temperature drop, the workpiece was immediately deformed by cold tools manufactured from P20 tool steel and lubricated by a graphite-based lubricant, at a stamping speed of 250 mm/s.

6.1.1.1 Flow stress and material card of AA6082

The functional module, Flow-stress, was operated to predict the stress-strain curves of the blank material AA6082 at a range of temperatures and strain rates by using the viscoplastic constitutive equations of the literature (Liu et al., 2018a) followed by the generation of a look-up table compatible to the FE software, as shown in Figure 6.3. Alternatively, the stress-strain curves could be acquired by performing the functional module named 'Material Card'. Meanwhile, the material properties of both the blank and tool materials shown in Table 6.1 were also contained in their respective material cards.

Table 6.1 Material properties of the AA6082 and P20 tool steel.

Properties	**Unit**	**AA6082**	**P20**
Density	kg/m^3	2700	7850
Young's modulus at 20°C	*GPa*	70.0	205
Young's modulus at 500°C	*GPa*	19.5	-
Poisson's ratio	-	0.3	0.285
Volumetric heat capacity	$J/(m^3 \cdot K)$	2.4×10^{-6}	3.6×10^{-6}
Thermal conductivity	$W/(m \cdot K)$	170	31.5
Thermal expansion coefficient	K^{-1}	24×10^{-6}	12.8×10^{-6}

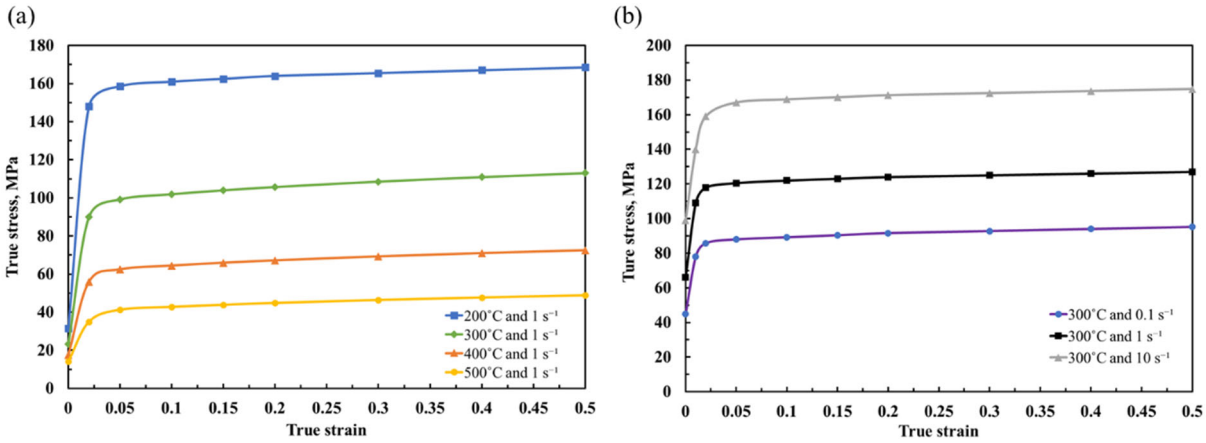

Figure 6.3 Stress-strain curves of the AA6082 at (a) a range of temperatures and (b) strain rates.

6.1.1.2 The IHTC and friction coefficient between AA6082 and P20

The functional module, IHTC-Mate, was operated to predict the IHTC evolutions as a function of contact pressure between the AA6082 and graphite-lubricated P20 by using a mechanism-based IHTC model (Liu et al., 2018b), as shown in Figure 6.4 (a).

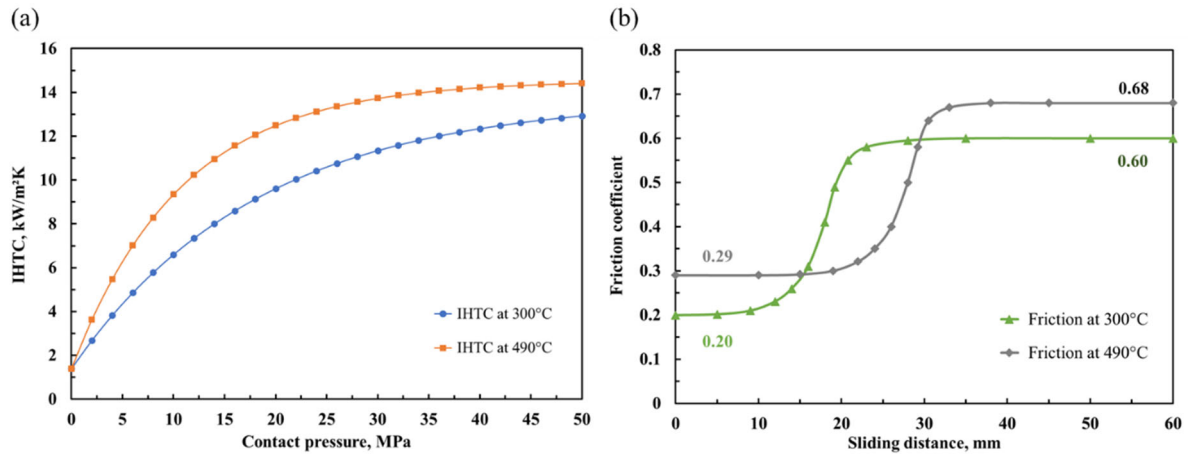

Figure 6.4 (a) The IHTC evolutions as a function of contact pressure, and (b) the friction coefficient evolutions as a function of sliding distance between the AA6082 and graphite-lubricated P20 for the FAST processes.

Due to the different forming temperatures being applied, the IHTC evolutions also varied for the FAST processes. Another functional module driven by an interactive friction model (Hu et al., 2019), Tribo-Mate, was able to predict the evolutions of the friction coefficient as a function of sliding distance between the AA6082 and graphite-lubricated P20 at different forming temperatures, whilst also accounting for lubricant breakdown, as shown in Figure 6.4 (b). In addition, the average friction coefficients could be generated by Tribo-Mate and be applied to

traditional FE software that is unable to accommodate evolutionary friction behaviour. Both the IHTC and friction coefficient were provided in the form of look-up tables or packages compatible to the FE software.

6.1.2 FE simulation of hot stamping processes in AutoForm

The FE simulation of FAST forming for a compact M-shaped panel component was performed in the software AutoForm, as shown in Figure 6.5. The material cards and boundary conditions generated by the functional modules of pre-FE modelling were implemented in both FE simulations. Subsequently, the blanks were set to be free on five degrees of freedom, the rigid dies remained stationary throughout the operation with all degrees of freedom locked, while the rigid punches and blankholder had only one degree of freedom in the forming direction. In the FE simulation of the FAST forming process, the blank and tools were meshed using triangular shell elements with a size of 2 mm^2, which were kept constant throughout the simulation to facilitate the subsequent post-FE evaluation process. The forming process consisted of three main stages. The first, a heating stage was defined to simulate the process of heating the blank to a target temperature, followed by a forming stage where the punch deformed the blank at the pre-defined forming speed. Finally, a quenching stage was defined whereby the punch was held against the deformed blank at a constant force to quench the formed component.

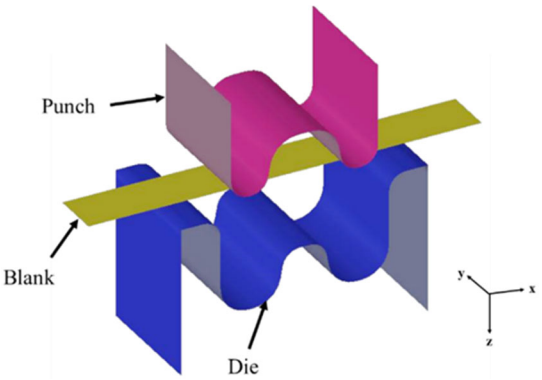

Figure 6.5 The FE models in AutoForm for the FAST forming of a compact M-shaped panel component.

To represent changes to the temperature of the tool surfaces during FAST forming processes, the active tool surfaces were projected in the stamping direction to form a volumetric mesh by a distance defined as the additional tool height.

6.1.3 Post-FE evaluation

After the FE simulation, the simulated evolutionary thermomechanical characteristics of each element were exported and then uploaded in the developed platform to operate the functional modules of post-FE evaluation, thereby predicting the formability, quenching efficiency and post-PBC strength of the formed components, as shown in Figure 6.2.

6.1.3.1 Formability of formed components

The simulated major strain, minor strain and temperature of each element at each time step were uploaded in the functional module, Formability, which applied the unified viscoplastic, Hosford and Marciniak-Kuczynski (MK) model to compute the failure criterion for each element, ranging from 1 to 10 (Gao et al., 2017). The propagation of a crack/necking increased with increasing failure criterion, while the onset of localised necking occurred when the critical value of 10 was reached. Subsequently, the failure criterion for all elements was distributed on the formed component and demonstrated by using a dedicated visualiser on the Smart Forming platform.

6.1.3.2 Quenching efficiency of formed components

The simulated temperature evolution as a function of forming time for each element were uploaded in the functional module, Tool-Maker, which superimposed the uploaded curves onto the CCP diagram of AA6082 (Milkereit et al., 2012). The critical quenching efficiency of an element was achieved when its temperature evolution did not intersect the CCP diagram, which was then defined as a safe element; otherwise, the element was insufficiently quenched and highlighted as a fail element. The distribution of quenching efficiency of the entire component was subsequently demonstrated by using the Smart Forming visualiser.

6.1.3.3 Post-PBC strength of formed components

In order to predict the evolution of the post-form strength of the formed component as a function of artificial ageing or other post-form heat treatment, the simulated major strain, minor strain and temperature of each element at each time step were required to be uploaded on the functional module, Tailor, driven by a post-form strength prediction model (Zhang et al., 2019). In addition, the process window of the post-form heat treatment (or PBC) was also required by this functional module. For instance, a 40 mins paint bake cycle was conducted at 120°C after the FAST forming. Subsequently, the distribution of the post-PBC strength of the formed component during the whole heat treatment process was computed and visualised.

6.2 Result and discussion

6.2.1 Prediction of the thickness distribution of formed components

The thickness distribution of the formed component was simulated by AutoForm. As shown in Figure 6.6, the simulated thickness distribution of the compact M-shaped component under the FAST forming conditions ranging from 1.93 to 2.01 mm had a close agreement with the experimentally-measured thickness with an error of less than 6 %, while the maximum thinning occurred on the side walls of the central bend. The simulated thickness results of FAST processes obtained from AutoForm verified the accuracy of the assigned material cards and boundary conditions to represent the complex nature of material flow behaviours and thermo-mechanical loadings in the hot stamping processes.

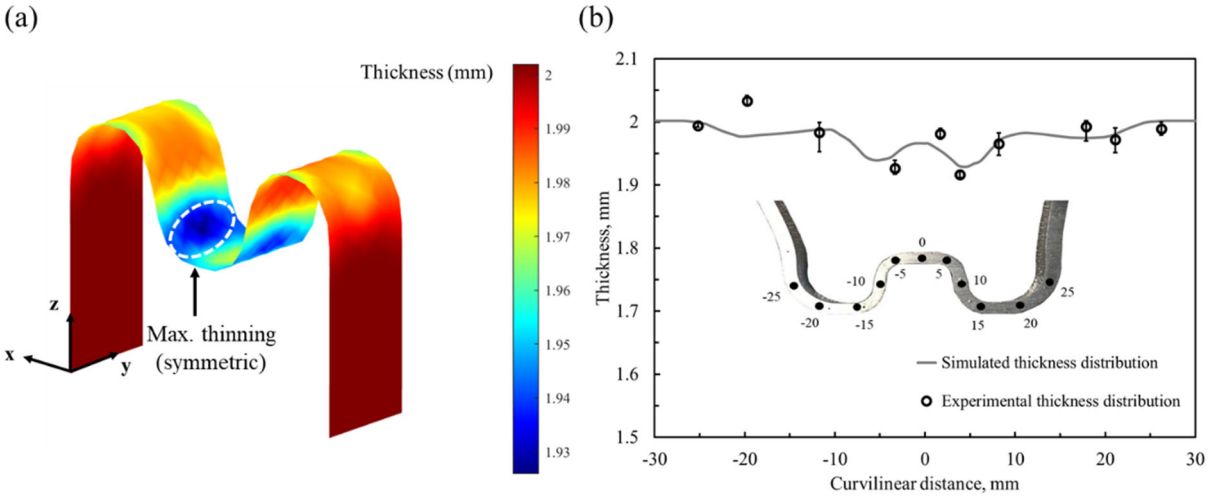

Figure 6.6 (a) FE simulated thickness distribution of the FAST-formed M-shaped component; (b) experimental and simulated thickness contour along the mid-section of the component.

6.2.2 Prediction of the formability and optimisation of the initial blank shape

The functional module, Formability, predicted the distributions of the failure criterion on two components, which were visualised on the developed platform. The failure criterion remained below the critical value for the FAST forming of the M-shaped component with a range of 1 to 6, as shown in Figure 6.7, which was verified by the forming trials since the components were successfully formed with no visible necking/cracking, as shown in Figure 6.6 (b). However, the maximum failure criterion did not occur on the regions that experienced the maximum thinning. As mentioned, the formability was a combined result of the temperature, strain rate and loading path. The temperature and strain rate of the adjacent regions with the maximum failure criterion and thinning were similar, while the loading path of those two regions was

uniaxial when drawing in the die cavity, followed by a transition to biaxiality when the central bend was stretched into the M-shape. The region with the maximum thinning was continuously stretched by a biaxial loading at the end of the forming process, while the region with the maximum failure criterion was at a plan loading, thus resulting in a lower formability. Due to the different loading path, the region with the maximum failure criterion was therefore located on the side wall of the central bend, which was not consistent with the region at the maximum thinning on the central bend.

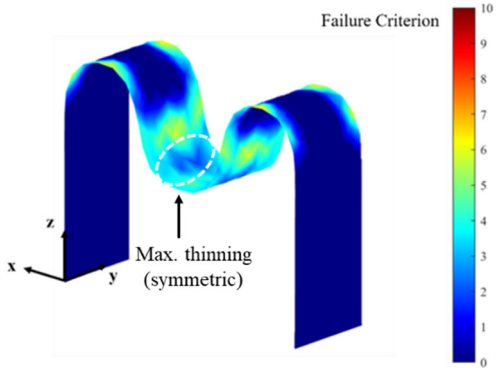

Figure 6.7 Prediction of the formability of the M-shaped component under the FAST forming conditions.

The formability prediction of the FAST processes indicated that the failure could not be simply evaluated by thickness/thinning distribution under the complex thermal and mechanical conditions. Instead, the combined effect of temperature, strain rate and loading path could contribute to an accurate prediction of the formability of the formed component. The significant change in the failure criterion distribution emphasised the sensitivity of the initial blank shape in the hot stamping processes. The functional module, Formability, is therefore necessary to predict the failure of the formed component as a combined result of temperature, strain rate and loading path as well as optimise the initial blank shape.

6.2.3 Prediction of the quenching efficiency of formed components

The functional module, Tool-Maker, predicted the quenching efficiency of the two components under the FAST forming condition. Figure 6.8 (a) shows the comparison between the temperature evolutions of all elements on the M-shaped component and the CCP diagram of AA6082. As no intersection was found, the entire formed component was sufficiently quenched and then visualised on the platform, as shown in Figure 6.8 (b). Consequently, secondary phases that consume alloying elements would not precipitate and thus a high post-PBC strength would be obtained after a proper artificial ageing process (or PBC). This also

indicated that the applied tool material P20, the designed tool geometry, e.g. the die clearance, radius of fillet and angle of side walls, and the selected process windows, including the forming temperature, blankholding force and die-closing force, ensured the critical quenching efficiency to be met in the FAST forming process. Therefore, the functional module, Tool-Maker, was able to optimise the tool design and process window by the prediction of the quenching efficiency.

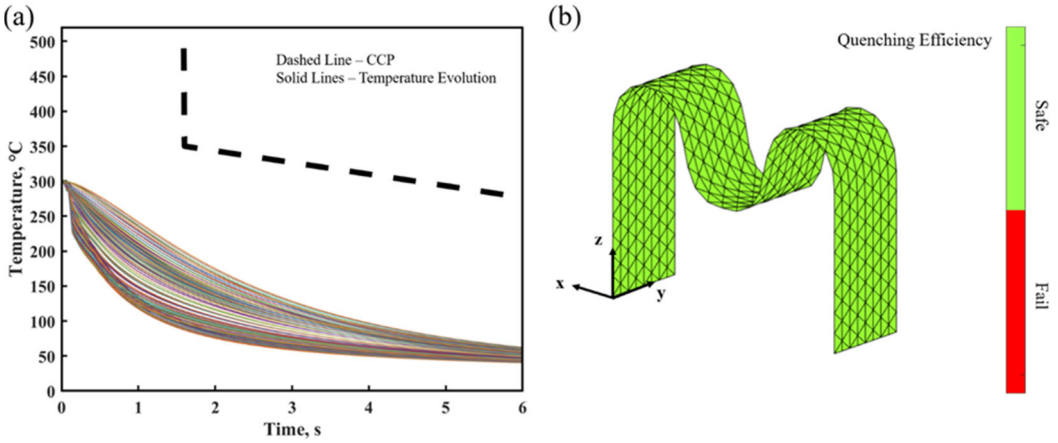

Figure 6.8 (a) Comparison between the temperature evolutions of all the elements and CCP diagram; (b) visualisation of the quenching efficiency distribution for the FAST-formed M-shaped component.

6.2.4 Prediction of the post-PBC strength of formed components

The functional module, Tailor, predicted and visualised the distributions of the post-PBC hardness of the formed component during the PBC. As shown in Figure 6.9, the average hardness of the M-shaped component was 84 HV after quenching and increased in the subsequent paint bake cycle at 120 °C, reaching 107 HV after baking for 20 mins and the peak value of 121 HV after baking for 40 mins. The hardness of the M-shaped component was experimentally measured along its section contour after quenching and paint bake cycle of 40 mins, showing the average values of 86 and 120 HV respectively. The error of the post-PBC hardness predicted by the functional module was less than 8 %.

The prediction of the post-PBC strength/hardness of the component mainly depended on the contributions of dislocation hardening, solid solution hardening and precipitation hardening. The contributions of dislocation hardening and solid solution hardening were closely tied to the normalised dislocation density, which was determined by the strain and strain rate experienced by the component. As the precipitates initiated and grew during the PBC, the effect

of precipitation hardening became the largest contributor to the increase in the hardness. Therefore, the post-PBC strength of the M-shaped component could be retained after a short heat treatment due to a fine microstructure being obtained after rapid heating in the FAST forming process. Hence, after post-processing the strain and temperature of the formed component, Tailor was able to predict the evolution of the post-PBC strength as a function of heat treatment, thereby computing the peak strength and optimising the process window of the PBC process.

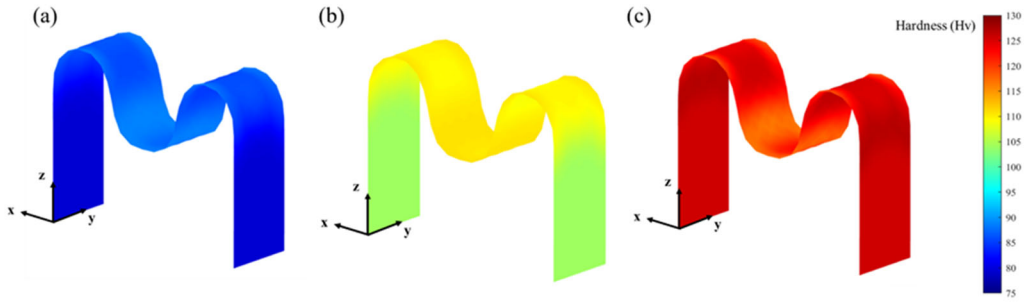

Figure 6.9 Predicted post-PBC hardness distribution of the FAST-formed M-shaped component (a) after quenching, (b) after the paint bake of 20 mins and (c) after the paint bake cycle of 40 mins.

6.3 Summary

A software agnostic platform '*Smart Forming*', integrated by the model-driven functional modules, was developed in the present research to provide cloud FEA of the FAST forming of a compact M-shaped component made from AA6082. According to the applied materials and processing window, the flow stress, material properties, IHTC and friction coefficient could be generated by the functional modules named Flow Stress, Material Card, IHTC-Mate and Tribo-Mate, respectively, in the form of compatible packages that fed directly into the desired FE software. Subsequently, the FE simulation of the hot stamping process was performed either locally or remotely on the developed platform. After uploading the simulated evolutionary thermomechanical characteristics of the formed component onto the platform, the functional modules named Formability, Tool-Maker and Tailor could be operated to predict and demonstrate the distributions of the formability, quenching efficiency and post-PBC strength respectively on the dedicated visualiser, thereby optimising the initial blank shape, tool design and process window. Close agreements between the cloud FEA and experimental results were found with an error of less than 10 %, verifying the accuracy of the developed *Smart Forming* platform.

Chapter 7. Conclusions and suggestions for future work

7.1 Conclusions

In this thesis, a novel sheet metal forming technology – Fast light Alloys Stamping Technology (FAST) was proposed and experimentally verified in lab scale for the manufacture of panel components from Tailor-Welded Blanks of Dissimilar Alloys (DA-TWBs). The proposed method achieved desirable mechanical properties in a cost and time efficient manner. The optimised processing window of the FAST process and a comprehensive understanding of the thermal-mechanical properties, including a post-PBC strength investigation on various forming process conditions were conducted. The implementation of the proposed FAST process was conducted by forming M-shaped and U-shaped panel components. A general aluminium alloy-independent model with a single set of fixed constants was developed to predict the Interfacial Heat Transfer Coefficient (IHTC) evolutions and was applied to simulate the temperature evolutions during FAST forming processes. A software agnostic platform, *Smart Forming*, was developed to provide cloud Finite Element Analysis (FEA) of hot and warm stamping processes as well as solutions for specific demands by operating model-driven functional modules. The key findings from the project are highlighted in the following sections.

7.1.1 Development of FAST process and implementation on forming U-shaped components made from DA-TWBs

The proposed FAST process utilises the ultra-fast heating of an aluminium alloy sheet to an appropriate temperature, which reduces the total forming cycle time to under 8 seconds whilst reducing energy consumption. FAST enables a similar strength of the as-received material to be retained in the formed components, and the springback effect is also reduced or eliminated depending on the complexity of the component. The feasibility of the FAST was initially studied on the AA6082 and AA7075 materials respectively, then applied to the application of DA-TWBs by using the common processing window suitable for both the AA6082 and AA7075 alloys.

In the thermo-mechanical properties investigation, uniaxial tensile tests were conducted to determine the thermo-mechanical properties of two base materials AA6082 and AA7075 at FAST conditions using a Gleeble 3800 thermo-mechanical simulation and testing system. The experimental results indicated that the increase of testing temperature leads to a decrease in flow stress but an increase in the ductility of the AA6082. The true failure strain (strain at fracture) of AA6082 increases from 0.25 to 0.85 when the temperature increases from 300 to 535 °C. The reduction in flow stress and increase in failure strain can be explained by thermally activated deformation mechanisms. As the temperature increases, the mobility of atoms and dislocations is enhanced. Therefore, the material becomes softer and more ductile. However, the reverse trend was found by using AA7075 as the ductility decreased sharply for temperatures above 425 °C. In addition, the flow stress and ductility of AA6082 increases with increasing strain rate due to the strain rate hardening effect, the failure strain increased from 0.65 to 0.95 when the strain rate increased from 0.1 to 5 s^{-1}. However, increasing strain rate has a negative effect on ductility for AA7075, but a positive reaction on flow stress.

The performance of post-Paint Bake Cycle (PBC) hardness was evaluated with various effects including pre-treatment time, heating rate, soaking time, forming temperature and quenching rate. The experimental results indicated that heat treatment time plays a very important role on post-PBC hardness of materials, as the time should be controlled precisely to avoid over ageing during the heat treatment and forming stages. Slow heating rate was found to have a negative effect on the post-PBC hardness, as the slow heating allows for the formation of coarse precipitates, which results in fast growth with slow nucleation. Thus, additional dislocation motion led to lower hardness. A shorter soaking time was suggested for the FAST process, as this led to fewer or completed avoided coarse precipitates which is the main barrier to increasing post-PBC hardness. In addition, high forming temperatures in FAST between 400 and 535 °C achieved only 83 % of the as-received material hardness which limits the application of AA6082 and AA7075 materials on a vehicle structure. However, it was found that 98% of post-PBC hardness was achievable when formed at 300 °C. Moreover, fast quenching rate with over 50 °C/s proved to be essential for the FAST process in order to minimise the post-PBC hardness reduction.

The validation of the FAST was conducted by forming U-shaped components from the AA6082 and AA7075 via a dedicated lab-scale pilot production line “Uni-Form”. The experimental test results indicated that U-shaped components were successfully formed by

using FAST, and the hardness was distributed evenly along the cross-section of the U-shaped parts, with the PFH value of approximately 118 and 178 HV for AA6082 and AA7075, respectively. By comparing with the hardness of as-received materials, the FAST formed U-shaped component under the suggested forming window can achieve a 98% hardness recovery. Springback under FAST forming conditions was successfully evaluated at different forming temperatures and speeds. It was found that decreasing springback angle or complete elimination of springback was possible when increasing forming temperature and punch speed. The reason for that was due the flow stress that was decreased with increasing forming temperature which results in decreased elastic deformation, and hence a reduction in springback effect.

The optimal forming window for FAST of the DA-TWBs was suggested to be pre-aging at the 180 and 120 °C and soaking for 60 and 75 minutes for AA6082 and AA7075 respectively. Moreover, the forming temperature range between 250 and 350 °C and above 450 °C respectively at a heating rate greater than 50 °C/s, and no soaking time was required.

The optimised FAST process was successfully implemented to form a U-shaped component made from DA-TWBs at 300 °C. The experimental results of springback angle indicated that good forming accuracy was achieved as all the springback angles were less than 1.8°. By comparing with the hardness of as-received material, the post-PBC hardness recovery that can be achieved is approximately 98 % and 97 % for the AA6082 and AA7075 materials, respectively. In addition, the FAST has enabled a significant reduction of total cycle time from several hours to 10 seconds, which further improved the production rate to 12.5 stroke per minute (spm).

7.1.2 Development of a general IHTC model to characterize the critical processing parameters in the FAST process

The general IHTC model was developed and predicted the temperature evolutions of the aluminium alloys to identify the critical contact pressures in FAST forming processes. This efficient method is applicable to different forming technologies, dramatically reducing experimental efforts. In the general aluminium alloys independent IHTC model, one set of fixed model constants was used which characterize the functions of contact pressure, surface roughness, initial blank temperature, initial blank thickness, tool material, coating material and lubricant material. The critical contact pressures of 18 MPa for the AA6082 and 28 MPa for

the AA7075 under the FAST forming conditions were identified by intergrating with the temperature evolutions identified from the respective materials Continuous Cooling Precipitation (CCP) diagrams. The critical contact pressure was defined as 28 MPa for forming of M-shaped DA-TWBs, and Post-PBC hardness of the formed component was fully retained which achieved approximately 97 % of the as-received hardness. The FE simulation of FAST forming of the dissimilar alloys was conducted to predict whether the post-PBC hardness of components was reached at different contact pressures, validating the accuracy of the developed general IHTC model and the feasibility of the applied method to identify the processing parameters for aluminium alloys under different FAST conditions.

7.1.3 Implementation of cloud finite element analysis (FEA) for hot stamping processes using the Smart Forming platform

A software agnostic platform '*Smart Forming*', integrated by the model-driven functional modules was developed, and verified in the cloud FEA of the FAST forming of a compact M-shaped component made from AA6082. According to the applied materials and processing window, the flow stress, material properties, IHTC and friction coefficient could be generated by the functional modules named Flow Stress, Material Card, IHTC-Mate and Tribo-Mate, respectively, in the form of compatible packages that fed directly into the desired Finite Element (FE) software. Subsequently, the FE simulation of the hot stamping process was performed either locally or remotely on the developed platform. After uploading the simulated evolutionary thermomechanical characteristics of the formed component onto the platform, the functional modules named Formability, Tool-Maker and Tailor could be operated to predict and demonstrate the distributions of the formability, quenching efficiency and post-PBC strength respectively on the dedicated visualiser, thereby optimising the initial blank shape, tool design and process window. Close agreements between the cloud FEA and experimental results were found with an error of less than 10 %, verifying the accuracy of the developed Smart Forming platform.

7.2 Suggestions for future work

7.2.1 Post-PBC strength (hardness) prediction of DA-TWBs under FAST conditions

FAST forming is a non-isothermal forming process which includes the processes of material pre-treatment and fast heating and quenching, which was successfully implemented on forming of M-shaped and U-shaped components. In addition, an optimal forming processing window was developed by conducting a large amount of experimental trials in order to obtain the desired post-PBC strength. Moreover, the precise forming parameters depend on the thermal mechanical properties of the test materials, and thus the entire experimental procedure should be repeated for new materials or when a different batch of material is applied. Therefore, it is essential to develop a model to predict the post-PBC strength of DA-TWBs under FAST condition, which will improve the efficiency of the FAST development and enables the wide application of FAST with shorter development time. In order to develop the prediction model, the knowledge of precipitation hardening sequence during the material pre-treatment, heating and quenching stages are required.

7.2.2 Further investigation of the FAST

In this thesis, FAST was proposed and experimentally verified in lab scale for panel components from tailor-welded blanks manufactured by dissimilar alloys (DA-TWBs). A comprehensive study was carried out including the fundamental experiments, thermal mechanism investigation and forming trials on AA6082 and AA7075. However, the forming limit of those materials under FAST condition should also carried out to investigate the effect of forming temperature and forming speed (strain rate). In addition, tests may be conducted on Scanning Electron Microscopy (SEM) or Transmission Electron Microscopy (TEM) to identify the precipitates during each stage of the FAST process.

7.2.3 Further development of functional module on cloud FEA platform

The collaboration and contribution of experts from around the world will lead towards the success of the '*Smart Forming*' cloud based FEA platform. Currently, three functional modules were developed which provide a wide range of solutions in the warm and hot stamping field. However, in order to provide an in depth understanding of the material pre-treatment, FAST

forming and Original Equipment Manufacturer (OEM)'s PBC, additional functional modules are encouraged to be created and developed. In pre-treatment, the specimen mechanical properties were influenced by treatment temperature and total time. Thus, the pre-treatment modules could be developed based on large volumes of available experimental test data, for example the uniaxial tensile test and post-PBC strength data. In FAST forming, a blank was subjected to fast heating, forming and quenching. A functional module could be established incorporating the effects of precipitation behaviour of different materials, various forming parameters, and precise tool design to ensure critical quenching rate and profile accuracy. In the future, the product development and production rate should be further reduced by using FAST with the aid of knowledge sharing platform – '*Smart Forming*'. The stages of material pre-treatment and welding could be completed by the material manufacturer or supplier, and the OEM paint bake cycle could be completed on-site with the automotive manufacturer.

The cloud FEA platform was not only designed for the FAST process but also aims to address other forming process, slow forming processes such as incremental forming could be integrated into the platform. In this PhD research, the feasibility study of Single Point Incremental Forming (SPIF) was also conducted on AA5754 by forming a bowl-shaped component under various forming conditions, including the geometry of the forming tool, forming path and incremental depth. In the next stage, the large amount of experiment data generated will be aggregated and classified, with the aim to enable the development of functional modules for lower speed and flexible forming processes.

References:

Aalco. (2020) *Aluminium Alloy - Commercial Alloy - 6082 - T6* Available from: http://www.aalco.co.uk/datasheets/Aluminium-Alloy_6082-T6~T651_148.ashx [Accessed 19th September 2020].

Abedrabbo, N., Pourboghrat, F. & Carsley, J. (2006a) Forming of aluminum alloys at elevated temperatures – Part 1: Material characterization. *International Journal of Plasticity.* 22**,** 314-341.

Abedrabbo, N., Pourboghrat, F. & Carsley, J. (2006b) Forming of aluminum alloys at elevated temperatures – Part 2: Numerical modeling and experimental verification. *International Journal of Plasticity.* 22**,** 342-373.

Altan, T. & Tekkaya, A. (2012) *Sheet Metal Forming: Processes and Applications.*The United States of America, ASM International.

Antunes, R. A. & De Oliveira, M. C. L. (2014) Materials selection for hot stamped automotive body parts: An application of the Ashby approach based on the strain hardening exponent and stacking fault energy of materials. *Materials & Design.* 63**,** 247-256.

Arcelor Mittal. (2010) *ArcelorMittal Tailored Blanks*. Available from: https://corporate.arcelormittal.com/ [Accessed 14th June 2019].

ASM. (2020) *Aluminum 7075-T6* Available from: http://asm.matweb.com/search/SpecificMaterial.asp?bassnum=MA7075T6 [Accessed 16th September 2020].

ASTM. (1936) *Symposium on High-Strength Constructional Metals.*The United States of America, American Society for Testing Materials (ASTM).

Bai, Q., Lin, J., Zhan, L., Dean, T. A., Balint, D. S. & Zhang, Z. (2012) An efficient closed-form method for determining interfacial heat transfer coefficient in metal forming. *International Journal of Machine Tools and Manufacture.* 56**,** 102-110.

Behrens, B.-A., Nürnberger, F., Bonk, C., Hübner, S., Behrens, S. & Vogt, H. (2017) Influences on the formability and mechanical properties of 7000-aluminum alloys in hot and warm forming. *Journal of Physics: Conference Series.* 896**,** 012004.

Berg, L. K., Gjønnes, J., Hansen, V., Li, X.-Z., Wedel, M., Waterloo, G., Schryvers, D. & Wallenberg, R. (2001) GP-zones in Al–Zn–Mg alloys and their role in artificial aging. *Acta Materialia.* 49**,** 3443-3451.

Bhanodaya Kiran Babu, N., Davidson, M. J., Neelakanteswara Rao, A., Balasubramanian, K. & Govindaraju, M. (2014) Effect of differential heat treatment on the formability of aluminium tailor welded blanks. *Materials & Design.* 55**,** 35-42.

Boukha, Z., Sánchez-Amaya, J., Amaya Vázquez, M. R., Rovira, L. & Botana, J. (2012) Laser Welding of Aeronautical and Automobile Aluminum Alloys. *AIP Conference Proceedings.* 1431**,** 974-981.

British Standards. (2017). *EN 515: Aluminium and aluminium alloys.* The United Kingdom, BSI.

Buchner, B., Buchner, M. & Buchmayr, B. (2009) Determination of the real contact area for numerical simulation. *Tribology International.* 42**,** 897-901.

Buffa, G., Fratini, L., Merklein, M. & Staud, D. (2007) Investigations on the Mechanical Properties and Formability of Friction Stir Welded Tailored Blanks. *Key Engineering Materials.* 344**,** 143-150.

Cai, Z., Fakir, O. E., Dhawan, S., Zhang, Q., Sun, Y., Luan, X., Wu, G. & Wang, L. 2019. *A data guided approach to manufacturing light-weight components*. China patent application CN201910786108.0.

Cai, Z., Liu, X., Zhang, Q., Wu, G., Zhu, M. & Wang, L. 2020. *Method of forming parts from tailor-welded blanks manufactured by dissimilar alloys*. China patent application CN2020xxxxxxxx.x.

Campbell, F. C. (2006) Chapter 2 - Aluminum. *In:* Campbell, F. C. (ed.) *Manufacturing Technology for Aerospace Structural Materials.* The United Kingdom, Elsevier Science, pp. 15-92.

Caron, E. J. F. R., Daun, K. J. & Wells, M. A. (2014) Experimental heat transfer coefficient measurements during hot forming die quenching of boron steel at high temperatures. *International Journal of Heat and Mass Transfer.* 71**,** 396-404.

Chang, Y., Tang, X., Zhao, K., Hu, P. & Wu, Y. (2016) Investigation of the factors influencing the interfacial heat transfer coefficient in hot stamping. *Journal of Materials Processing Technology.* 228**,** 25-33.

Chrominski, W. & Lewandowska, M. (2016) Precipitation phenomena in ultrafine grained Al–Mg–Si alloy with heterogeneous microstructure. *Acta Materialia.* 103**,** 547-557.

Cooper, M. G., Mikic, B. B. & Yovanovich, M. M. (1969) Thermal contact conductance. *International Journal of Heat and Mass Transfer.* 12**,** 279-300.

Davis, J. R. (1993) *Aluminum and aluminum alloys.*The United States of America, ASM international.

Davis, J. R. (2004) *Tensile Testing.*The United States of America, ASM International.

Dursun, T. & Soutis, C. (2014) Recent developments in advanced aircraft aluminium alloys. *Materials & Design (1980-2015).* 56**,** 862-871.

El Fakir, O., Wang, L., Balint, D., Dear, J. P., Lin, J. & Dean, T. A. (2014) Numerical study of the solution heat treatment, forming, and in-die quenching (HFQ) process on AA5754. *International Journal of Machine Tools and Manufacture.* 87**,** 39-48.

Engler, O. & Hirsch, J. (2002) Texture control by thermomechanical processing of AA6xxx Al–Mg–Si sheet alloys for automotive applications—a review. *Materials Science and Engineering: A.* 336**,** 249-262.

EPA. (2019) *Sources of Greenhouse Gas Emissions*. Available from: https://www.epa.gov/ghgemissions/sources-greenhouse-gas-emissions#transportation [Accessed 15th June 2020].

European Aluminium. (2017) *The Aluminium Automotive Manual*. Available from: https://european-aluminium.eu/resource-hub/aluminium-automotive-manual/ [Accessed 16th June 2020].

European Commission. (2017) *Reducing CO2 emissions from passenger cars - before 2020*. Available from: https://ec.europa.eu/clima/policies/transport/vehicles/cars_en [Accessed 16th June 2020].

Fan, X., He, Z., Yuan, S. & Zheng, K. (2013) Experimental investigation on hot forming–quenching integrated process of 6A02 aluminum alloy sheet. *Materials Science and Engineering: A.* 573**,** 154-160.

Fan, X., He, Z., Zheng, K. & Yuan, S. (2015) Strengthening behavior of Al–Cu–Mg alloy sheet in hot forming–quenching integrated process with cold–hot dies. *Materials & Design.* 83**,** 557-565.

Feistauer, E., Bergmann, L., Barreto, L. & Dos Santos, J. (2014) Mechanical behaviour of dissimilar friction stir welded tailor welded blanks in Al–Mg alloys for Marine applications. *Materials & Design.* 59**,** 323–332.

Foster, A. D., Dean, T. A. & Lin, J. 2010. *Process for forming aluminium alloy sheet component*. The United Kingdom patent application EP 09785115 A. 16th January 2013.

Gaied, S., Roelandt, J.-M., Pinard, F., Schmit, F. & Balabane, M. (2009) Experimental and numerical assessment of Tailor-Welded Blanks formability. *Journal of Materials Processing Tech.* 209.

Gao, H., El Fakir, O., Wang, L., Politis, D. J. & Li, Z. (2017) Forming limit prediction for hot stamping processes featuring non-isothermal and complex loading conditions. *International Journal of Mechanical Sciences.* 131-132**,** 792-810.

Garrett, R. P., Lin, J. & Dean, T. A. (2005) An investigation of the effects of solution heat treatment on mechanical properties for AA 6xxx alloys: experimentation and modelling. *International Journal of Plasticity.* 21**,** 1640-1657.

Gasson, P. C. (2003) *Mechanics of Sheet Metal Forming.*The United Kingdom, Cambridge University Press.

Ghosh, M., Miroux, A., Werkhoven, R. J., Bolt, P. J. & Kestens, L. a. I. (2014) Warm deep-drawing and post drawing analysis of two Al–Mg–Si alloys. *Journal of Materials Processing Technology.* 214**,** 756-766.

Greiser, J., Müller, D., Müllner, P., Thompson, C. V. & Arzt, E. (1999) Growth of giant grains in silver thin films. *Scripta Materialia.* 41**,** 709-714.

Grelier, F. (2018) *CO2 Emissions From Cars: the facts.* European Federation for Transport and Environment. Report number: 2.

Grohmann, T.(2016) Forming of AMAG 7xxx Series Aluminium Sheet Alloys. In: Amag. *New Developments in Sheet Metal Forming*, Germany, AMAG. pp. 1-21.

Harrison, N. R., Friedman, P. A. & Pan, J. (2015) Warm forming die design, Part III: Design and validation of a warm forming die. *Journal of Manufacturing Processes.* 20**,** 356-366.

Heinz, A., Haszler, A., Keidel, C., Moldenhauer, S., Benedictus, R. & Miller, W. S. (2000) Recent development in aluminium alloys for aerospace applications. *Materials Science and Engineering: A.* 280**,** 102-107.

Hu, Y., Wang, L., Politis, D. J. & Masen, M. A. (2017) Development of an interactive friction model for the prediction of lubricant breakdown behaviour during sliding wear. *Tribology International.* 110**,** 370-377.

Hu, Y., Zheng, Y., Politis, D. J., Masen, M. A., Cui, J. & Wang, L. (2019) Development of an interactive friction model to predict aluminum transfer in a pin-on-disc sliding system. *Tribology International.* 130**,** 216-228.

Imperial College London. (2020) *Metal forming and materials modelling*. Available from: http://www.imperial.ac.uk/metal-forming [Accessed 16th September 2020].

Instron. (2020a) *The Definitive Guide to ASTM E8/E8M Tension Testing of Metals*. Available from: https://www.instron.us/testing-solutions/the-definitive-guide-to-astm-e8-e8m [Accessed 16th September 2020].

Instron. (2020b) *Instron : Materials Testing Machines for Tensile, Fatigue, Impact, Rheology and Structural Testing - Instron*. Available from: https://www.instron.co.uk/ [Accessed 12th June 2020].

Karbasian, H. & Tekkaya, A. E. (2010) A review on hot stamping. *Journal of Materials Processing Technology.* 210**,** 2103-2118.

Kaufman, J. G. (2000) *Introducton to aluminum alloys and tempers.*The United States of America, ASM International.

Keci, A., Harrison, N. R. & Luckey S. George.(2014) Experimental Evaluation of the Quench Rate of AA7075. In: Sae. *World Congress & Exhibition*, The United States of America, SAE International. pp. 984-998.

Keum, Y.T. & Han, B.Y. (2002) Springback of FCC sheet in warm forming. *Journal of Ceramic Processing Research.* 3**,** 159-165.

Kim, H. S. & Koç, M. (2008) Numerical investigations on springback characteristics of aluminum sheet metal alloys in warm forming conditions. *Journal of Materials Processing Technology.* 204**,** 370-383.

Kinsey, B. L. & Wu, X. (2011) *Tailor Welded Blanks for Advanced Manufacturing.*The United States of America, Woodhead Publishing.

Klampfer, J. (2017) Email send to Zhaoheng Cai, 10th November.

Kumar, M., Poletti, C. & Degischer, H. P. (2013) Precipitation kinetics in warm forming of AW-7020 alloy. *Materials Science and Engineering: A.* 561**,** 362-370.

Kwansoo, C. T. K., Rahul, K. V., Taejoon, P., Hoon, H. & Gihyun, B.(2011) Part C: Benchmark Problems and Results. In: *The 8th NUMISHEET conference*, Seoul, Korea, pp. 177.

Lassance, D., Fabrègue, D., Delannay, F. & Pardoen, T. (2007) Micromechanics of room and high temperature fracture in 6xxx Al alloys. *Progress in Materials Science.* 52**,** 62-129.

Laurent, H., Coër, J., Greze, R., Manach, P. Y., Andrade-Campos, A., Oliveira, M. & Menezes, L. (2011) Mechanical Behaviour and Springback Study of an Aluminium Alloy in Warm Forming Conditions. *ISRN Mechanical Engineering.* 2011.

Leitão, C., Eml Lio, B., Chaparro, B. M., Rodrigues, D. M. J. M. & Design (2009) Formability of similar and dissimilar friction stir welded AA 5182-H111 and AA 6016-T4 tailored blanks. 30**,** 3235-3242.

Lenton. (2020) *Chamber furnaces for laboratory & industrial use - Carbolite Gero*. Available from: https://www.carbolite-gero.com/products/chamber-furnaces/ [Accessed 12th June 2020].

Li, D. & Ghosh, A. K. (2004) Biaxial warm forming behavior of aluminum sheet alloys. *Journal of Materials Processing Technology.* 145**,** 281-293.

Li, H., He, L., Zhao, G. & Zhang, L. (2013) Constitutive relationships of hot stamping boron steel B1500HS based on the modified Arrhenius and Johnson–Cook model. *Materials Science and Engineering: A.* 580**,** 330-348.

Li, N., Zheng, J., Zhang, C., Zheng, K., Lin, J. & Dean, T. (2015) Investigation on fast and energy-efficient heat treatments of AA6082 in HFQ processes for automotive applications. *MATEC Web of Conferences.* 21**,** 05015.

Li, X., Roth, C. C. & Mohr, D. (2019) Machine-learning based temperature- and rate-dependent plasticity model: Application to analysis of fracture experiments on DP steel. *International Journal of Plasticity.* 118**,** 320-344.

Li, X. Z., Hansen, V., Gjønnes, J. & Wallenberg, L. R. (1999) HREM study and structure modeling of the η′ phase, the hardening precipitates in commercial Al–Zn–Mg alloys. *Acta Materialia.* 47**,** 2651-2659.

Li, Y., Madhusudana, C. & Leonardi, E. (2000) Enhancement of Thermal Contact Conductance: Effect of Metallic Coating. *Journal of Thermophysics and Heat Transfer.* 14**,** 540-547.

Lin, J. & Dean, T. A. (2005) Modelling of microstructure evolution in hot forming using unified constitutive equations. *Journal of Materials Processing Technology.* 167**,** 354-362.

Liu, D., Xiong, B., Bian, F., Li, Z., Li, X., Zhang, Y., Wang, Q., Xie, G., Wang, F. & Liu, H. (2015a) Quantitative study of nanoscale precipitates in Al-Zn-Mg-Cu alloys with different chemical compositions. *Materials Science and Engineering: A.* 639**,** 245-251.

Liu, J., Gao, H., Fakir, O. E., Wang, L. & Lin, J. (2015b) HFQ forming of AA6082 tailor welded blanks. *MATEC Web of Conferences.* 21**,** 05006.

Liu, J., Wang, A., Gao, H., Gandra, J., Beamish, K., Zhan, L. & Wang, L. (2018a) Transition of failure mode in hot stamping of AA6082 tailor welded blanks. *Journal of Materials Processing Technology.* 257**,** 33-44.

Liu, J., Wang, A., Zheng, Y., Liu, X., Gandra, J., Beamish, K., Petre, A. & Wang, L.-L. (2017a) Hot stamping of AA6082 tailor welded blanks for automotive applications. *Procedia Engineering.* 207**,** 729-734.

Liu, J., Wang, L.-L., Lee, J., Chen, R., El-Fakir, O., Chen, L., Lin, J. & Dean, T. A. (2015c) Size-dependent mechanical properties in AA6082 tailor welded specimens. *Journal of Materials Processing Technology.* 224**,** 169-180.

Liu, X., El Fakir, O., Cai, Z., Dalkaya, B., Wang, K., Gharbi, M. M. & Wang, L. (2019a) Development of an interfacial heat transfer coefficient model for the hot and warm aluminium stamping processes under different initial blank temperature conditions. *Journal of Materials Processing Technology.* 273**,** 116245.

Liu, X., El Fakir, O., Zheng, Y., Gharbi, M. M. & Wang, L. (2019b) Effect of tool coatings on the interfacial heat transfer coefficient in hot stamping of aluminium alloys under variable contact pressure conditions. *International Journal of Heat and Mass Transfer.* 137**,** 74-83.

Liu, X., Fakir, O. E., Meng, L., Sun, X., Li, X. & Wang, L. (2018b) Effects of lubricant on the IHTC during the hot stamping of AA6082 aluminium alloy: Experimental and modelling studies. *Journal of Materials Processing Technology.* 255**,** 175-183.

Liu, X., Gharbi, M. M., Manassib, O., El Fakir, O. & Wang, L. (2017b) Determination of the interfacial heat transfer coefficient between AA7075 and different forming tools in hot stamping processes. *Procedia Engineering.* 207**,** 717-722.

Liu, X., Ji, K., Fakir, O. E., Fang, H., Gharbi, M. M. & Wang, L. (2017c) Determination of the interfacial heat transfer coefficient for a hot aluminium stamping process. *Journal of Materials Processing Technology.* 247**,** 158-170.

Lloyd, D. J. & Chaturvedi, M. C. (1982) A calorimetric study of aluminium alloy AA-7075. *Journal of Materials Science.* 17**,** 1819-1824.

Luan, X., Cai, Z., Sun, Y., Zhang, Q., Fakir, O. E., Wu, G., Lin, J. & Wang, L. 2019. *A device for simulating the hot stamping process of a sheet*. China patent application CN201910707785.9.

Lutsey, N. & Sperling, D. (2005) Energy Efficiency, Fuel Economy, and Policy Implications. *Transportation Research Record.* 1941**,** 8-17.

Maeno, T., Mori, K.-I. & Yachi, R. (2017) Hot stamping of high-strength aluminium alloy aircraft parts using quick heating. *CIRP Annals.* 66**,** 269-272.

Mallick, P.K. (2010) *Materials, design and manufacturing for lightweight vehicles.*The United Kingdom, Matthew Deans.

Make it from. (2020) *Aluminum Alloys*. Available from: https://www.makeitfrom.com/material-group/Aluminum-Alloy [Accessed 4th December 2020].

Merklein, M., Hofmann, M., Lechner, M. & Kuppert, A. (2014) A review on tailored blanks—Production, applications and evaluation. *Journal of Materials Processing Technology.* 214**,** 151–164.

Merklein, M., Wieland, M., Lechner, M., Bruschi, S. & Ghiotti, A. (2016) Hot stamping of boron steel sheets with tailored properties: A review. *Journal of Materials Processing Technology.* 228**,** 11-24.

Merrill L. Minces. (1966) *Thermal contact resistance.* Air Force Materials Laboratory Research and Technology Division. Report number: I.

Metz, B., Davidson, O., Bosch, P., Dave, R. & Meyer, L. (2007) *Climate Change 2007 Mitigation.*The United States of America, Cambridge University Press.

Milkereit, B., Österreich, M., Schuster, P., Kirov, G., Mukeli, E. & Kessler, O. (2018) Dissolution and Precipitation Behavior for Hot Forming of 7021 and 7075 Aluminum Alloys. *Metals - Open Access Metallurgy Journal.* 8 (7).

Milkereit, B., Wanderka, N., Schick, C. & Kessler, O. (2012) Continuous cooling precipitation diagrams of Al–Mg–Si alloys. *Materials Science and Engineering: A.* 550**,** 87-96.

Mishra, R. S. & Ma, Z. Y. (2005) Friction stir welding and processing. *Materials Science and Engineering: R: Reports.* 50**,** 1-78.

Mohamed, M. S., Foster, A. D., Lin, J., Balint, D. S. & Dean, T. A. (2012) Investigation of deformation and failure features in hot stamping of AA6082: Experimentation and modelling. *International Journal of Machine Tools and Manufacture.* 53**,** 27-38.

Moon, Y. H., Kang, S. S., Cho, J. R. & Kim, T. G. (2003) Effect of tool temperature on the reduction of the springback of aluminum sheets. *Journal of Materials Processing Technology.* 132**,** 365-368.

Ostermann, F. (1998) *Anwendungstechnologie Aluminium.*Germany, Springer.

Palumbo, G., Piccininni, A., Guglielmi, P. & Di Michele, G. (2015) Warm HydroForming of the heat treatable aluminium alloy AC170PX. *Journal of Manufacturing Processes.* 20**,** 24-32.

Palumbo, G. & Tricarico, L. (2007) Numerical and experimental investigations on the Warm Deep Drawing process of circular aluminum alloy specimens. *Journal of Materials Processing Technology.* 184**,** 115-123.

Polmear, I., Stjohn, D., Nie, J.-F. & Qian, M. (2017) *Light Alloys Metallurgy of the Light Metals (5th ed.).*The United States of America, Butterworth-Heinemann.

Polmear, I. J. (1995) *Metallurgy of the light metals.*The United Kingdom, Edward Arnold.

Polmear, I. J. (2005) Wrought aluminium alloys. *In:* Polmear, I. J. (ed.) *Light Alloys (Fourth Edition).* The United Kingdom, Butterworth-Heinemann, pp. 97-204.

Prabhu, T. R. (2015) An Overview of High-Performance Aircraft Structural Al Alloy-AA7085. *Acta Metallurgica Sinica (English Letters).* 28**,** 909-921.

Ramezani, M. & Ripin, Z. M. (2012) 1 - Introduction to sheet metal forming processes. *In:* Ramezani, M. & Ripin, Z. M. (eds.) *Rubber-Pad Forming Processes.* Woodhead Publishing, pp. 1-22.

Sáenz De Argandoña, E., Galdos, L., Ortubay, R., Mendiguren, J. & Agirretxe, X. (2015) Room Temperature Forming of AA7075 Aluminum Alloys: W-Temper Process. *Key Engineering Materials.* 651-653**,** 199-204.

Salazar, A. (2003) On thermal diffusivity. *European Journal of Physics.* 24**,** 351.

Sanders, R. E. (2001) Technology innovation in aluminum products. *JOM.* 53**,** 21-25.

Sato, T. & Matsuda, K. (2003) History of research and development of Al–Mg–Si alloys. *Journal of Japan Institute of Light Metals.* 53**,** 449-453.

Schloth, P. (2015) *Precipitation in the high strength AA7449 aluminium alloy: implications on internal stresses on different length scales.* Doctor of Philosophy, Swiss Federal Institute of Technology Lausanne, doi: 10.5075/epfl-thesis-6525.

Shao, Z., Li, N., Lin, J. & Dean, T. (2017) Strain measurement and error analysis in thermo-mechanical tensile tests of sheet metals for hot stamping applications. *Proceedings of the Institution of Mechanical Engineers, Part C: Journal of Mechanical Engineering Science.* 095440621771401.

Shi, Z., Wang, Y., Lin, J., Dean, T., Balint, D., Stanton, M. & Watson, D.(2012) An Investigation, Using Standard Experimental Techniques, to Determine FLCs at Elevated Temperature for Aluminium Alloys. In: *3rd International Conference on New Forming Technology*, China, Spiral. pp. 100-104.

Simões, V. M., Oliveira, M. C., Laurent, H. & Menezes, L. F. (2019) The punch speed influence on warm forming and springback of two Al-Mg-Si alloys. *Journal of Manufacturing Processes.* 38**,** 266-278.

Smart Forming. (2020) *Smart Forming*. Available from: https://smartforming.com [Accessed 5th December 2020].

Smith, B. A., Spulber; Shashank, Modi; Terni, Fiorelli 2017. Technology Roadmaps: Intelligent Mobility Technology, Materials and Manufacturing Processes, and Light Duty Vehicle Propulsion. Ann Arbor, Ml: Centre for Automotive Research.

Struers. (2020) *Grinding and polishing machines and equipment*. Available from: https://www.struers.com/en/Products/Grinding-and-Polishing/Grinding-and-polishing-equipment [Accessed 12th June 2020].

Tarng, Y. S., Tsai, H. L. & Yeh, S. S. (1999) Modeling, optimization and classification of weld quality in tungsten inert gas welding. *International Journal of Machine Tools and Manufacture.* 39**,** 1427-1438.

Tekkaya, A. E. (2000) State-of-the-art of simulation of sheet metal forming. *Journal of Materials Processing Technology.* 103**,** 14-22.

The Aluminum Association. (2015). *Aluminum Alloys 101* The United States of America, The Aluminum Association.

Toros, S., Ozturk, F. & Kacar, I. (2008) Review of warm forming of aluminum–magnesium alloys. *Journal of Materials Processing Technology.* 207**,** 1-12.

Torque Tips. (2017) *Audi A8 Space frame*. Available from: https://blog.swanswaygarages.com/new-audi-a8-not-taken-lightly [Accessed 12th July 2020].

United Nations Climate Change. (2015) *The Paris Agreement*. Available from: https://unfccc.int/process-and-meetings/the-paris-agreement/the-paris-agreement [Accessed 10th June 2020].

Ungureanu, C.A., Das, S. & Jawahir, I.S. (2007) Life-cycle Cost Analysis: Aluminum versus Steel in Passenger Cars. *The Minerals, Metals & Materials Society.* 11-24.

Wang, A., El Fakir, O., Liu, J., Zhang, Q., Zheng, Y. & Wang, L. (2019) Multi-objective finite element simulations of a sheet metal-forming process via a cloud-based platform. *The International Journal of Advanced Manufacturing Technology.* 100**,** 2753-2765.

Wang, A., Zhong, K., El Fakir, O., Liu, J., Sun, C., Wang, L.-L., Lin, J. & Dean, T. A. (2017) Springback analysis of AA5754 after hot stamping: experiments and FE modelling. *The International Journal of Advanced Manufacturing Technology.* 89**,** 1339-1352.

Wang, L., Strangwood, M., Balint, D., Lin, J. & Dean, T. A. (2011) Formability and failure mechanisms of AA2024 under hot forming conditions. *Materials Science and Engineering: A.* 528**,** 2648-2656.

Wanhill, R. J. H. (2014) Aerospace Applications of Aluminum–Lithium Alloys. *In:* Merken, S. (ed.) *Aluminum-lithium Alloys: Processing, Properties, and Applications.* The United Kingdom, Elsevier Inc, pp. 503-535.

Warner, T. (2006) Recently-Developed Aluminium Solutions for Aerospace Applications. *Materials Science Forum.* 519-521**,** 1271-1278.

Xu, F., Sun, G., Li, G. & Li, Q. (2014) Experimental investigation on high strength steel (HSS) tailor-welded blanks (TWBs). *Journal of Materials Processing Tech.* 214**,** 925-935.

Zhang, Q., Luan, X., Dhawan, S., Politis, D. J., Du, Q., Fu, M. W., Wang, K., Gharbi, M. M. & Wang, L. (2019) Development of the post-form strength prediction model for a high-strength 6xxx aluminium alloy with pre-existing precipitates and residual dislocations. *International Journal of Plasticity.* 119**,** 230-248.

Zhang, Y., Weyland, M., Milkereit, B., Reich, M. & Rometsch, P. A. (2016) Precipitation of a new platelet phase during the quenching of an Al-Zn-Mg-Cu alloy. *Scientific Reports.* 6**,** 23109.

Zheng, K., Dong, Y., Zheng, D., Lin, J. & Dean, T. A. (2019) An experimental investigation on the deformation and post-formed strength of heat-treatable aluminium alloys using different elevated temperature forming processes. *Journal of Materials Processing Technology.* 268**,** 87-96.

Zheng, K., Politis, D. J., Wang, L. & Lin, J. (2018) A review on forming techniques for manufacturing lightweight complex—shaped aluminium panel components. *International Journal of Lightweight Materials and Manufacture.* 1**,** 55-80.

Zhou, D., Yuan, X., Gao, H., Wang, A., Liu, J., El Fakir, O., Politis, D. J., Wang, L. & Lin, J. (2016) Knowledge Based Cloud FE Simulation of Sheet Metal Forming Processes. *JoVE.* e53957.

Zwick/Roell. (2020) *ZHR Rockwell hardness testers*. Available from: https://www.zwickroell.com/en/rockwell-hardness-testers/zhr [Accessed 12th June 2020].

Appendix-A Finite element (FE) simulation of FAST process: U-shaped component

A1. FE model setup

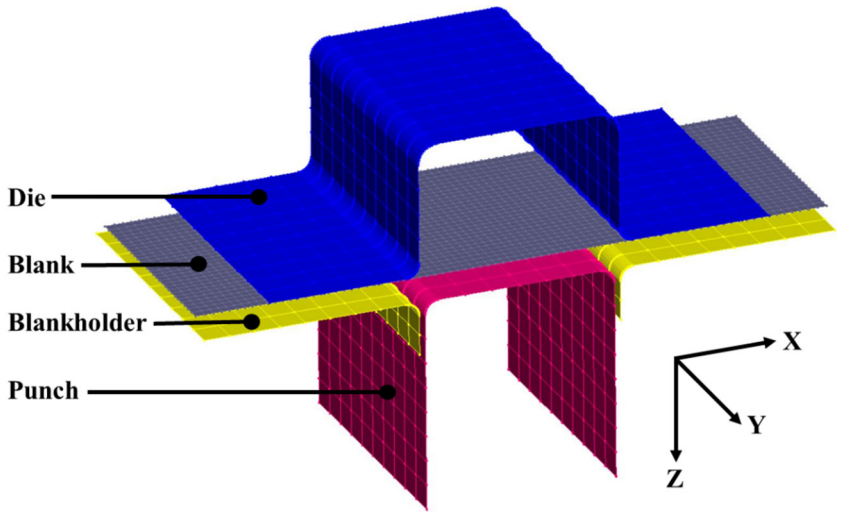

Figure A.1 Schematic diagram of FE simulation set up with mesh for U-shaped forming.

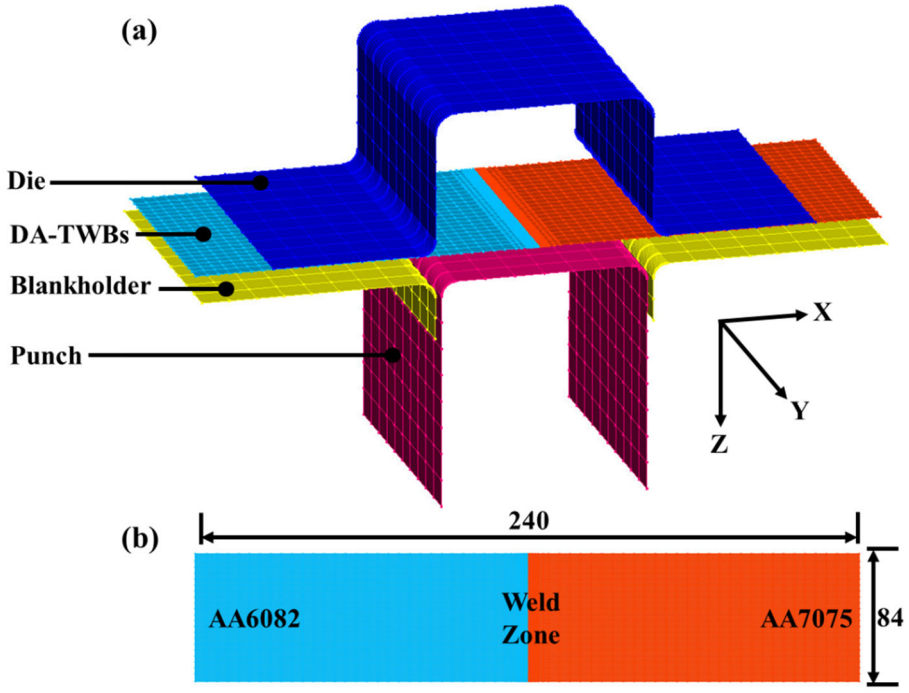

Figure A.2 FE simulation set up of U-shaped forming with DA-TWBs (a) schematic diagram with mesh and (b) design of DA-TWBs (dimensions are in mm).

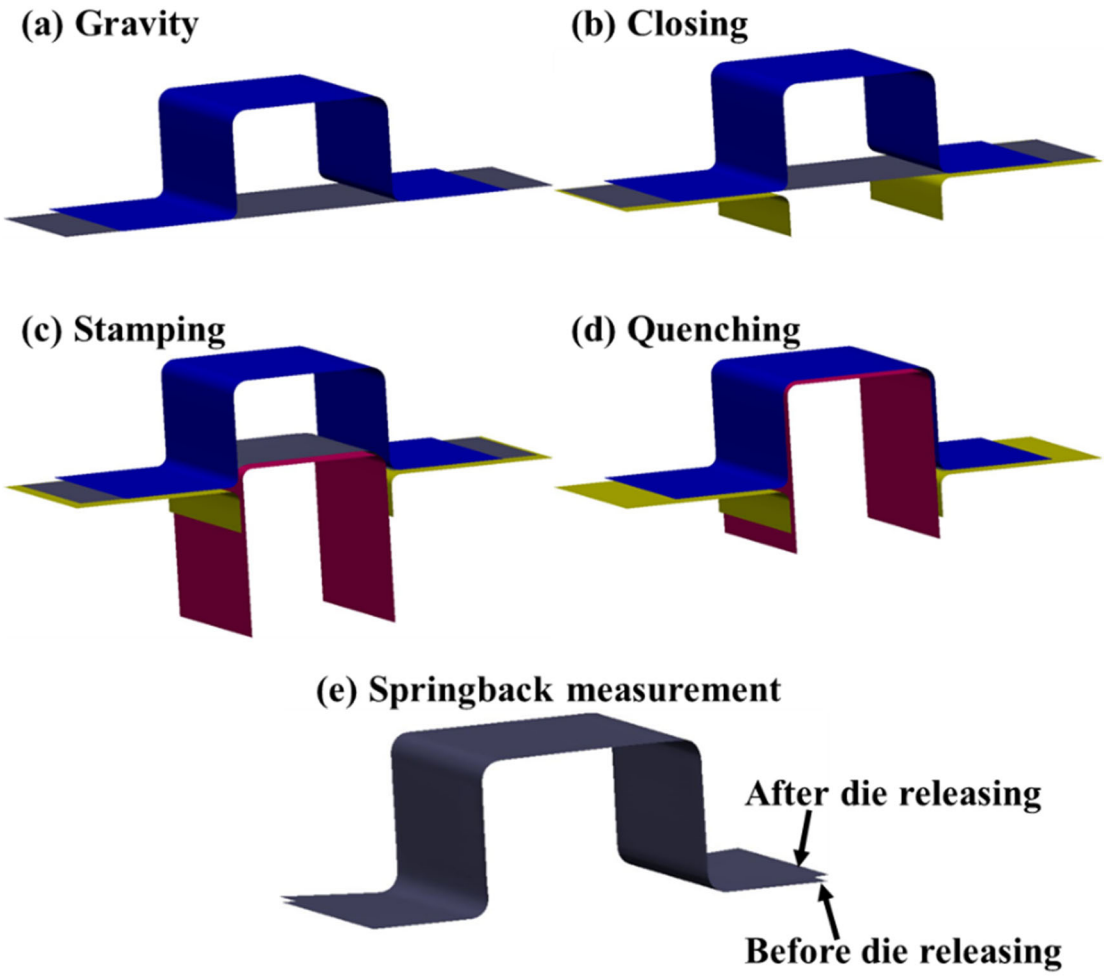

Figure A.3 Schematic diagram of FE simulation at various forming stages with springback measurement.

A2. Material model setup

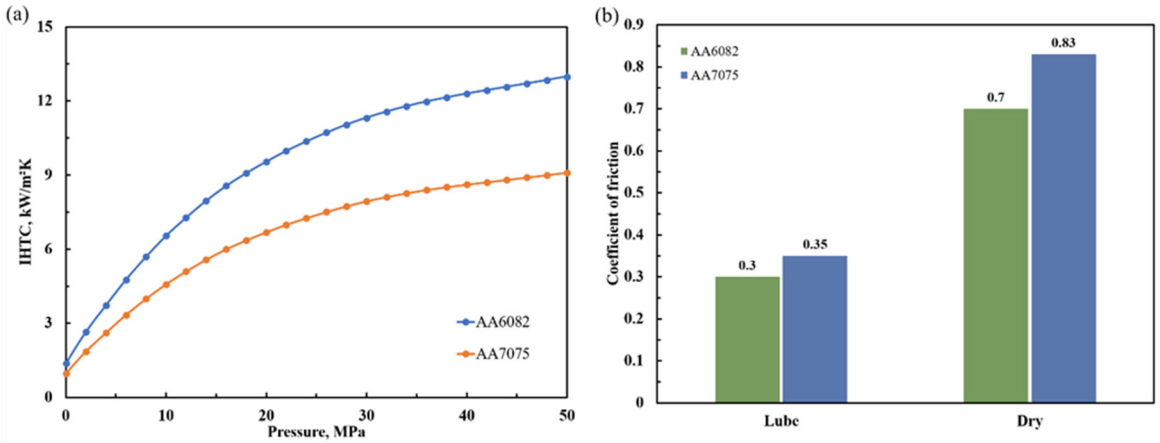

Figure A.4 (a) The IHTC and (b) the coefficient of friction of AA6082 and AA7075

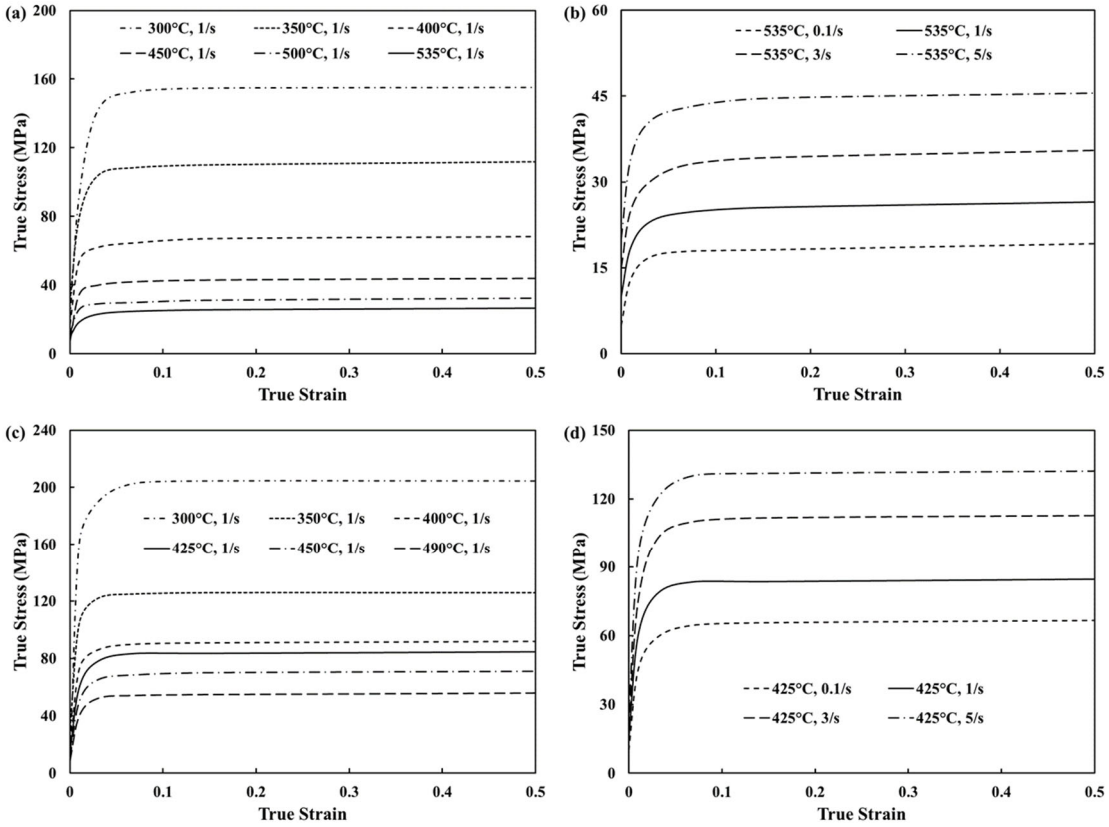

Figure A.5 Flow stress curves of (a) AA6082 at different forming temperatures, (b) AA6082 at different strain rates, (c) AA7075 at different forming temperatures and (d) AA7075 at different strain rates

A3. Verification of the FE simulation

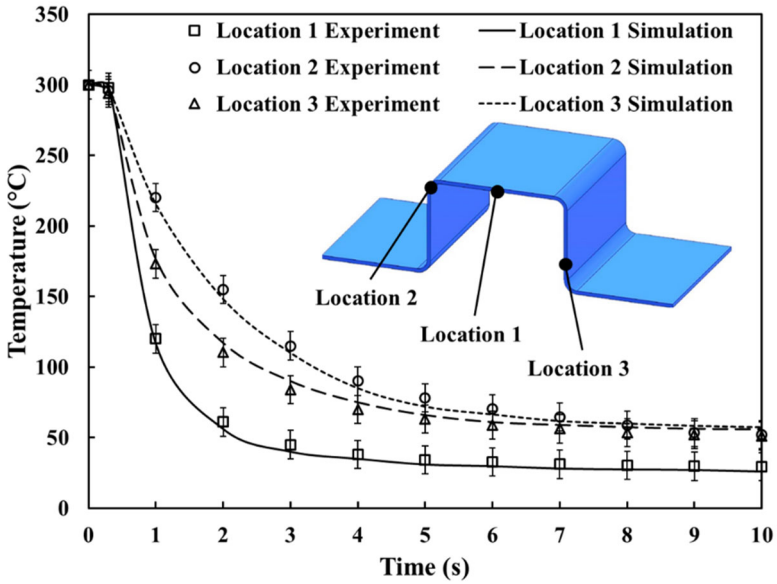

Figure A.6 Temperature evolution comparison between experiments and FE simulations during forming stage for the AA7075 blank.

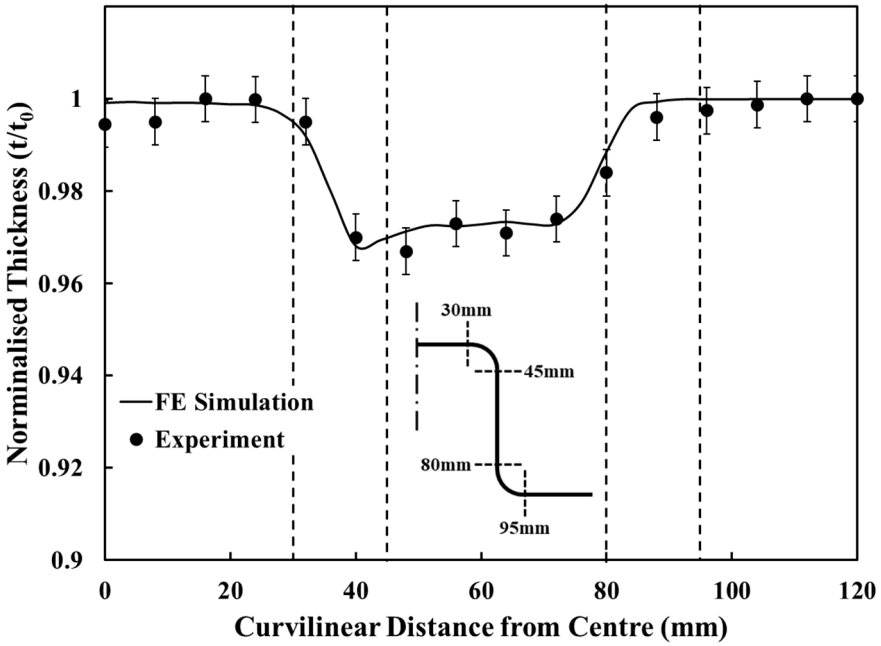

Figure A.7 Thickness distribution comparison between experiments and FE simulations of U-shaped component formed at 300°C using AA6082 blank.

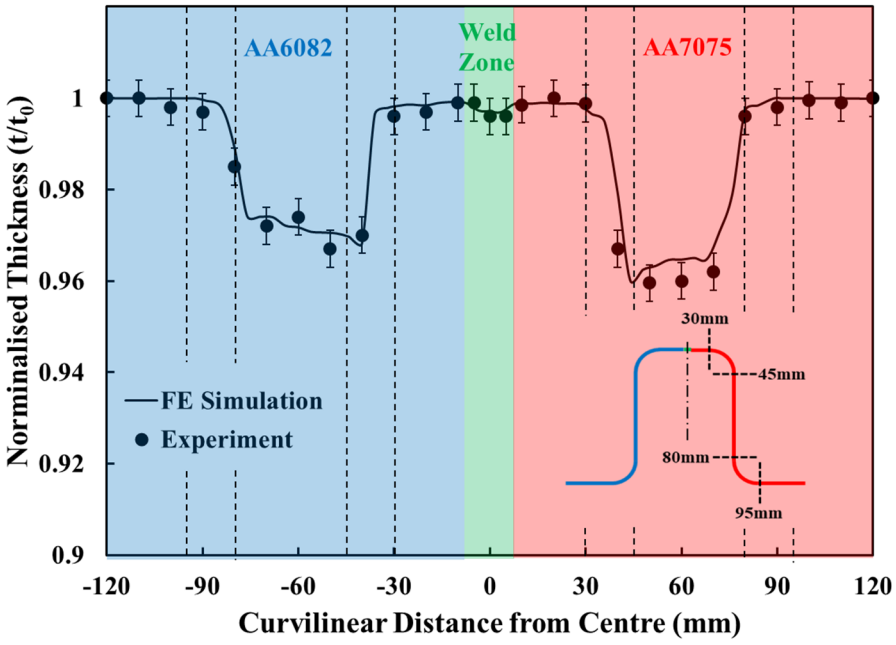

Figure A.8 Thickness distribution comparison between experiments and FE simulations of U-shaped component formed at 300°C using DA-TWBs.